Synthesis of Nickel Oxide Nanoparticles Using Gelatine as a Green Template for Photocatalytic Degradation of Dyes

by

Lee Jay Yang

Thesis Submitted In Fulfilment of the Requirements for the Degree of Master of Science

Nov 2017

COPYRIGHT NOTICE

Student Signature:

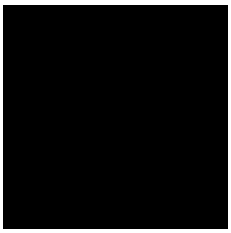

Print Name: Lee Jay Yang

Date: 19/11/2017

DECLARATION

This thesis contains no materials which has been award of other degree or diploma at any university or equivalent institution and that, to the best of my knowledge and believe, this thesis contains no material previously published or written by another person, except where due reference is made in the text of the thesis.

Student Signature:

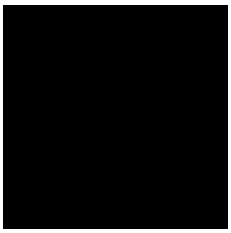

Print Name: Lee Jay Yang

Date: 19/11/2017

ACKNOWLEDGEMENT

Firstly, I would like to express my gratefulness towards my supervisor Dr. Babak Salamatinia for his constant guidance and supervision throughout my studies. Secondly, I would like to extend my thanks to Dr. Bahman Amini Horri and Dr. Horizon Briggs for their insight as well as knowledge regarding the synthesis process. Many thanks to Ms Nurul Hidayah and Mr. Azarudin Ahmad for their assistance in the laboratory works. Lastly, my deepest gratitude to my beloved family for their constant support in this research.

TABLE OF CONTENTS

LIST OF TABLES

LIST OF FIGURES

LIST OF SYMBOLS

Symbols	Description	Unit
C	Concentration at time, t	ppm
C_1	Concentration at t=0	ppm
R^2	Correlation factor	-
L	Crystallite size	nm
d	Diameter	mm
Ɵ	Diffraction Peak	rad
β	Full width half minimum	-
m	Mass	g
k_1	Rate constant for second order degradation model	min^{-1}
k_2	Rate constant for second order degradation model	min^{-1}
k	Scherer's Constant	-
T	Temperature	^oC
t	Time	min
l	Wavelength	nm
wt %	Weight Percentage	%

LIST OF ABBREVIATION

Abbreviation	Name
AOP	Advanced Oxidation Process
AY25	Acid Yellow 25
BET	Brunauer-Emmett-Teller
CO	Carbon Monoxide
CO_2	Carbon Dioxide
CeO_2	Cerium (IV) Oxide
CB	Conduction Band
e^-	Electron
FESEM	Field Emmission Scanning Electron Microscopy
FTIR	Fourier Transform Infrared Spectroscopy
OH	Hydroxyl
OH^-	Hydroxide ion
$OH\cdot$	Hydroxyl radical
$HO_2\cdot$	Hydroperoxide radical
h^+	holes
Fe_2O_3	Iron (II) Oxide
LO	Longitudinal Optical
Ni	Nickel
NiO	Nickel Oxide
$Ni(OCOCH_3)_2\cdot 4H_2O$	Nickel Acetate Tetrahydrate
RB5	Reactive Black 5
$O_2^-\cdot$	Superoxide radical
SnO_2	Tin Oxide
TiO_2	Titanium Oxide

UV	Ultra Violet
UV-VIS	Ultra Violet something
VB	Valence Band
H_2O	Water
XRD	X-ray Diffractogram
Zn	Zinc
ZnO	Zinc oxide
ZnS	Zinc Sulphide

ABSTRACT

In this study, nickel oxide (NiO) nanoparticles of spherical shape were prepared through a proteic sol-gel method followed by calcination process. The aim of this research is to synthesize NiO nanoparticles with a green material, gelatin. Catalytic activity of the synthesized NiO nanoparticles were studied through photocatalytic degradation of Acid Yellow 25 and Reactive Black 5 dyes. Nickel acetate tetrahydrate and gelatin from bovine skin were used as the starting materials for reaction and subsequent drying to form a xerogel precursor. Subsequently, the precursor was calcinated to form a dark green or black nickel oxide powder. Utilizing gelatin as a templating agent will reduced the amount of chemicals promotes a more environmentally friendly synthesizing method. The calcinated products were characterized by TGA, FE-SEM, RAMAN spectroscopy and XRD analytical techniques. The effects of concentration of starting materials, reaction time, calcination time and temperature were examine on the purity and morphological properties of the resulting nickel oxide product. TGA results revealed that the precursor was completely degraded at a temperature of 420 ^{o}C and with calcination temperature of above 500 ^{o}C for 2 h of calcination time, all the functional groups from the precursor were completely removed as confirmed by FT-IR and RAMAN analysis. XRD, RAMAN and FT-IR results showed that there are no unexpected peaks besides the peaks corresponding to NiO. The FE-SEM images showed that nanoparticles of at least 5.94 nm were obtained with spherical shape. The NiO calcined at 500 ^{o}C for 4 h was of weak agglomeration with small particle size of 13.9 nm. It was noted that the particle size increase with an

increasing time and temperature with NiO diffraction peaks that corresponds to (1 1 1), (2 0 0), (2 2 0), (3 1 1) and (2 2 2) planes, indicating the formation of busenite structure with face-centered cubic atomic arrangement. The synthesized NiO was employed for photocatalytic studies of AY25 and RB5 dyes optimizing with various parameters such as catalyst loading, calcination time and temperature of catalyst to determine the catalytic performance of NiO. The result showed that 0.75 g of NiO catalyst had the highest degradation rate and decolorization efficiency of 80.82 % for RB5 dye. 0.5 g of NiO catalyst was found to have the highest degradation rate for AY25 with a decolourization efficiency of 53.08 %. Calcination time and temperature of NiO showed similarity with 500 ^{o}C and 4 h for highest degradation rate for both dyes. The data obtained were found to have a best fit in a pseudo second order model. The usage of gelatin as a green material for the synthesis of nanoparticles has shown promising results that allows a more environmental friendly and sustainable approach for the fabrication of nanomaterials.

CHAPTER 1

INTRODUCTION

1.1. Background

Over the past decades, the continuous advancement of technology and globalization has led to a major boost in industrial activities to supply the ever-growing needs of the human population. However, the increasing industrial activities comes with its adverse effects on the environment. The release of greenhouse gases from factories and dumping of wastewater into the river or sea have become a serious issue. Developing countries are enforcing stricter laws to limit and mitigate the harmful environmental effects from these industrial sectors. Therefore, wastewater treatment plants and facilities are being invested to achieve the environmental regulations and mitigate the environmental effects on the aquatic ecosystem.

Nanotechnology based semiconductors for photocatalytic degradation is an efficient method for waste water treatment. The principal behind photocatalytic degradation is the catalyst being excited by the photons from a source light to generate electron hole pairs. Subsequently, photo-induced charges disperse and migrate to the active reaction sites that finally on the surface of the catalyst the contaminant is degraded and reduced. Selection of semiconductor metals are also crucial in determining the properties and usage of the nanotechnology due to the difference in chemical and physical properties of the metals. Conversely, the physical and chemicals properties are

a function of the size and shape; therefore it differs as compared to the independent constant properties of bulk materials.

1.2. Dye Degradation

Azo dyes are one of the major concerns in the pollution of wastewater. The discharge of dyes by dye manufacturing and textile industries has become an environmental concern. It has been reported that about 280,000 tons of textile dyes are discharged in the industrial effluents every year (Solís et al., 2012). The main issue involving the harmful effects of azo dyes includes toxicity to the environment, inhibiting the photosynthesis in aquatic flora and deplete dissolved oxygen for aquatic lifeforms (Brüschweiler and Merlot, 2017). dye effluent poses a problem for manufacturing plants and water-treatment downstream as the undesired aesthetics of coloured stream resulting from the dye waste sometimes may undergo anaerobic degradation to form amines based carcinogen (Harisha et al., 2017). Many different water treatment methods have been developed and studied through physical, chemical or biological treatments. Physical removal process such as sedimentation and filtration are widely used due to their simplicity and low cost in technology to remove solids. However, it has a lot of drawbacks where sedimentation require long period of time and it does not remove pathogens and viruses present in the water (Rodriguez-Narvaez et al., 2017). Biological methods focus on the use of microbial treatment to remove the pollutants. Although biological methods have been utilized for dye removal, the long detention times and cost intensive of the maintenance are the limitation (Shi et al., 2017). Chemical treatment uses the principle of oxidation to degrade the dyes into environmentally friendly organic compounds. A special oxidation technique defined as Advanced Oxidation Processes

(AOPs) could successfully mitigate the current limitation of current water treatment technologies as the operating parameters are very low and the retention time is relatively low (Ltaïef et al., 2017).

Photocatalysis is a category under AOP which is a heterogeneous process that employs catalyst to increase the rate of degradation process in the presence of light. Photocatalysis has been employed as a mitigation step to ensure continuous sustainability of the environment. Photocatalysis is gaining more popularity in the water treatment sector due to the easy setup, operation at ambient temperature and low energy consumption. Photocatalysis is the acceleration of a reaction in the presence of a catalyst and light source. The irradiation of a semiconductor with light energy generates electron hole pairs ($e^-_{CB} + h^+_{VB}$) and the equivalent or exceeding its band energy gap promotes the movement of electrons (e^-) from the valence band to the conduction band, leaving positive electron holes in the valence band (h^+) (Linda et al., 2016). This initiates a redox reaction and molecular transformation that degrades the pollutant to organic compounds such as carbon dioxide and water (Molinari et al., 2014).

1.3. Synthesis of Nanoparticles

Nanotechnology is defined as a material that have at least one dimension in the range of 1 – 100 nm (Duhan et al., 2017). Synthesis of metal nanoparticles has gained significant interest due to their large surface area to volume ratio resulting in higher efficiency. The reduction in particle size will give superior characteristics of the material in terms of changes of electronic and lattice structure, reduction of band gap and lower melting point (Santhosh et al., 2016). An important deliberation for producing

nanoparticles would be the synthesis methods and materials involved. Different techniques have been used to synthesize nanocrystalline nanoparticles. There are many synthetic methods to produce nickel oxide nanoparticles however, these synthesis routes often utilize external additives like stabilizers, reducing agents and surfactants. Synthetic methods with high temperature and pressure are also an unwanted drawbacks. Nanoparticle synthesis routes such as hydrothermal (Mutta et al., 2017), chemical precipitation (Sharma et al., 2016) and thermal decomposition (Yang et al., 2017) have been employed for nanoparticle synthesis the past decade. Overall practicality of the synthetic route is a major consideration that researchers are exploring as the feasibility, simplicity and efficiency have to be considered other than the particle size and morphology. Many of these synthetic routes reduces the metal salts in the presence of capping agents such as ammonia (Mbuyisa et al., 2015), sodium hydroxide (Yang et al., 2013) and ethanol (Saghatforoush et al., 2012) to exercise control over the size and shape of the nanoparticles. These techniques usually employ a multi-step process that increases the complexity and energy consumption, which are not environmentally friendly.

There are several key requirements which have to be fulfilled in the synthesis route of material in order to be classified as a green nanotechnology. Primarily, the selection of raw materials and cost effectiveness of the synthesis route is of necessity. Material that is biodegradable, natural and abundant that works with low operating temperature should be considered. Other than that, the engineered nanoparticles must have good particle size distribution, crystallinity and morphology (Stankic et al., 2016). A small nano-sized particle with low agglomeration is the desired outcome of the

synthesis route. Different techniques such as, hydrothermal (Swetha and Geetha, 2015), sol-gel (Mao et al., 2017), co-precipitation (Kurian and Nair, 2016), and micro-emulsion (Junaid et al., 2016) have already been reported. However, these preparation methods posed some disadvantages. For example, precipitation method is affected by various factors such as precipitation agent, pH, temperature, and solution concentration, thus complicating the synthesis process. Furthermore, these methods require either expensive raw material or special equipment to synthesize the nanoparticles, which are not favourable for large scale application.

Amongst the several investigated methods, the sol–gel method to prepare nanoparticles represents an effective synthesis route. Advantages of this method includes the simplicity of the method, which does not require high temperature or high pressure. Besides, comparative study conducted with sol-gel synthesis and co-precipitation method to synthesize nanoparticles shows that sol-gel synthesis route has better homogeneity of end products (Smalenskaite et al., 2017). However, these conventional methods utilize metal alkoxides, alcohol or acids as the precursor, which are not environmentally friendly.

Synthesis route and capping agents are not the only factors that determine the properties of the nanoparticles. Different element of metals will yield different properties when reduced to a nanoscale. This occurrence ensues because of the large surface area to volume ratio of nanoparticles that results in a highly reactive and quantum size effects becoming dominant at nanoscale (Saravanan et al., 2017b). Semiconductors, especially metal oxides within groups II to VI of the periodic table are

receiving much interest due to their superior physical and chemical properties (Qing et al., 2015). One of the metals that is categorized in that division is nickel, (Ni).

Nickel oxide (NiO) is classified as a face center cubic crystal structure, and is a p-type semiconductor transition metal oxide material with a direct band gap value of 3.5-3.8 eV that exists in large exciton binding energy of 40 meV (Hashem et al., 2016). Ni is a group II transition metal and also a semiconductor. NiO has been under intensive investigation by researchers because of the versatility of application including battery cathodes (Li et al., 2016), gas sensors (Yamini et al., 2017), magnetic materials (Tadic et al., 2015) and catalyst (Banković–Ilić et al., 2017). Nano-sized NiO is expected to present improved properties because of the quantum and surface effect difference between the bulk material of NiO and nanocrystalline NiO. Additionally, physicochemical properties of NiO is highly dependent on the particle size, crystalline phase and morphology (Fazlali et al., 2015). Manipulation of these variables will enhance the NiO potential. Therefore, it is of great significance to synthesize uniform NiO with a unique morphology and particle size being as small as possible with a high crystallinity.

1.4. Problem Statement

Metal nanoparticles contains a lot of potential in terms of reducing the bulk size material to nano-size because of the heighten physiochemical properties. The versatility of metal nanoparticles in synthesis route is another factor that makes it an interesting research subject. Particle size distribution is the most important factor in nanotechnology due to the properties of metal nanoparticles being exceedingly reliant

on particle size (Braga et al., 2015). Furthermore, NiO nanoparticles have a major disadvantage where particles tend to agglomerate and form aggregations. This results in a reduction of available active sites that will impede the catalytic activity, thus lessen the efficiency. Furthermore, metal salts coupled with green material such as gelatin shows many advantages like low cost, high availability, environmentally friendly and biocompatible. Utilization of gelatin as a templating agent for metal nanoparticles holds great potential for long term practice. However, this combination is also met with a couple of drawbacks. The instability to control size distribution, morphology and crystallinity of the product is a major issue. It is important to understand the reason behind the drawbacks and advantages to improve the synthesis method in order to yield an optimum nano-product.

The lack of stoichiometric data of the gelatin proves to be a challenge in optimizing the nickel salt to gel ratio, which increases the complexity of the synthesis process. Several key parameters have to be considered such as, the dilution of gel, mass of gel required to react with certain amount of nickel salt. In addition, controlling the particle size distribution without any stoichiometric calculation is challenging because different ratios of mass to molarity will result in a reduction of size homogeneity of nano-sized nickel oxide. Sol-gel technique is used to overcome this challenge as it produces a thin bond-coating to provide an excellent linkage between the metallic substrate and the gel that improves the growth of crystalline nanoparticles. Additionally, the low sintering capability of sol-gel method will minimize the occurrence of agglomeration of NiO nanoparticles. Furthermore, it is remarkable to determine the

feasibility of producing metal nanoparticles using low processing variables with green templates on the photocatalysis process.

To the knowledge of the author, so far there are no in depth studies on varying preparation conditions of NiO nanoparticles for the degradation of azo dyes. Altering the samples synthesizing conditions will produce different physicochemical properties of nanoparticles. Investigating the catalytic activity of the nickel oxide nanoparticles synthesized through different conditions will provide a better understanding regarding the effect of particle size, morphology and crystallinity on the degradation of dyes. Hence, this research focus on detailed investigation of all the parameters that will affect the particle size, morphology and crystalline of the product. Additionally, two different dyes will be conducted for degradation experiment to further comprehend the mechanism of degradation of dyes on the NiO catalysts.

1.5. Research Objectives

This research consists of three main objectives as described below:

1) To investigate the effects of nickel acetate molarity, mass of gelatin and reaction time on the NiO nanoparticles.
2) To investigate the effects of calcination time and temperature on the nickel oxide nanoparticles.
3) To evaluate the catalytic activities of the nickel oxide products via photocatalytic of Reactive black dye 5 and Acid Yellow dye 25.

1.6. Scope of Study

In this study, sol-gel method was used to synthesize NiO nanoparticles using gelatin from bovine skin as the templating agent. The effect of synthesis parameters were explored in order to provide a better understanding on the effect of the properties of synthesized nickel oxides. Concentration of Nickel Acetate (0.5 mol to 1.25 mol), mass of gelatin (0.5 g to 2.0 g), reaction temperature (6 hour to 24 hour), calcination temperature (400 ^{o}C to 700 ^{o}C) and calcination time (2 hours to 8 hours) were the main parameters studied in the synthesis process of sol-gel reaction. The physical and chemical properties of the synthesized NiO nanoparticles were evaluated with different characterization techniques that includes Field Emission Scanning Electron Microscopy (FE-SEM), Fourier Transform Infrared Spectroscopy (FTIR), X-ray Diffraction (XRD), Raman Spectroscopy and Thermogravimetric Analysis (TGA).

The second phases of the study include selection of optimum samples based on the characterization outcomes were utilize to investigate the photo-degradation of reactive black and acid yellow 25 dyes. Various photo-degradation parameters were investigated such as catalyst loading (0 g to 1.0 g), calcination temperature (500 ^{o}C to 700 ^{o}C) and calcination time (2 h to 6 h). Dye concentration was set at 100 ppm for both reactive black and acid yellow 25 dye to determine the effects of the synthesized nickel oxide nanoparticles catalyst on the photo-degradation results. The data obtained from UV-VIS was fitted into a pseudo-first order kinetic model to determine the overall photo-degradation rate and also provides some recommendations for future studies.

1.7. Organization of Thesis

This thesis consists or five chapters including the introduction, literature review, material and methods, results and discussion and conclusion. The first chapter, Introduction briefly present the overall research of the project, problem statement and objectives of study. The second chapter, Literature Review, evaluates the background knowledge on this study and examine the previous reported studies on nanoparticle synthesis, and photocatalysis to identify the knowledge gap. Material and Methods, which is the third chapter will provide description on the materials, experimental equipment and procedures for this study in a way that other researchers are able to reflect the experiments. Chapter four presents the results obtained for the nanoparticle synthesis and photo-degradation performance of the synthesized nanoparticles as well as in depth discussions on the findings. Lastly, chapter five will conclude the study based on findings and data obtain through experimentation.

CHAPTER 2

LITERATURE REVIEW

2.1. Background

This chapter consists of a detailed review on the literature, which provides more in-depth knowledge on the objectives and highlights the findings and results of the studies conducted by previous researchers.

2.2. Dye wastewater Treatment

Industrial effluents are one of the most adverse pollutants in the environment (El Hassani et al., 2017). Effluents from textile and dye industries contains highly polluted suspended solids, high chemical oxygen demand (COD) values and other harmful bacteria (Ayati et al., 2016). These particles can be removed by chemical, physical or biological methods. However, synthetic colour dye caused from the residual dye from the textile industry requires a more complex system for elimination. Colour contamination of rivers and seas are a major issue due to the potential toxicity and visibility contaminated waters. Therefore, colour removal have been extensively studied by researchers to mitigate the current pollution.

Dyes are defined as substances that provide colour to a substrate through a process that alters the crystal structure of the substance. Textile industries are the main consumer of dyes with an estimated of 7×10^5 tons of dyes used (Uday et al., 2016). Synthetic dyes were derived from organic and inorganic compounds. Dyes are classified based on their chemical structure, solubility and textile dye application. The chromophores

functional groups in the dyes are responsible for the dye colour. Subsequently, colouring of the chromophores can be intensified by auxochromes substituents, which promotes electron donation or withdrawal (Chequer et al., 2013). Table 2.1 shows the various types of description, properties and applications of dyes.

Table 2.1: Properties and application of specific types of dyes

Dye Class	**Description**	**Solubility**	**Application**	**Associating Pollutants**	**Ref**
Acid	Anionic and with acidic functional groups in the molecular structure	Water soluble	Wool, nylon	Colour; organic acids; unfixed dyes	(Cretescu et al., 2017)
Direct	Anionic, the dyes contain sulphonic acid groups in structure	Water soluble	Cotton, rayon, paper, leather	Colour, salt, cationic fixing agents, surfactant, finish diluents, retarding agents	(Zeng et al., 2017)
Disperse	Non-ionic dyes, utilizes dispersing agents (metal salts) to retain dyes in fine dispersion	Water Insoluble	Polyester, acetate, acrylic fibers	Colour, Organic acids, phosphates, defoamers,	(Chakraborty, 2014)
Reactive	Form a covalent bond with the hydroxyl functional groups in cellulose	Water soluble	Cotton, wool, fiber, silk	Colour, Alkali pH, redox agent,	(Bhate et al., 2017)
Vat	Contains C=O chromophore structure	Water Insoluble	Cellulosic fibers, rayon, wool, cotton	Colour, alkali pH, redox agent	(Khatri et al., 2017)
Sulphur	Contains sulphonic groups	Water Insoluble	Cellulosic fibers, rayon, wool, cotton	Colour, alkali pH, redox agent	(Nguyen and Juang, 2013)

The continuation of dye applications is currently a major environmental issue that causes significant damage to the aquatic life and human health. The World Bank

estimates that 17 to 20 percent of industrial waste water was generated from textile industries (Holkar et al., 2016). The colouring of water blocks the sunlight passage into the water that impedes photosynthesis, which increases the biological oxygen demand and affects the aquatic life (Zou and Wang, 2017). Furthermore, the presence of chromophores and auxochromes in the dye molecules are carcinogenic and harmful to human health. The main challenge with the removal of dye is because of the organic matter and colorants. The complex aromatic structure and xenobiotic nature of the dyes allow it to be resistant to heat and biodegradation (Ngulube et al., 2017). In that regard, it is necessary to eliminate dyes from wastewater before being discharge to environment because of the toxicity of dyes. Thus, treatment methods for degradation of dyes have to emphasize on the decolourization of water and ensure the removal of all toxicity of the dyes.

There are a lot of technologies and treatment method that have been developed and employed to degrade the dyes as per required by the water quality guidelines. Despite the abundant technology available, industries facing difficulty to develop an economical, rapid and effective water treatment system to be used at a commercial level. Currently, wastewater treatment of dyes is being treated by three different areas such as physical, chemical and biological. All these methods present their own pros and cons. Table 2.2 shows the characteristics and disadvantages of the various water treatment methods

Table 2.2: Dye wastewater treatment method description and disadvantages

Type	Treatment Method	Characteristics	Disadvantages	Ref
Physical	Reverse Osmosis	Utilizes a semipermeable membrane to remove ions by applying pressure on the wastewater	Osmotic pressure is directly proportional to the concentration of dyes, which will use more energy as a result.	(Kwan et al., 2015)
	Nanofiltration	Nanometer sized membrane with pore sizes from 1-10nm to remove ions	Accumulation of dissolved solids that impedes the discharge of treated effluents. High cost in maintenance of membrane.	(Babu and Murthy, 2017)
	Adsorption	Accumulation of a particular pollutant from liquid or gas at the surface of an adsorbent	High cost in regeneration of adsorbents. Does not remove solid wastes, further treatment required	(Aguiar et al., 2017)
Chemical	Photocatalytic	Formation of hydroxyl radicals and hydrogen ions through the excitation of a catalyst in presence of light.	Difficulty in separation of fine catalyst in the effluent.	(Li et al., 2017)
	Ozonation	Reaction of ozone with organic molecule to generate hydroxyl radicals for the degradation of dyes	Formation of carcinogenic aromatic amines	(Mahmoodi, 2013)
	Fenton's reagent	Utilizes oxidizing agents (H_2O_2) to form hydroxyl radicals in an acidic solution containing Fe^{2+} ions.	Significant addition of acid and alkali to reach required pH, reduction of iron concentration required.	(Wang et al., 2016a)
Biological	Aerobic	Treatment of wastewater with the use of bacteria and fungi in presence of O_2	Incapable of completely degrading dye molecules due to the inability of aerobic bacteria to completely degrade dye molecule	(van der Zee and Villaverde, 2005)
	Anaerobic	Biological breakdown of organic matter in absence of O_2 to form CO_2 methane,	High temperature required. Long retention time to remove dyes (a few days)	(Pan et al., 2017)

Physical methods, especially adsorption method has been studied extensively because of the cheap and easily acquired adsorbents (Gupta et al., 2013). Furthermore, the high porosity and large surface area of adsorbents enables high adsorption capacity (Yagub et al., 2014). Adsorption mainly utilizes Van der Waals forces and dipole-dipole intermolecular interactions to adsorb the adsorbate on the surface of the adsorbent. A previous study was conducted on degradation of Rhodamine B dye using activated carbon as the adsorbents shows an efficient removal of dye with a high adsorption capacity of 757.6 mg/g (Goswami and Phukan, 2017). However, despite the high adsorption capability of physical adsorption process, the regeneration of adsorbents is both time consuming and costly (Ngulube et al., 2017). Additionally, efficiency of the adsorbents will continuously reduce after periods of regeneration.

Nanofiltration and Reverse Osmosis uses membrane technology to operate. Advantages of membrane technology includes that no by-products is formed after treatment and treatment can occur under ambient conditions without the need of any chemical additives (Dasgupta et al., 2014). However, fouling of membrane poses as a key issue for membrane technology and the high cost of replacing a membrane is not feasible in industrial scale (Van der Bruggen et al., 2008). Biological treatments such as aerobic and anaerobic are not a favourable treatment method because of the obstinate compounds of dyes that resist biological treatment. A previous study was conducted on growing the cynobacteria *Phormidium Valderianum* with anaerobic and anaerobic-aerobic system. The results concluded that the growth of cynobacteria on wastewater was slow, where complete discoloration of dyes was only achieved after 20 days (Dellamatrice et al., 2017).

Chemical methods such as ozonation, photocatalysis and Fenton's reagent are classified as Advanced Oxidation Process (AOP). AOP refers to a series of redox reaction to form strong oxidants such as hydroxyl radicals to react with the organic compound to formed harmless by-product. Ozonation is an AOP that degrades the dye through direct contact of ozone gas in a specially design ozonation. A research was conducted previously whereby ozone was used to degrade anthaquinone dyes with high decolourization efficiency of 96 % (Liu et al., 2007). However, unwanted byproducts such as chlorine and sulphuric acid and nitrates were observed. Additionally, the short half-life of ozone exhibits slow reaction time for degradation (Verma et al., 2012). Fenton's reagent is another chemical process, which is based on the electron transfer of hydrogen peroxide (H_2O_2) and iron ions acting as homogeneous catalyst to form hydroxyl radicals to degrade dyes (Babaei et al., 2017).

Numerous study has been conducted to investigate Fenton's reaction on the degradation of dyes. For example, Fenton reaction was used to degrade Direct Blue 71 dye by investigating the effect of concentration of iron ions on the colour removal of dye. It was reported that up to 94% decolourization was achieved with COD removal of 50.7 % (Ertugay and Acar, 2017). However, the iron ions in Fenton's reagent cannot be retained in the process therefore resulting in additional water pollution (Barbusinski and Majewski, 2003).

Photocatalysis is a type of AOP that involves a heterogeneous catalyst and light source that degrades the organic compound into harmless molecules such as CO_2 and H_2O. Furthermore, photocatalysis shows more advantages to the other water treatment

methods because it is a single step reaction where organic pollutants is completely removed without further treatment. Moreover, photocatalytic degradation does not use any toxic oxidants unlike ozonation and Fenton's process where ozone gas, iron salt and hydrogen peroxides are used.

2.3. Photocatalytic Degradation

Photocatalysis is defined from the composite words "photo" and "catalysis" whereby it is a process where the compound increases the rate of chemical reaction in the system by lowering down the activation energy without the reactants being consumed or altered throughout the reaction in the presence of a light source. Photocatalysis is the acceleration of a reaction in the presence of a catalyst and source light. The positive electron hole in the valence electron can oxidize the OH^- or H_2O at the surface of the catalyst to produce a hydroxyl radical, $OH\cdot$ which acts as the oxidizing agent for organic pollutants. Moreover, the photon excited electron in the conduction band reacts with the oxygen molecules present in the system and the hydrogen ion, H^+ to reduced and form a superoxide radical, $O_2\cdot$ and hydro peroxide radical ($OOH\cdot$) respectively. The mechanism for the photocatalysis reaction for the production of the necessary radicals is shown below:

1) The irradiation of light on the semiconductor catalyst generates electron pairs with higher or equal energy to form electron hole pairs ($e^-_{CB} + h^+_{VB}$)

$$\text{Semiconductor catalyst} + \text{light} \rightarrow e_{CB}^{-} + h_{VB}^{+} \qquad 2.1$$

2) Photo-generated holes oxidized the water molecules and hydroxyl ions by irradiation of a light source to form hydroxyl radicals

$$h^+ + H_2O \rightarrow OH\cdot \quad 2.2$$

$$h^+ + OH^- \rightarrow OH\cdot \quad 2.3$$

3) Photo-generated electrons reduce the oxygen molecules in the system to form super oxide radicals to for further reaction to form hydrogen peroxide, H_2O_2

$$e^- + O_2 \rightarrow {O_2}^- \quad 2.4$$

$$H^+ + {O_2}^- \rightarrow HO_2\cdot \quad 2.5$$

$$HO_2\cdot + HO_2\cdot \rightarrow H_2O_2 + O_2 \quad 2.6$$

$${O_2}^-\cdot + HO_2\cdot \rightarrow {HO_2}^-\cdot + O_2 \quad 2.7$$

$${HO_2}^-\cdot + H^+ \rightarrow H_2O_2 \quad 2.8$$

4) Hydrogen peroxide, H_2O_2 undergoes further degradation with the anion oxide radical and electron to form hydroxyl radicals

$$H_2O_2 + {O_2}^-\cdot \rightarrow OH\cdot + OH^- + O_2 \quad 2.9$$

$$H_2O_2 + e^- \rightarrow OH\cdot + OH^- \quad 2.10$$

$$H_2O_2 + \text{light} \rightarrow 2OH\cdot \quad 2.11$$

5) Degradation of organic pollutants through a serious or redox reaction with the intermediates ($HO_2\cdot$, $OH\cdot$ and $O_2^{-}\cdot$) to produce harmless products like carbon dioxide, CO_2 and water, H_2O as seen in Equation 2.13.

$$OH \cdot + dye \rightarrow dye\ intermediate \quad 2.12$$

$$OH \cdot + dye\ intermediate \rightarrow H_2O + CO_2 + end\ products \quad 2.13$$

The hydroxyl radicals, oxide radicals and hydrogen peroxide acts as a non-selective oxidant which are capable of initiating a series of oxidation reaction of the organic molecules that undergoes free radical reactions that produce the dye intermediates. These dye intermediates will eventually undergo oxidative cleavage that results carbon dioxide, water and inorganic ions as the end product.

2.3.1. Photocatalyst

Transition metal compound have received much attention as catalysts for oxidation of dyes to degrade effectively to clean compounds such as CO_2 and H_2O. The wide band gap of transition metals (3.4 eV-4.0 eV) enables a high energy radiation to excite the electrons from the valence band. Photon energy of visible light is between 1.8 to 3.1 eV ranges, therefore further affirming that the transition metals possess sufficient band energy gap that can be overcome by electrons excited with visible light (Ozcan et al., 2007). Many different transition compound hybrids such as TiO_2 (Ozcan et al., 2007), ZnO (Wang et al., 2017a), ZnS (Reddy et al., 2017), CuO (Xu et al., 2017) and SnO_2 has been studied for photo-degradation. Additionally, catalyst selection has to be inexpensive, chemically and physically stable, environmental friendly and abundant. Figure 2.1 presents the schematic illustration of photocatalytic degradation of dyes.

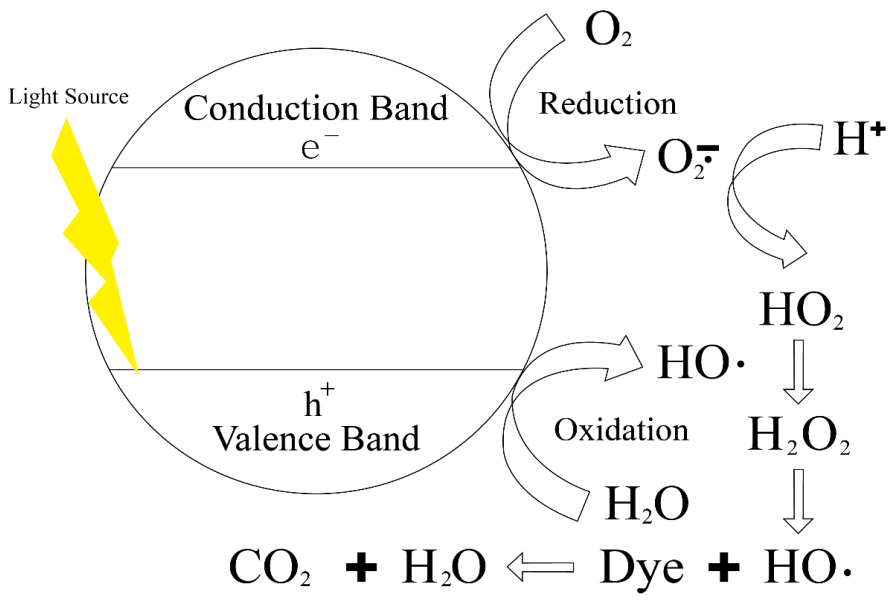

Figure 2.1: Illustration of mechanism of photocatalytic degradation of dyes

Furthermore, the general mechanism for photo-degradation of dyes can be summarize in four main steps.

1) Photo excitation of metals

$$MO + hv(UV) \rightarrow MO({e_{CB}}^{-} + {h_{VB}}^{+}) \quad 2.14$$

2) Oxygen ion adsorption

$$MO({e_{CB}}^{-}) + O_2 \rightarrow MO + \cdot {O_2}^{-} \quad 2.15$$

3) Ionization of water

$$MO\ ({h_{VB}}^{+}) + H_2O \rightarrow MO + H^{+} + OH\cdot \quad 2.16$$

$$MO\ ({h_{VB}}^{+}) + OH^{-} \rightarrow MO + OH\cdot \quad 2.17$$

$$\cdot O_2^- + H^+ \rightarrow HO_2 \cdot \quad 2.18$$

4) Protonation of superoxides

$$MO(e_{CB}^-) + HO_2 \cdot + H^+ \rightarrow H_2O_2 \quad 2.19$$

$$MO\ (h_{VB}^+) + Dye \rightarrow oxidation\ products\ (CO_2, H_2O, etc.) \quad 2.20$$

where, h_v is photon energy required to excite the semiconductor from the valence band (VB) region to the conduction band (CB) region and M denotes the metal of the photocatalyst.

Titania (TiO_2) and Zinc Oxide (ZnO) are of the early transition metals that most photocatalytic reactions were conducted because of their wide band gap in the near UV-spectral region that increases the oxidation rate and large free binding energy (Park, 2017). The main concern that dictates the efficiency of a photocatalyst is the thermodynamic and kinetic limitations of the semiconductor that promotes recombination and migration of electron hole pairs (Boyjoo et al., 2017). In order to reduce these limitations of TiO_2, a simple sol-gel process assisted with underwater discharge plasma treatment was used to synthesized nanoporous TiO_2 where the highest degradation efficiency was found to be >99 % for Reactive Black 5 dye due to the high BET surface area of the synthesized TiO_2 at 262.2 m^2/g as compared to 37.0 m^2/g for commercial TiO_2 (An et al., 2017). Another research utilized a mineral supported TiO_2 composite synthesized through a ball-milling method and calcinated at 300 ^oC for 6 hours to form a montmorillonite-TiO_2 nanocomposite to degrade methylene blue dye.

The results shows that photocatalytic activity of 90% TiO_2/montmorillonite display significant improvement of degradation rate as compared to pure TiO_2. This improvement was because the mineral reduced the agglomeration, thus enhancing the photocatalytic response ability (Liang et al., 2017). Furthermore, ZnO has also been successfully synthesized through a solvothermal method for the degradation of methyl orange dye under UV-light radiation.

It was determined that the high band gap of ZnO nano-spheres increases the separation of h^+ that makes it easier to form $O_2^{-}\cdot$ active ion and OH^- on the surface of the catalyst (Atchudan et al., 2017). As photocatalytic degradation is primarily occurs on the catalyst surface for the ionization of oxygen and water, the mass transfer limitation has to be minimized for effective application in photocatalysis. However, TiO_2 and ZnO have poor affinity toward organic pollutants, particularly hydrophobic organic pollutants. Therefore, the adsorption of organic pollutants on the surface is relatively low resulting in a slower photocatalytic degradation rate (Dong et al., 2015). Furthermore, the fast recombination between electron-hole pairs and the mismatch between the band gap of TiO_2 are other issues that are yet to be overcome (Hung et al., 2017).

2.3.2. Azo Dyes

Azo dyes are the most abundant groups of synthetic dyes. Azo dyes are classified due to having one or more azo bonds (-N=N-) (Zhang et al., 2010). The high solubility, low cost and abundance in variety of colour of azo dyes have attracted industry to utilize these dyes in a wide array of applications. The drawbacks of these azo-dyes are due to the non-biodegradable properties and the high solubility of the dyes make sludge

treatment and filtration method inadequate (Forgacs et al., 2004). The reduction cleavage of azo bond under anaerobic conditions will result in formation of aromatic amines that are highly toxic and carcinogenic, thus, biological treatment of azo dyes are also not favourable (Liu et al., 2011). Additionally, azo dyes maybe activated through direct oxidation of azo linkage to highly reactive electrophilic diazonium salts (Hu et al., 2011). However, photocatalytic application has been utilized by principle of redox reaction between the OH radical and oxygen anion to protonate the dyes to form harmless compounds such as carbon dioxide and water.

Photocataytic removal of reactive black dye and acid yellow have already been conducted in the past. A previous study investigate the efficiency of UV-A light emitting diodes for decolourisation of reactive black solutions in a continuous photoreactor (Ferreira et al., 2016). Titanium oxide was used as the photocatalyst to remove the reactive black dye. It was determined that decolourization of up to 89 % was achieved with 0.5 g/L of catalyst loading. Another research investigated the effects of pH on the removal of dye through photocatalytic reaction by using iron powder as the catalyst (Rahmani et al., 2010). It was determined that at high pH of 11, the highest removal percentage of reactive black dye under UV system was achieved. Furthermore, investigation on the removal of acid yellow dye was conducted by utilizing zinc oxide as the photocatalyst to remove acid yellow dye. It was determined that the most efficient pH level for photocatalytic decomposition was 8 and zinc oxide cannot be uses as a photocatalyst in an acidic solution of pH lower than 4 (Khezrianjoo and Revanasiddappa, 2013). Nonetheless, there are many studies available that utilize different types of photocatalyst to degrade the azo dye, however, exploiting nano nickel oxide as a

photocatalyst synthesized through proteic sol-gel method has not been reported to the author's knowledge.

2.3.3. Nickel Oxide Photocatalyst

Nickel oxide have been gaining much attention as of late because of their diversity and potential application in numerous fields such as, magnetic appliances (Davar et al., 2009), biomedicine (Muñoz and Costa, 2012), catalytic technology (Hu et al., 2015). Furthermore, there have been many report and research conducted on the manipulation of nano shapes of NiO, further evident on the potential application of NiO in the wide variety of nanotechnology. Nano sized nickel oxide can be classified as one-, two- and three- dimensional structure. One-dimensional structures are the most abundant group due to the simplicity of synthesizing and high surface – volume ratio. Examples of one-dimensional structures includes, nano-rods (Tao et al., 2016, Lee et al., 2016), -needles (Zhang et al., 2005), -whiskers (Miura, 2004), -wires (Wang et al., 2012) and –tubes (Lee et al., 2016). Nickel oxide that can be obtained in two-dimensional structures includes nano-sheet (Yu et al., 2015) and nano-wafers (Tao et al., 2016).

Many researchers have examined the usage of NiO as the catalyst for photocatalytic degradation. Separating the electron-hole recombination is a key factor in photocatalytic degradation and NiO has been shown to reduce the recombination process due to the high band gap and conduction band which shows excellent electrochemical stability (Soofivand and Salavati-Niasari, 2017). An electrodeposition technique in Choline Chloride and sol-gel method was used previously to synthesize NiO for the degradation of methyl orange, which shows favourable electrochromic

stability and degradation rates (Qi et al., 2015). Another research synthesize NiO microspheres through a solvo-thermal route followed by calcination process shows the excellent degradable ability to MB dye with almost 89.06 % removal rate (Qing et al., 2015). Additionally, it was proposed that by doping the p-type NiO with n-type NiO to form a p-n junction can effectively reduce the recombination of electron-hole pairs at the junction to enhance the photocatalytic activity of the catalyst (Vinoth et al., 2017).

Table 2.3: Summary of Synthesizing Routes for NiO nanoparticles

Photocatalyst	Structure	Synthesis method	Description	References
NiO	Nanoparticles of 1-2 nm	Electro deposition	Degradation of Methyl Orange dye under UV light with removal rate of 48 %	(Qi et al., 2015)
NiO	Microspheres	Solvothermal method	Degradation of Methylene blue under both UV light and visible light with removal rate of 89.06 %	(Qing et al., 2015)
NiO-TiO_2	Microspheres	Ultrasound assisted wet impregnation method	Degradation of Methyl Orange dye under visible light increases with higher loading of NiO wt. % with removal rate of 92 %.	(Vinoth et al., 2017)

2.3.4. Kinetics

The photo-degradation kinetics are vital to assess the performance of the photocatalyst to simulate the removal of organic materials in the natural environment. Due to the fact that adsorption is considered critical in heterogeneous photo-degradation, Langmuir-Hinshelwood model, which is similar to a pseudo first order model and pseudo second order model are used to describe the photo-degradation kinetics (Channei et al., 2017). The pseudo first order model assumes the rate of reaction is directly proportional to the difference in concentration of dyes and the amount of dye adsorbed with time as shown:

$$ln\frac{C_0}{C} = k_1 t$$

2.21

The pseudo second order model is based on the following equation:

$$\frac{1}{C} = k_2 t + \frac{1}{C_o}$$

2.22

where, C_0 is the adsorbance at specific time t and C is the initial dye adsorbance, k_1 and k_2 is pseudo first order and second order rate constant (min^{-1}) for degradation reactions respectively and t is the degradation time.

2.4. Nanoparticles Synthesis Methods

Metallic semiconductors and metal oxides have been gaining much interest due to their wide variety of applications in the field of medicine (Kristinaitytė et al., 2017), energy , environmental (Edralin et al., 2017) and catalyst due their unique and improved properties. The nanoscale dimensions of particles enhance chemical properties in thermal conductivity, catalytic reactivity, and chemical stability owing to its large surface area to volume ratio as compared to their bulk counterparts. However, formation of agglomeration tends to occur as energy levels and reactivity of nanoparticles increases with a decrease in particle size (Sodipo and Aziz, 2016).

As the surface area and particle size are one of the main parameter in determining the properties of nanoparticles, researcher (Ferreira et al., 2016) face an uphill task to

synthesize optimum nanoparticles with high surface to volume ratio with low agglomeration coupled. In addition, the properties of nanoparticles are also highly dependent on the growth mechanism such as temperature, pH, and concentration of reactants (Ramesh, 2013). The determinant conditions for the growth of nanoparticles change with different synthesis methods. Therefore, extensive research has been conducted to improve the synthesis routes of metal nanoparticles such as ZnO (Arslan and Abalı, 2017), TiO_2 (Wang et al., 2013), AgO (Shen et al., 2017), NiO (Abu-Zied et al., 2017) and MgO (Yang et al., 2017). The main aim of their research is to improve the crystallinity, morphological properties of the nano materials as well as obtaining a sustainable synthetic process. This section discusses on the various synthesizing methods of nanoparticles for different applications. The synthesis method can be separated to two different approach, which are bottom-up and top-down approaches.

2.4.1. Bottom-up Method

Bottom up approach seeks to arrange smaller components like atom of molecular constituents into more complex assembly by using chemical or physical forces operating at nanoscale to assemble basic units into larger structure (Haikal et al., 2017). Bottom up approach also known as wet chemical method, involves the condensation of molecules in a solvent to generate nanoparticles via crystallization. Nanoparticle size could be controlled by manipulating the processing parameters that influence the crystallite growth and nucleation of particles.

2.4.1.1. Sol-gel

Sol-gel method is based on the hydrolysis of metalorganic compound precursors, for example, metal alkoxides followed by polycondensation reaction to form a network of metal hydroxide. Subsequent drying and heating of the metal hydroxide polymerizes to form dense porous gel that leads to the production of nano-sized crystalline metal oxides (Stankic et al., 2016). Sol-gel method is a popular synthetic method with much interest in view of the simplicity, low cost, reliability and mild conditions of synthesis which utilizes low temperature and atmospheric pressure to form nanoparticles (Ramesh, 2013, Bhaskar et al., 2017, Papynov et al., 2017). Previous research has concluded that the low temperature conditons of sol-gel shows favourable morphological properties of the nanoparticles which is crucial as a degradation catalyst for decontamination of waste water (Mahato et al., 2009). Hydrolysis and condensation of alcohol and hydroxyl groups are the two most widely reported sol-gel synthesis method.

Previous research has successfully synthesize nickel oxide nanoparticles through sol-gel synthesis method by using basic nickel carbonate (BNC) and malic acid as the raw materials (Li et al., 2007). A wet gel was obtained by mixing the raw materials and stirring under temperature of 70 ^{o}C for 3 hours, subsequent calcination at 400 ^{o}C for 1 hour produce the nano-sized nickel oxide powder. The result of this research show that the synthesized NiO powder has an average particle size of 13 nm with narrow size distribution and weak agglomeration. Besides that, synthesis of nickel oxide nanoparticles by using nickel nitrate hexahydrate with isopropanol alcohol and polyethylene glycol as the hydrolysis agent have also showed favourable results where

high crystallinity particles was determine by XRD and morphological analysis showed a sample of ± 32.9 nm was obtained when calcinated at 450 ^{o}C.

2.4.1.2. Hydrothermal

Hydrothermal synthesis refers to the preparation of chemical reactions in an autoclave, where the reactants are heated gradually to a temperature range between 100 ^{o}C – 500 ^{o}C for a certain amount of time. This method can be described as a two-step mechanism where the hydrolysis of metal ions will form hydroxide intermediate which is then dehydrated to form the desired product (Sodipo and Aziz, 2016). The high temperature heating and subsequent cooling promotes the growth of crystal nuclei which will result in a high degree of crystallinity and high purity of the material (Biao et al., 2017). This method also eliminates the use of additional processing such as grinding or calcination that makes it a more simple and environmental friendly approach.

Previous research have already successfully employed hydrothermal method to synthesize Ag nanoparticles with average diameter of 10.0 ± 5.4 nm by utilizing chitosan as a stabilizer in a autoclave at 140 ^{o}C for 4 hours (Biao et al., 2017). However, conventional hydrothermal routes have shown to have a slow reaction kinetics at any given temperature. Researchers have proposed to use microwave heating during hydrothermal synthesis to increase the kinetics of crystallization because of the localized super heating of the solution (Sreeja and Joy, 2007). A comparative study between Ni and Zn ferrite powders were conducted between microwave hydrothermal reaction and conventional hydrothermal method at varying time and temperatures and it was concluded that Microwave-Hydrothermal reaction has a better crystallinity due to the

lower temperature and holding time (Lee et al., 2001). Another Microwave-Hydrothermal method was utilized to synthesize super magnetic Fe_2O_3 with an average particle size of 10 nm (Sreeja and Joy, 2007). Photo-degradation properties of hydrothermal synthesized Co-doped ZnS were also carried out previously, showing that the Co dopant concentration decreases the band gap of ZnS from 3.32 eV to 2.65 eV which enables stronger absorption of light. Furthermore, the Co dopant could act as an electron trapping agent which reduces the recombination of electron-hole pair (Wang et al., 2016b).

2.4.1.3. Controlled Precipitation

Controlled Precipitation is another route widely used to synthesize metal nanoparticles due to the possibility of obtaining products with repeatable properties. This method involves fast spontaneous reduction of a metal salt through a reducing agent in order to inhibit the growth of particles with specified dimensions, followed by ion exchange between the reactants and finally precipitation of a precursor from the solution (He et al., 2017). Further thermal treatment and milling is necessary for this method to remove the impurities to obtain a metal oxide product. Reaction time, temperature, reducing agent and pH (Wang et al., 2017b) are the main parameters affecting the morphology and crystallinity of the nano-product. However, calcination often results in high level of agglomerations depending on the parameters (Yang et al., 2017).

There is a report available mentioning successful synthesis of NiO nanoparticles, using controlled precipitation with Nickel Chloride Hexahydrate as the reducing agent,

with average crystalline size of 9 nm. Optical study of the NiO nanoparticles showed that the bandgap of the particle decreased with the increase in calcination temperature and crystallite size due to quantum confinement effect in the particle (Varunkumar et al., 2017a). Nanocomposite was also obtained through co-precipitation method where nickel oxide was combined with Zinc to form a shell-core composite that shows excellent soft magnetic properties (Peng et al., 2017). Furthermore, doping of ZnS with rare earth element, Gadolinium through co-precipitation has shown to improve the magnetic capability of the metal compound due to the localization of 4f orbitals that enables magnetic coupling through intra-ion 4f and 5d exchange (Kaur et al., 2017). Not only that, Zn-doped NiO powders prepared through co-precipitation method confirmed that a single phase Ni_xZn_xO was formed and the increasing amount of Zn dopant decreases the activation energy which improves the gas-sensing properties (Lontio Fomekong et al., 2016). The effects of pH was also studied to further understand the physicochemical properties of $Ce_{0.35}Zr_{0.55}(LaPr)_{0.1}O_2$ in the co-precipitation reaction. It was determine that the homogenous structure with best thermal stability and oxygen storage capability was at a pH=10 because of the changes in ionic charge or the compound (Wang et al., 2017b).

2.4.2. Top-down Method

Top down approach involves the breaking down of large macroscopic particle to create nanoparticles (Low et al., 2017). This approach usually encompasses physical methods to breaking the bulk materials through ball milling or laser ablation. The simple technique and low cost operating parameters are advantages to create a sustainable synthesis method for nanoparticle(Lermyte et al., 2015).

2.4.2.1. Ball Milling

Ball milling method has gained a lot of attention as a non-equilibrium solid-state process that results in metal oxides with nanoscale microstructure. The localized deformation of shear bands of the metal oxide contains a high dislocation density to form a cell or sub-grain structure with finer dimension (Cheng et al., 2017). Other than that, mechanical ball milling process could be carried out in room temperature through centrifugal forces or stirring action of an agitator. Parameters such as milling time, milling speed and weight ratio of ball to powder are the main factors that influences the characteristics of the powders (Kumar et al., 2014). However, common drawbacks of ball milling technique includes the, highly disperse size distribution and the contamination problems of the grinding media (Yang and Ding, 2012).

Many studies have been conducted recently and successfully utilize ball milling as a synthetic route to produce nanoparticles. It was determined that using pure ethanol as an additive to make a wet ball-milling process resulting in a Fe/Al flakes that have potential for making lightweight broad-band microwave absorbers that can be applied in a high frequency range of 12.2 GHz to 15.9 GHz (Yang and Ding, 2012) Furthermore, SiC powder was successfully reduced to nano-sized SiC powder via high energy planetary ball mill with improved reduction in particle size, permittivity and microwave absorption (Kumar et al., 2014). Other than that, nanocomposite was also successfully synthesized through ball milling technique with a heighten physiochemical properties of the nanoparticles. It was found that a mechanically milled MgH_2 with 5% Vanadium has shown to have better hydrogen sorption kinetics than the unmilled MgH_2 (Liang et al., 1999).

2.4.2.2. Laser Ablation

The principle of laser ablation has been described as the removal of material from a surface through laser irradiation. Nanoparticles are primarily obtained when the laser fluencies are higher than the threshold of the particles. The laser-target material interaction produces plasma consisting of ions, atoms and molecules at high temperature and pressure conditions (Navas et al., 2017). The high power of the laser beam induces large light absorption on the material surface, which results in an elevated temperature of the material that is vaporized into the laser plume. The high temperature and pressure difference between plasma and ambient liquid will cause a rapid expansion and cooling of plasma. This leads to the interactions between the liquid medium to produce nanoparticles through nucleation growth process. Hence, the advantage of this method is the morphology of the material, which can be manipulated by varying parameters such as wave length, surfactants and temperature of the liquid medium (Elsayed et al., 2013).

Recently, laser ablation has been employed widely for preparation of nanoparticles due to the simplicity of the method and absence of chemical reagents, and high purity of nanomaterial. However, the drawbacks includes the agglomeration and ejection of large fragments during laser ablation due to the difference in thermodynamic equilibrium of the process (Elsayed et al., 2013). ZnO was successfully synthesized through laser ablation method in water, ammonium nitrate and cetyltrimethyl ammonium bromide to form spherical, nano-flakes, nano-squares, nano-flowers and nano-rods.

It was determined that the directional growth and crystallinity were highly dependent on the plasma interaction with the surrounding medium. Temperature of the

liquid medium also showed significant influence in the structural growth of ZnO nanoparticles (Navas et al., 2017). Furthermore, Ag-Au core-shell nanoparticles were also successfully synthesized through laser ablation in water. It was determined an increase in the ablation duration leads to the growth and formation of core-shell particles with fine lattice spacing of 0.232 nm (Vinod and Gopchandran, 2015).

2.4.3. Compilation of Synthesis Methods

The explanations of nanoparticles synthesizing routes are summarized in Table 2.4. The field of nanotechnology has proved to be very enterprising in many industrial sectors such as biomedicine, wastewater treatment, catalytic reaction etc. A lot of extensive research has been conducted previously in the field of nanotechnology to determine optimal synthesizing conditions and materials used for industrial production of nanoparticles. Every synthesis route has shown to be able to produce nanoparticles previously. However, the main challenge that researchers are facing currently is the feasibility of a synthesis route being implemented in a large scale industrial process. The physiochemical properties, surface morphology, crystallinity and monodispersity of a nanoparticle are the main factors that show the functionality of the nanoparticles. Hence, a deeper understanding of synthesis routes is required for practicality in a sustainable long term process.

Table 2.4: Summary of Synthesizing Routes for nanoparticles

Method	Technique	Description	Advantages	Drawbacks	Ref
Bottom up	Hydrothermal	Heating of metal salt solution in high temperature and pressure in an autoclave with subsequent cooling for the growth of crystal nuclei	Further thermal treatment is not required. High degree of crystallinity in the nano product	Difficulty in controlling crystal growth because of slow reaction kinetics	(Sodipo and Aziz, 2016)
	Sol-gel	Hydrolysis of metal alkoxides followed by polycondensation to form dense porous gel that leads to the production of nano-sized crystalline metal oxides	High purity products, low energy and material cost, suitable for large scale synthesis	Time consuming to form the gel, formation of agglomeration due to calcination	(Stankic et al., 2016)
	Controlled Percipitation	Fast spontaneous reduction of a metal salt through a reducing agent in order followed by ion exchange between the reactants and precipitation of a precursor from the solution	Repeatable process with good consistency in nano products.	Formation of agglomeration due to calcination.	(He et al., 2017)
Top Down	Ball milling	Metallic precursor are grinded in a solvent with an agitator or grinding media to form nano sized particles	Operates at ambient conditions, suitable for large scale process	Highly disperse size distribution, contamination of grinding media	(Yang and Ding, 2012) (Cheng et al., 2017)

Laser Ablation	Removal of material surface through laser irradiation. Bulk target is immersed in a liquid media during laser ablation	Good control of particle size with adjustment of the laser, time efficient, low energy required	Laser technology is costly, high agglomeration because of the difference in thermodynamic equilibrium of the process	(Elsayed et al., 2013)

2.5. Green materials as a Template for Synthesis of Nanoparticles

Substituting conventional chemicals for natural occurring materials have been gaining attention because they are environmentally friendly, cost effective and does not use toxic or expensive organic solvents (Król et al., 2017). Green templates have strong reducing and chelating agents such as hydroxyl, carboxylic acid, alkoxide. Metal salts have high reduction potential because of the electron donating nature of anions for example, chlorides (Cl^-), sulphates (SO_4^-) and nitrites (NH_3^-). As a result of these factors, metal salt can be easily reduced into a more stable form by using green template such as gelatin, cellulose and biological extract.

Mechanism of green templating synthesis of metal nanoparticles can be described in a three step process. Firstly, metal ions are reduced by the strong reducing agents from the green materials to form metal atoms. The metal atoms thus undergo nucleation to reduce the remaining metal ions in the bulk solution (Imran Din and Rani, 2016a). Secondly, heterogeneous nucleation and growth of the metal ions further reduces the metal ion for spontaneous coalescence of the adjacent nanoparticles into larger size

nanoparticles. This step enhances the thermodynamic stability of the nanoparticles. Lastly, the metal nanoparticles are subjected to drying or calcination to form metal oxide nanoparticles. The final shape of nanoparticles are determined through this step (Calvache-Muñoz et al., 2017).

2.5.1. Biomaterials

Biological synthesis of nanoparticles is a method that incorporates certain parts of plants or plants extract, biomolecules to synthesize nanoparticles (Tanzil et al., 2016). Biological synthesis are gaining much interest because of the high reducing capability of secondary metabolites that are found in plants (Rasheed et al., 2017). Secondary metabolites such as flavonoids, phenols and glycosides contain high concentration of hydroxyl ions that easily donates electron to reduce the metal salts. Other than that, microbial bacteria are also another biological material that has been utilized to synthesize nanoparticles. Synthesis of nanoparticles through bacterial differs slightly with plants whereby the metal cation is reduced through electrostatic interactions between negatively charged cell wall of the bacteria and the positive charge metal cation. The enzyme that is released as a result from the interactions will then reduce the metal ions into metal atom that aggregate and form metal nanoparticles (Singh et al., 2015).

There are a lot of studies than have been conducted by using biomaterials to prepare metal nanoparticles. Silver nanoparticles of around 25 nm were successfully produced using the leave extract of Artemisia vulgaris without addition of any external reducing agent (Rasheed et al., 2017). Furthermore, a photocatalytic study for the degradation of Methyl orange and Congo red dye was conducted by using silver

nanoparticles synthesized through microbial bacteria (*Leuconostoc lactis*) reduction (Saravanan et al., 2017a). The study reports that silver nanoparticles was produced with an average size of 35 nm and the high surface area and hydrophilic nature of the microbial stabilized-silver nanoparticles showed efficient degradation of textile dyes. Synthesis of nickel oxide using *Coriandrum sativum* leaf extract through assisted microwave method was conducted previously with crystallite size in the range of 15 nm to 16 nm with potential catalytic activity (Azhagu Raj et al., 2017). Furthermore, gold nanoparticles of less than 10 nm was also successfully synthesized by using a sulphate-reducing bacteria (Tanzil et al., 2016). Cultivation parameters and the gold precursor were determined as factors that affect the size and morphology of the gold nanoparticles.

2.5.2. Chitosan

Chitosan is a copolymer of 1-4 linked β-D-glucosamine and N- acylated-D-glucose-2- amine. Chitosan is gaining interest because it is renewable, biocompatible, non-toxic and it is highly available in nature which allows a renewable low cost biomaterial. Because of these characteristics, chitosan can be applied in a wide array of application such as drug transfer, wastewater treatment and agricultural (Raghavendra et al., 2017). It is also reported that chitosan has excellent chelating ability because of abundant hydroxyl groups present in the molecular structure (Varma et al., 2004). Furthermore, the presence of amine group in the chitosan allows ease of crosslinking reaction to produce new derivatives. In another words, the O-H and N-H groups of chitosan are the main factors that act as reducing and stabilizing agents for intermolecular reaction with metal cations. This allows chitosan to be used as a precursor with metal salts to synthesize nanomaterials.

Chitosan has a drawback where precipitation of chitosan occurs in basic medium which makes it difficult for in situ synthesis of metal oxides. This is supported by the study comparing in situ and ex situ synthesis of cobalt spheres where ex situ exhibit superior structural and magnetic properties of cobalt nanoparticles (Briceño et al., 2017). Additionally, chitosan was determined as a coordination compound and soft template to produce copper oxide and zinc oxide nanocomposite for hollow nano-spheres (Witoon et al., 2013). Chitosan also exhibits the ability as a capping agents for ZnO:Na nanoparticle via wet chemical synthesis that leads to reduction in grain size from 16 nm to 13 nm (Safeera and Anila, 2017). Furthermore, flower-like copper oxide morphology was successfully synthesized using chitosan as a templating agent with excellent antibacterial activity against *E. coli* (Raghavendra et al., 2017). The same study also reported great catalytic activity of flower-like copper oxide for the reduction of 4-nitrophenol to 4-aminophenol.

2.5.3. Alginate

Alginate is a carbohydrate block copolymer that is obtained from brown marine algae. The natural occurring alginate consist of linear copolymers of two different monomers comprising 1-4 linked of β-D mannuronic acid and α-L guluronic acid in a homopolymeric block sequence (Narayanan and Han, 2017). Alginate is mainly used in bioengineering and pharmaceutical because of its low toxicity and biocompatible nature (Sood et al., 2017). The solubility, hydrophilicity and chemical properties of alginate can be manipulated through the addition of new functional groups into the alginate molecular structure (Pawar and Edgar, 2012). Furthermore, the oxygen rich chemical

structure of alginate can effectively cap the synthesized metal nanoparticles to prevent aggregation (Dey et al., 2016).

A previous research concludes that iron oxide-gold core shell nanoparticles were synthesized with thiolate sodium alginate template shows potential for drug delivery because of the encapsulation efficiency of the nanoparticles (Sood et al., 2017). Other than that, silver nanoparticles produced using sodium alginate as a stabilizing and reducing agent yields spherical nanoparticles of less than 25 nm with uniform particle size distribution (Zhao et al., 2014). It was determined that the silver nitrate concentration, sodium alginate concentration and pH levels of the solution have a significant impact on the particle size distribution and morphology of the silver nanoparticles. Not only that, sodium alginate has also been used as a green template for solvothermal synthesis of gold nanoparticles for catalytic reduction of 4-nitrophenol. The results show that catalytic activities and rate constants is related to the total surface area of gold nanoparticles where the higher amount of gold nanoparticles and smaller particle size will increase catalytic activity (Zhao et al., 2017).

2.5.4. Gelatin

Gelatin, a polysaccharide is another alternative to use as a raw material attributing to its advantages such as high water absorption, biodegradability and non-toxicity (Fan and Wang, 2016, dos Santos et al., 2016a, Imran Din and Rani, 2016b). Application of gelatin includes food, chemical, pharmaceutical and biological industries. Gelatin being the more thermally, chemical stable and hydrophilic theoretically shows more promising prospects in the synthesis of nanoparticles as compared to other biomaterials. Gelatin

can exist in different matter based on the temperature, liquid form at high temperature and solid form at low temperature. Moreover, free carboxyl groups makes up the backbone of the gelatin, which improves the potential for chelating and reducing transition metal compound. The amine-groups in the molecular structure of gelatin (Figure 2.2) is also a useful cross-linker with metal salts to form hydrogels precursor (Amonpattaratkit et al., 2017)

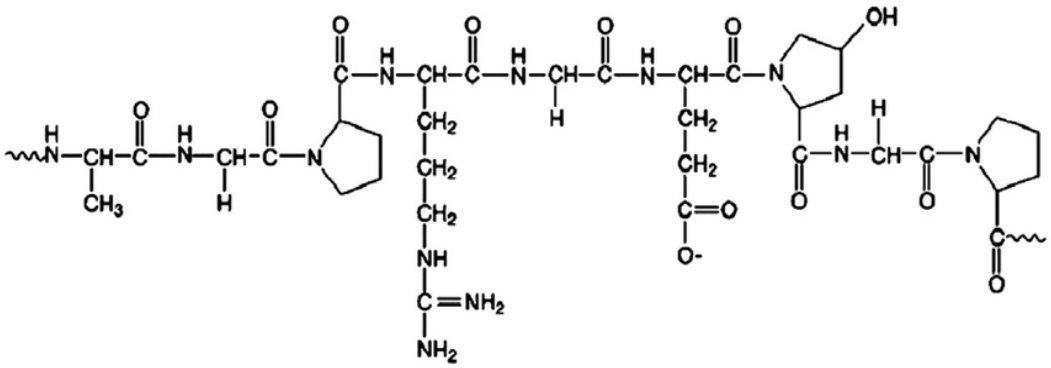

Figure 2.2: Molecular structure of gelatin

Additionally, utilizing gelatin as a precursor combining it with a metal salt to obtain nanoparticles has been reported with favourable results. Nanoparticles of Chromium oxide, Cr_2O_3 were obtain by synthesizing gelatin with Chrome alum with a particle size in the range of 15-60 nm (Medeiros et al., 2004). On top of that, synthesizing and modifying of gelatin into nano-gels as a drug carrier have been reported by Fan et al. (Fan and Wang, 2016) and Patra et al. (Patra et al., 2016) with nanoparticles of 96.7 nm and 55.67 nm, respectively. Not only that, a previous study reported on replacing polysaccharides with gelatin to stabilize palladium nanoparticles

without any addition of reducing agent and a face-centered cube crystalline palladium nanoparticle in the range of 2-5 nm was obtained (Khazaei et al., 2015).

2.6. Proteic Sol-gel

A new novel sol-gel synthesis route, Proteic sol-gel can be mentioned where it utilized an organic precursor in place of alkoxides or alcohol. Organic protein such as coconut water solution (de Paiva et al., 2009) have been reported for synthesis of nanoparticles with favourable results in terms of magnetic properties, purity and particle size. Proteic sol – gel method appears to be a promising synthesizing method due to its organic nature, which coincide with green technology. Proteic sol – gel method is classified as a top – down approach synthesis for nanoparticles (Ghazali et al., 2016). This method encompasses the hydrolysis of the gelatin followed by polymerization of the nickel acetate to form a network of gelatin – nickel acetate. Proteic sol – gel is altered compared to the conventional synthetic route where condensation is not required to form a gel, drying is conducted instead to remove all the water molecules which subsequently forms a xerogel. Moreover, this method can be seen as a clean, green and surfactant free method to synthesize high quality nickel oxide nanoparticles.

2.7. Summary

Essentially, Nickel oxide was selected as the metal oxide to produce nanoparticles for photocatalytic application. Comparing Nickel with other conventional metal such as titanium oxide and zinc oxide, the wide band gap and lower cost of nickel oxide shows better potential (Xu and Xu, 2015). Furthermore, the high negativity potential of Ni (E^o = -0.23 V) is more negative than the potential of H^+ ions, which favors transfer of

photogenerated electrons. More hydroxyl radicals are formed as a result, which accelerates the rate of photocatalytic reactions (Wang et al., 2015).

Other than that, sol-gel was selected as the synthesis method to produce nickel oxide nanoparticles. Selection of synthesis route was based on the high purity the nanoparticles produced from sol-gel method, with low agglomeration and simplicity of the method. Sol-gel method does not require high temperature or pressure during reactions and subsequent thermal treatment can be controlled to obtain good morphological nickel oxide nanoparticles. Gelatin was used as the templating agent as compared to conventional chemicals like alcohols or alkoxides. Gelatin is widely available, biocompatible and naturally occurring product that makes it an environmental friendly material for synthesis of nanoparticles. Furthermore, gelatin shows a great potential because of the carboxyl compounds present in the molecule that is a good chelating agent to hydrolyse metal salt. Nonetheless, a detailed study is required for all the parameters that are affecting the morphology, crystallinity and particle size distribution in order to determine the optimum conditions for synthesis of NiO nanoparticles. The properties of the NiO nanoparticles will be examined by photocatalytic degradation of RB5 and AY25 dyes to provide a more in depth study in the photocatalytic behavior of different azo dyes.

CHAPTER 3

MATERIAL AND METHODS

3.1. Background

In this chapter, the experimental procedures are described. The chapter also outlines the chemicals used in the study as well as their origin and purity together with the analytical instruments used. The preliminary stage of this research focuses on a sol-gel synthesis and characterization of nano-sized nickel oxide for further preparation as a catalyst used for photocatalytic activity. Nano-sized nickel oxide is synthesized via sol-gel method followed by thermal treating at controlled conditions. The final stage of the project plan comprises of fabricating a photocatalytic reactor that was used to conduct the photocatalytic activity on the degradation of dyes. The optimized synthesis variables of the nano-sized nickel oxide are used to test the on two different dyes, i.e: Reactive Black 5 and Acid Yellow 25 in order to have a better understanding on the catalytic activity of the synthesized nano nickel oxide particles. The structure of experiments will be carried out based on the flow chart presented in Figure 3.1.

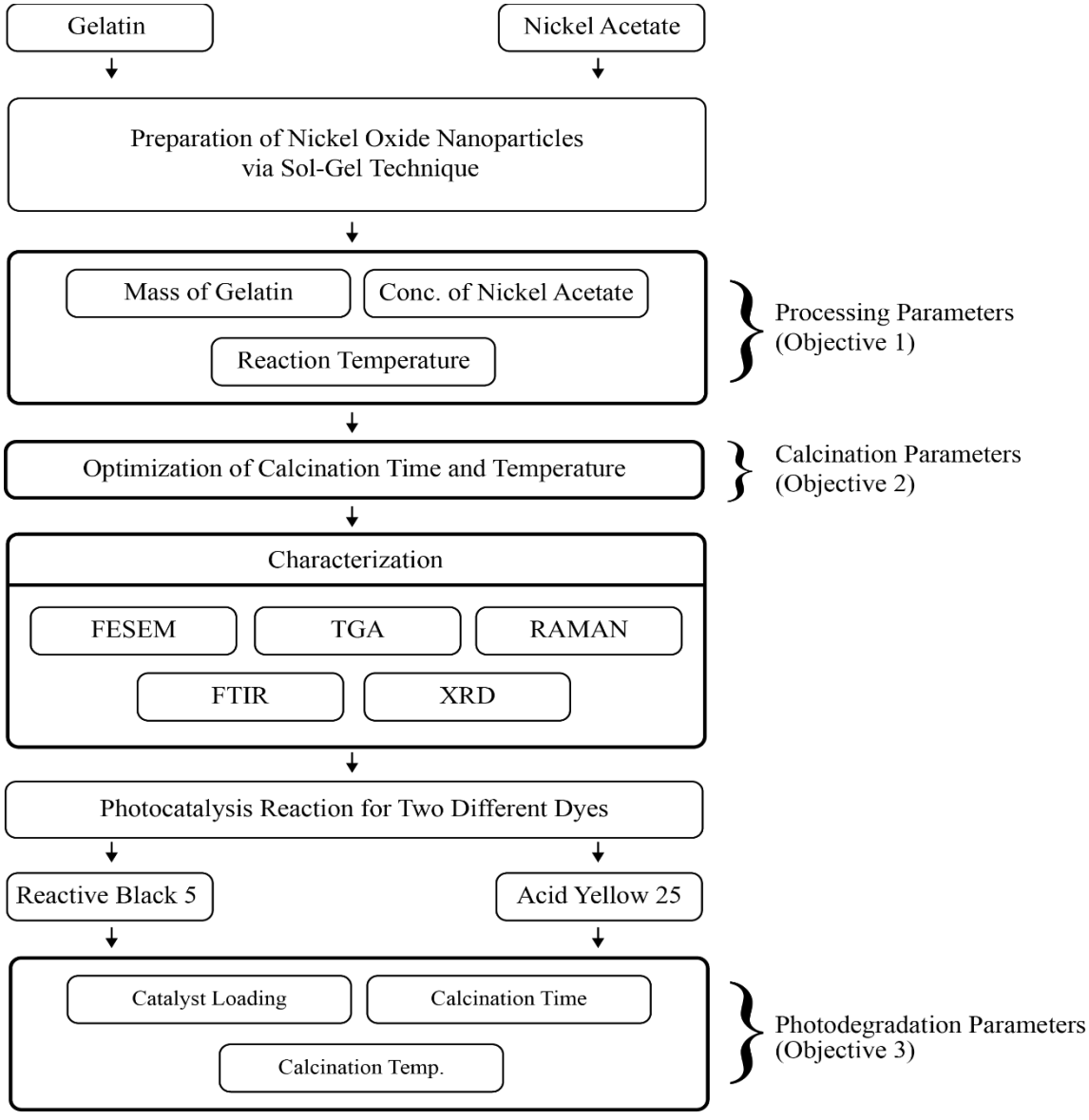

Figure 3.1: Experiment flow chart

3.2. Materials

Nickel nitrate tetrahydrate ($Ni(OCOCH_3)_2 \cdot 4H_2O$) of molecular weight 248.84 g/mol and gelatin from bovine skin supplied by Sigma-Aldrich were used in this sol-gel

synthesis process. Other than that, Reactive Black 5 ($C_{26}H_{25}N_5O_{19}S_6Na_4$) with dye content of 55 % and Acid Yellow 25 ($C_{23}H_{20}N_5NaO_6S_2$) with dye content of 40 % were also purchased from Sigma-Aldrich. All the chemicals used were of analytical grade without any further purification.

3.3. Synthesis of Nickel Oxide Powder

The syntheses of the samples were performed through sol-gel method. The first preliminary stage was separated into two parts in order to optimize the nickel oxide nanoparticles that were used to study the photocatalytic activity in the degradation of dyes. The first part of the study focused on optimization of the "sol" under controlled conditions (reaction temperature, calcination time and calcination temperature). Concentration of nickel acetate was studied first due to the lack of stoichiometric data of the gel, which prohibits the stoichiometric calculation between nickel acetate and gelatin. Stoichiometric ratio between nickel acetate and gelatin could not be accomplish due to the difference in units of the compounds as gelatin does not have an exact molar mass for calculation. Reaction temperature was set at a constant temperature of 80^{o}C throughout all the experiments. The temperature was fixed because gelatin from bovine will dissolve completely and polymerize with nickel acetate at this temperature. Reaction time was manipulated in order to determine the shortest achievable time for a highly homogenous reaction.

The second part of the preliminary studies included the calcination time and temperature. The optimized conditions for "sol" were used as the basis for this study. Calcination time and temperature were studied in order to determine which condition

yields the highest purity and smallest size distribution for the nano-sized nickel oxide particles. Figure 3.2 demonstrates a graphical image of the sole-gel reaction

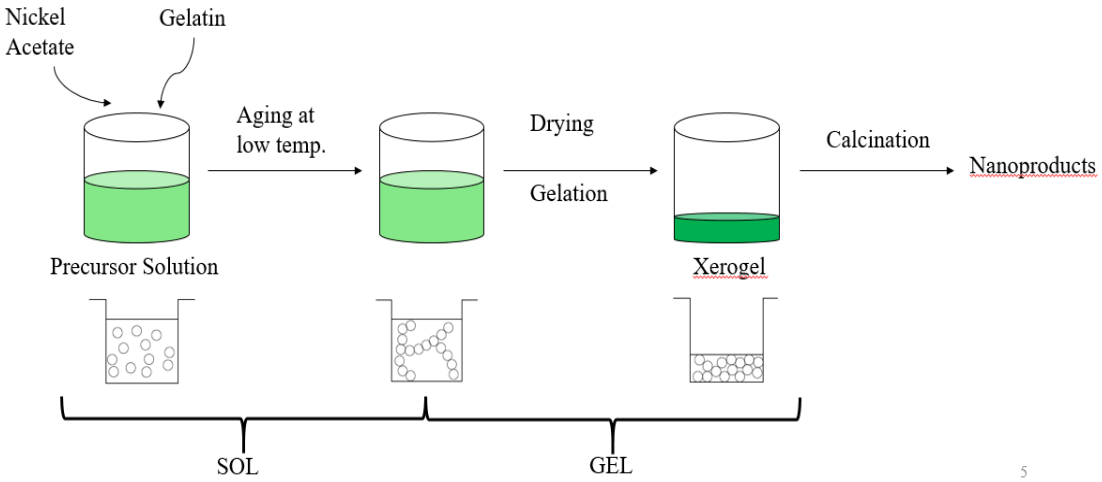

Figure 3.2: Schematic expression of sol-gel reaction

3.3.1. Sol Reaction

Concentration of Nickel Acetate is the first parameter that was being studied in this research due to the insufficient stoichiometric data of gelatin. Four different concentration of nickel acetate at 0.5 mol, 0.75 mol, 1.0 mol, 1.25 mol and four different mass of gelatin of 2 g, 1.5 g, 1 g and 0.5 g of gelatin were studied. The respective concentration of nickel acetate was first diluted in 30 ml of distilled water on a magnetic stirrer, forming a green solution. Gelatin solution was prepared by dissolving the desired mass of gelatin into 170 ml of distilled water under stirring conditions, forming a cloudy solution. Both the solutions were then heated to 80 ^{o}C. After that, the solutions was

mixed together into a beaker and stirred for 24 hours at 80 ºC to ensure complete immobilization of the gelatin and nickel acetate (Figure 3.3).

Figure 3.3: Sol solution of nickel acetate-gelatin

After 24 hours, the mixture was allowed to cool until room temperature before being placed inside an oven to dry out the remaining water at 60 ºC for 48 h forming a xerogel. The product was grinded in a pestle and mortar to form a green powder. The nickel acetate – gel polymer was transferred into a calcination boat and placed in a furnace at 500 ºC with a ramping rate of 2 ºC/min for calcination. Nickel oxide powder was formed as the end product of this procedure. Reaction time was manipulated after determining the best ratio of nickel acetate and gelatin. 0.5 mol of nickel acetate and 1 g of gelatin were dissolved in 30 ml and 170 ml of distilled water, respectively and heated to 80 ºC prior mixing of both the solution. Reaction time was manipulated at 6 to 24 h with intervals of 6 h. The xerogel (Figure 3.4) was then dried at 60 ºC for 48 h in an oven. The powder nickel oxide precursor samples was calcined at a temperature of 500

^{o}C with calcination time being set at 2 h. Ramping rate was set at 2 ^{o}C/min for all the reaction time parameters.

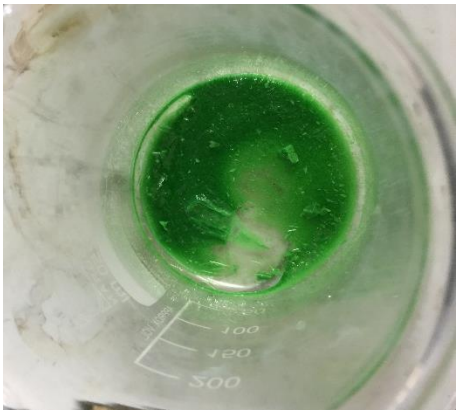

Figure 3.4: Xerogel of nickel oxide precursor

3.3.2. Calcination Time and Temperature

0.5 mol of nickel acetate and 1 g of gelatin were dissolved separately in 30 ml of distilled water and 170 ml of distilled water respectively and heated to 80 ^{o}C prior mixing of both the solution. Reaction time was set at 6 hours and 80 ^{o}C. After that, the resulting mixture in the beaker was allowed to cool until thermal equilibrium. The xerogel was then dried at 60 ^{o}C for 48 hours in an oven. The powder nickel oxide precursor samples was sent for calcination in a furnace at a temperature of 400 ^{o}C, 500 ^{o}C, 600 ^{o}C and 700 ^{o}C with calcination time being set at 2 to 8 h with intervals of 2 h. Ramping rate is set at 2 ^{o}C/min for all the calcination parameters.

3.4. Characterization of NiO nanoparticles

Characterization techniques were performed on the Nickel oxide nanoparticles to determine particle size, morphology, crystallinity as well as the physicochemical properties of the NiO nanoparticles

3.4.1. Thermalgravimetric Analaysis (TGA)

The nickel acetate – gelatin polymer, precursor of nickel oxide powder were examined using a thermo-gravimetric analyzer (TGA Q-50, TA Instruments, USA) to determine the thermal stability of the samples. The samples were heated from 25 ^{o}C to 800 ^{o}C with a heating rate of 5 ^{o}C/min in air atmosphere. The results from TGA were plotted to determine the degradation trend of the nickel acetate – gelatin polymer.

3.4.2. Microstructural Analysis

The microstructure of the powder specimens was examined using a field emission scanning electron microscope, FESEM (Hitachi Ultra-high resolution SU8010, Japan). The specimens were subjected to platinum coating using a coater (Quarum Q150R S, UK) prior to conducting microstructural analysis.

3.4.3. Fourier Transform Infrared Spectra (FTIR)

The Fourier transform infrared spectra (FTIR) test was carried out to determine the interactions of functional groups and analyze the chemical bonds of the final powder specimens. The FTIR spectra were obtained in the range of 4000 to 500 cm^{-1} (recorded at 0.4 cm^{-1} resolution and averaged by 64 scans) under transmittance mode using ATR technique.

3.4.4. X-Ray Diffractogram Analysis (XRD)

The crystal structure of the powder specimens was observed by using X-ray Diffraction (Bruker D8 Discover, Germany) at room temperature. The specimens were subjected to Cu-Kα radiation to obtain the diffraction peaks, which corresponded to the crystalline structure of the powder. Scherrer equation was then used to estimate the crystallite sizes of the synthesized product as shown in equation 3.1.

$$L = \frac{k\lambda}{\beta \cos\theta} \qquad 3.1$$

3.4.5. RAMAN Spectroscopy

Raman spectroscopy of nickel oxide powder at varying reaction conditions were carried out over the range of 200 to 1800 cm^{-1} using a Raman Spectrometer (Horiba LabRam HR evolution, Japan). A frequency doubled $Nd.VO_4$ diode pumped solid state laser with excitation of 532 nm was used to obtain the Raman spectra of the samples.

3.5. Photocatalytic Reactor

The photocatalytic reactions were studied in a fabricated polycarbonate plastic reactor with a volume of 500 ml. Initially, white paint was used to coat the interior to maintain a uniform light distribution throughout the dyes and aluminum foil was wrapped around the reactor in order to prevent any light from escaping the reactor and also to reflect back any light that manage to permeate the coating as presented in Figure 3.5. The reactor is fitted with a 24.5 cm long and 2.5 cm in diameter 11 W ultraviolet

lamp (Aquanice, Malaysia) as the primary light source for the photo-degradation of dyes. The experimental equipment used in this study are presented in Figure 3.5.

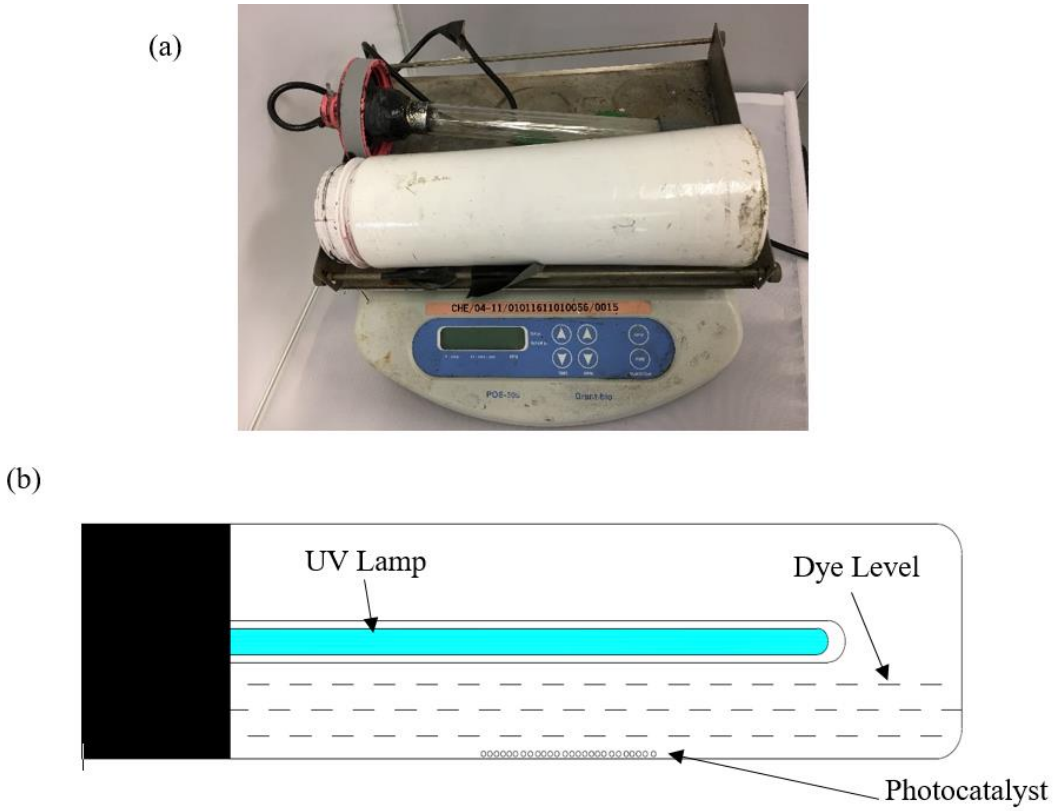

Figure 3.5: (a) Photo-degradation reactor setup and (b) Schemetic Diagram of Photodegradation Reactor

3.5.1. Photocatalytic Reactor

The photocatalytic activity of the synthesized NiO nanoparticles was investigated by using Reactive Black 5 (RB5) dye and Acid Yellow 25 (AY25) dye. Stock solutions of RB5 and AY25 were prepared at concentration of 100 ppm throughout all the photo-degradation experiments.

Investigation on the effect of catalyst loading were carried out in batch studies with catalyst mass of 0 g, 0.1 g, 0.25 g, 0.5 g, 0.75 g and 1.0 g for both Acid Yellow 25 and Reactive Black 5 dye. Other than that, the effects of calcination temperature and time of the synthesized nickel oxide nanoparticles on photo-degradation were studied with a fixed mass of catalyst of 0.75 g for RB5 and 0.5 g for AY25. Nickel oxide nanoparticles with calcination temperature of 500 ^{o}C, 600 ^{o}C and 700 ^{o}C and calcination time of 2 hours, 4 hours and 6 hours were studied. Photocatalytic reaction without presence of light was conducted on the best parameter to further understand and compare the adsorption capability of RB5 and AY25.

All the samples were obtained using a micropipette (Eppendorf, USA) at an interval of 10 minutes until 120 minutes and the dye was centrifuged at 6000 rpm for 10 minutes and removed using a syringe filter with a pore size of 0.12 μm (Merck, Malaysia) to remove any suspended particles from the dye sample. The sample was then analyzed using a UV-vis spectrometer (Thermo Genesys 10UV, USA) at a wavelength of 597 nm for RB5 and 392 nm for AY25 to determine the absorbance of the respective dyes at the particular interval.

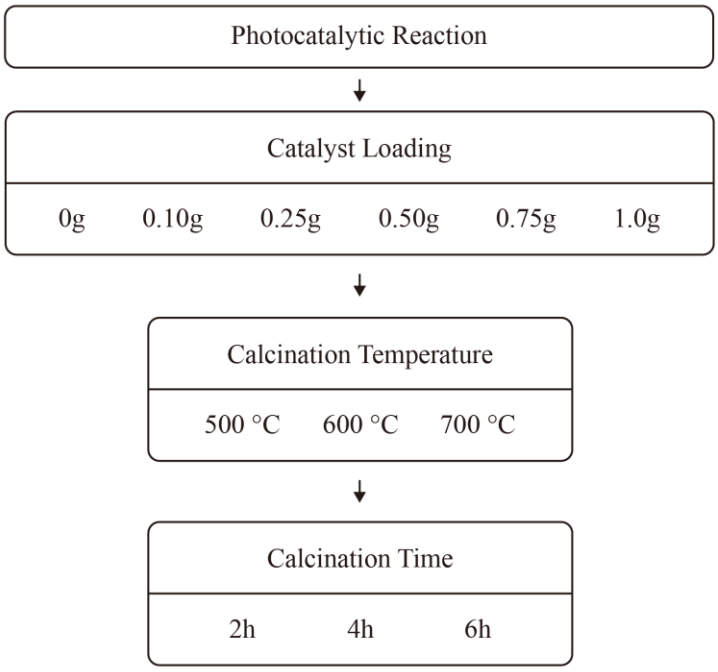

Figure 3.6: Flow chart for Photocatalytic Reaction

3.5.2. UV-visible Spectrophotometer (UV-vis)

UV-vis spectrometer (Thermo Genesys 10UV, USA) was utilized at a wavelength of 597 nm for RB5 and 392 nm for AY25 to determine the absorbance of the respective dyes at the particular interval with varying reaction parameter. According to Beer-Lambert law, the value of absorbance is proportional to the chemical concentration, thus, concentrations of the dye in any specific sample can be measured through absorbance measurements.

CHAPTER 4

RESULT AND DISCUSSION

4.1. Introduction

This chapter presents the results and in depth discussion of this research work. Nano-sized nickel oxide was synthesized from nickel acetate tetrahydrate using gelatin as a precursor through sol-gel method followed by calcination in an air furnace. Two set of optimization parameter were conducted. Firstly, manipulating the "sol" reaction conditions were carried out followed by calcination conditions to enhance the chemical and physical properties of the resulting NiO nanopowder. Sol reaction was studied first to optimize the properties of xerogel for further calcination to form NiO nanoparticles. Calcination conditions were manipulated after optimizing the sol parameters to yield the best NiO nanoparticle in terms of morphology, particle size and purity. A series of characterization that includes, TGA, FESEM, RAMAN, XRD and FTIR were conducted to determine the optimum processing conditions to obtain high quality nickel oxide nanoparticles. Photo-degradation performance of the synthesized NiO catalyst was determine based on the photo-degradation of RB5 and AY25 dyes under UV irradiation with varying parameters such as catalyst loading, calcination time and calcination temperature. Finally, the comparisons between the dyes was also investigated and compared with previous studies.

4.2. Sol Reaction

Three parameters were studied in the "sol" reaction, which are molarity of nickel acetate, mass of gelatin and reaction time. Each of these parameter were studied by varying one parameter at a time while keeping the other values constant. Thermogravimetric Analysis (TGA) was conducted first to determine the baseline for calcination conditions. FESEM images and XRD analysis were conducted to determine the optimum value of each parameter that will be used to proceed.

4.2.1. Thermogravimetric Analysis (TGA)

Thermalgravimetric analysis on the nickel acetate-gel polymer was carried out to determine the appropriate calcination conditions of NiO. Figure 4.1 shows the TGA results for NiO with the mixing ratio of 0.5 mol of nickel sulphate and 1 g of gel as the starting material.

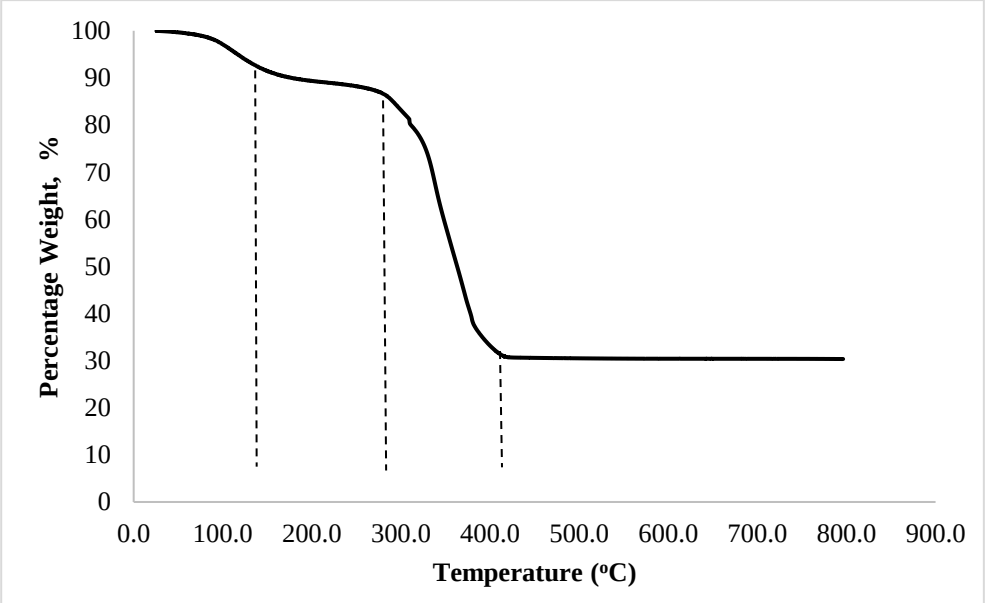

Figure 4.1: Thermal degradation of sol-gel precursor to form NiO

It was observed that the thermal degradation for the samples are separated into three different stages that are related to weight loss (Shankar et al., 2015). From 25 ^{o}C to 100 ^{o}C, a total of 9.63 % of mass loss occurred, which is attributed to the evaporation of moisture that was present at the surface of the sample. The second stage, from 100 ^{o}C to 270 ^{o}C a total of 3.07 % of mass loss was observed. This is attributed to the water desorption process and breakage of O-H bonds present in the sample, removing all the water present in the sample.

The third stage, from 270 ^{o}C to 420 ^{o}C a mass loss of 56.9 % ensued due to the decomposition of organic compound in the sample. Nitrate decomposition and biomaterial degradation occurred from the oxidation process and carbon monoxide and carbon dioxide are released as a byproduct (dos Santos et al., 2016a). No significant drop in mass was observed after 420 ^{o}C and the sample remained at 30.8 % of the initial mass. Hence, it can be concluded that nickel oxide will form with all the biomaterial decomposed with a calcination temperature of more than 420 ^{o}C, therefore, justifying the usage of 500 ^{o}C as the based point of calcination temperature prior to optimizing the processing parameters.

4.2.2. Microstructural Analysis

FESEM images of each processing parameters such as, molarity of nickel acetate, mass of gelatin and reaction time were obtained to analyze and determine the optimum processing variable for NiO nanoparticles.

4.2.2.1 Molarity of Nickel Acetate

FESEM images of NiO samples synthesized with different molarity of nickel acetate are shown in Figure 4.2. Reaction temperature, reaction time, calcination temperature and calcination time were set at constant levels of 80 ^{o}C, 24 h, 500 ^{o}C and 2 h, respectively. 2.0 g of gelatin used as the starting material for all the experiments conducted. It can be observed that NiO synthesized were spherical shape with nano-sized particles ranging from 15.0 nm to 50.4 nm.

From Figure 4.2, a trend could be noted with an increase of particle size in conjunction with the increase of molarity of nickel acetate used. Reason for this occurrence is due to the oxidation of precursor in presence of excess amount of nickel acetate during calcination, which accelerates the hydrolysis rate. This subsequently results in a larger distribution of NiO nanoparticles. It can also be noted that isolated nanoparticles were obtained with an increase of nickel acetate concentration, whereas, a more coalescence nanoparticles were obtained with lower concentration of nickel acetate as seen in Figure 4.2 (c), Figure 4.2 (d) and Figure 4.2 (a), Figure 4.2 (b) respectively.

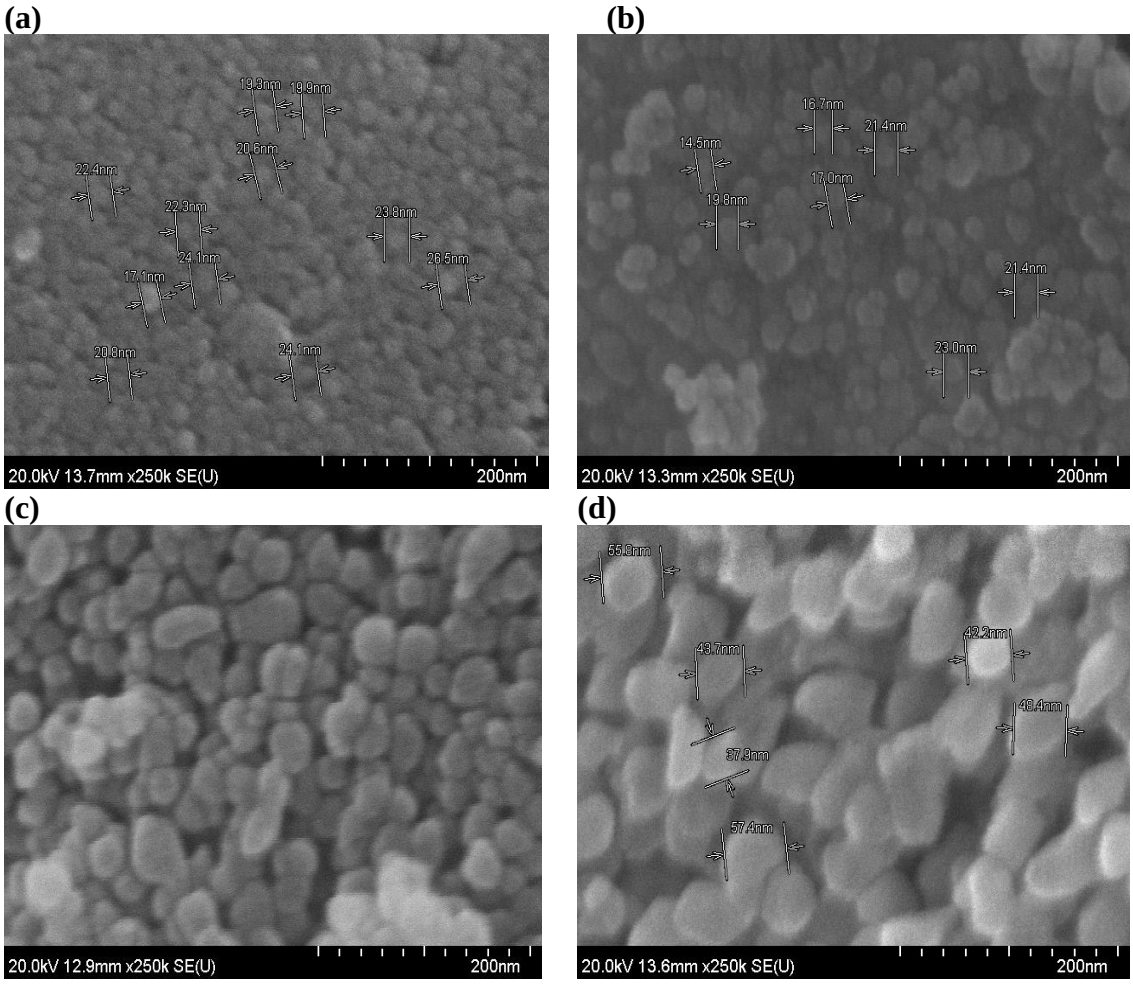

Figure 4.2: Comparison of surface morphology for NiO at (a) 0.5 mol, (b) 0.75 mol, (c) 1.0 mol and (d) 1.25 mol of Nickel acetate combining with 2 g of gelatin as the starting materials

4.2.2.2 Mass of Gelatin

The surface morphology of NiO samples synthesized with different mass of gelatin was compared with the concentration of nickel acetate being kept constant of 0.5 mol for all the various mass of gelatin. Agglomeration of nano nickel oxide and flaky shaped particles were observed with the alteration of mass of gelatin. Agglomerations in Figure 4.3 (a) are noticeably more severe with agglomeration size of more than 50 nm as compared to the rest of the samples. This is due to insufficient amount of gelatin used with nickel acetate to accelerate the hydrolysis, resulting in more agglomerated particles (Palanisamy, 2008). Figure 4.3 (b) and Figure 4.3 (d) show the best results out of the four in terms of agglomeration and particle size. This shows that 1.0 g and 2.0 g mass of gelatin yields are the appropriate ratio to mix with nickel acetate for synthesis of nickel oxide nanoparticles. However, it can be observed that 1.0 g of gelatin yields a smaller particle size of 15.0 nm compared to 2.0 g of gelatin at 19.3 nm. In addition, lower agglomeration was observed when 1.0 g of gelatin was used. This occurrence can be attributed to the high amount of gelatin that increases the nucleation growth of particle which results in a larger particle size (Al-Sehemi et al., 2014). Hence, 1.0 g of gelatin combined with 0.5 mol was determined as desired ratio for continuation of this study.

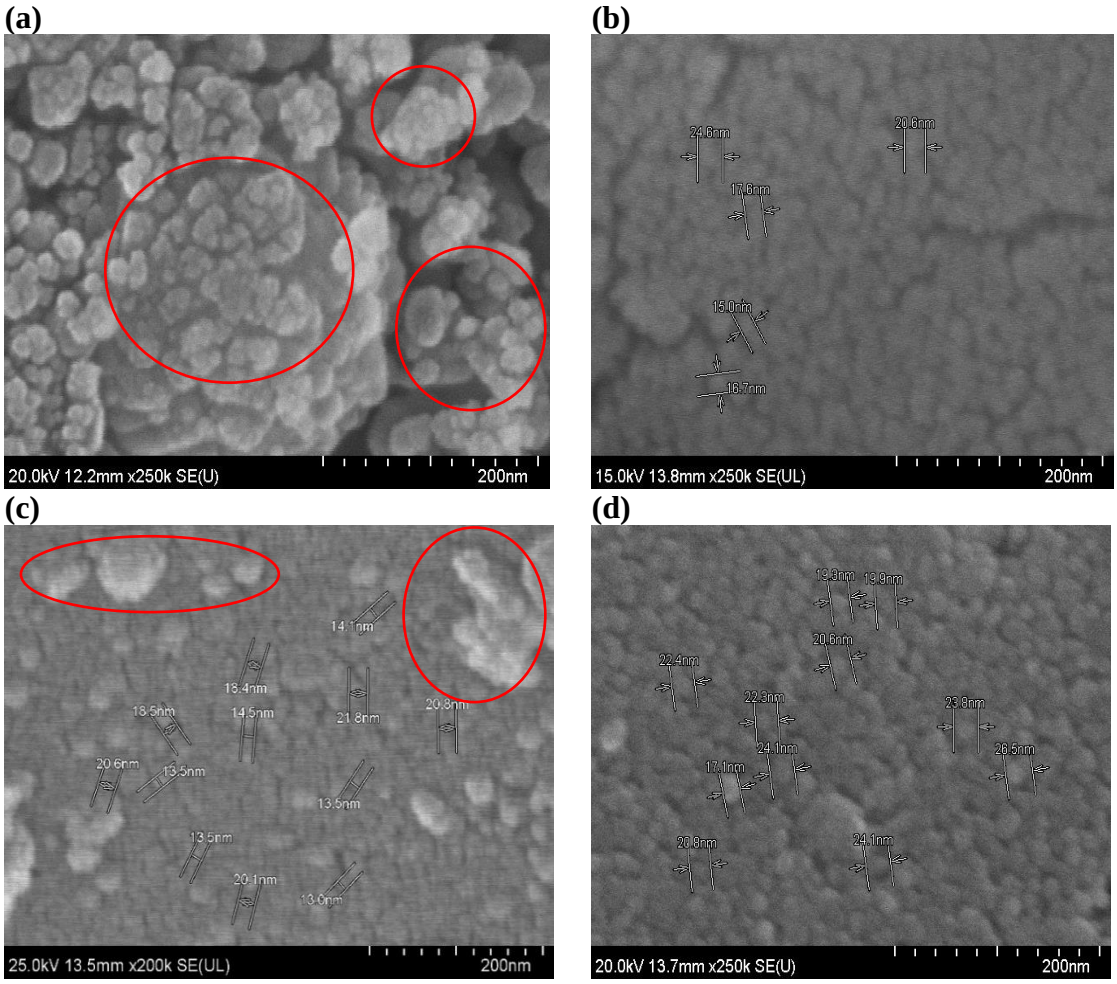

Figure 4.3: Comparison of surface morphology for NiO at (a) 0.5g, (b) 1.0g, (c) 1.5g and (d) 2g of gelatin combining with 0.5mol of nickel acetate as the starting materials

4.2.2.3 Reaction Time

Reaction time on the surface morphology of NiO was investigated with 0.5 mol of nickel acetate and 1 g of gelatin varying at 6 h to 24 h with intervals of 6 h. Gelatin and nickel acetate must have sufficient time to allow a high homogeneity sol-gel reaction. However, increasing the reaction time results in more severe agglomeration and larger particle size. It can be noted that agglomeration occurred for all the samples in Figure 4.4. Nonetheless, homogeneity of nanoparticles was already achieve by having reaction

time of 6 h showing the smallest particle size as compared to the longer reaction durations of 12 h, 18 h and 24 h. Therefore, reaction time was found to be at 6 h where all particles were spherical with the size range of 12.4 nm to 20.2 nm.

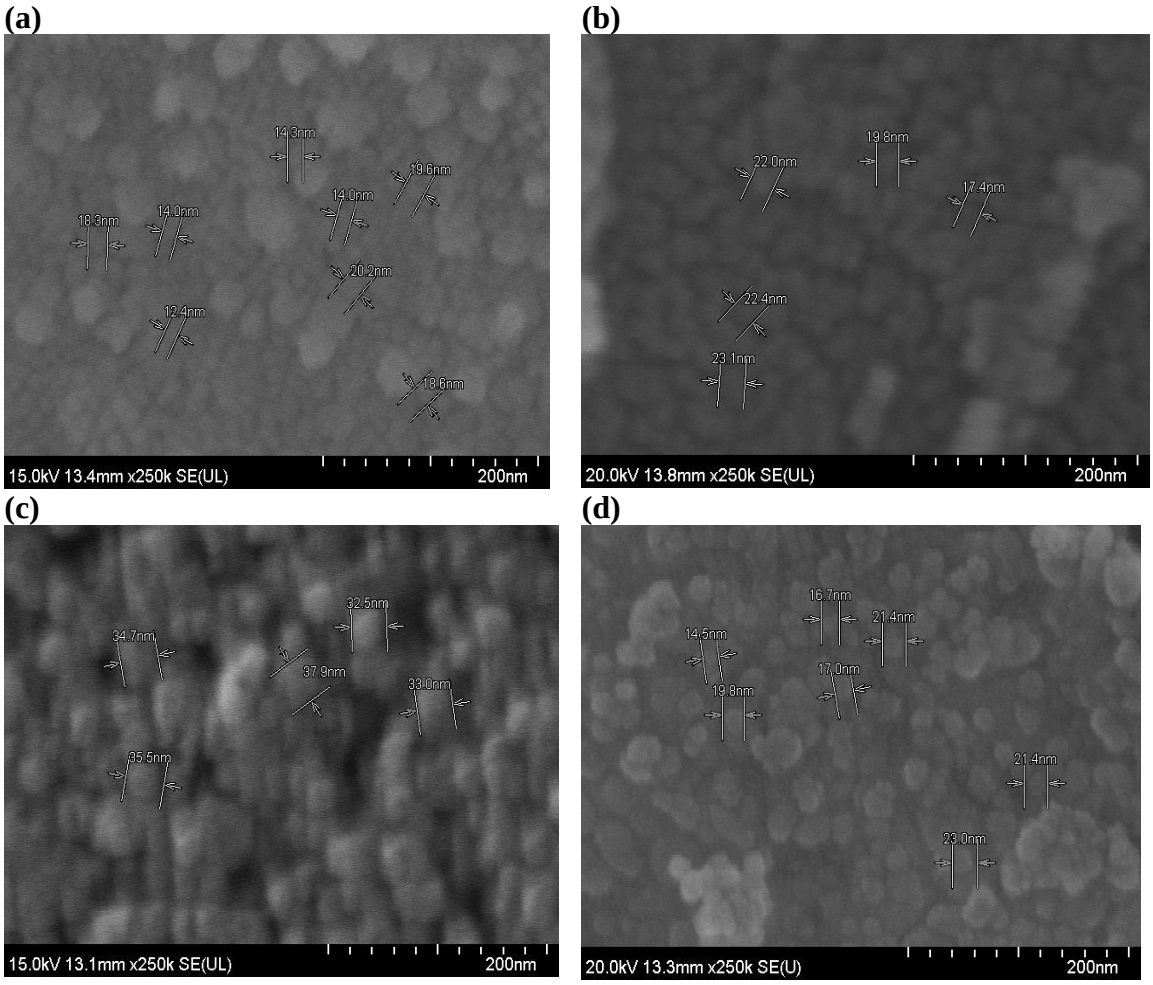

Figure 4.4: Comparison of surface morphology for NiO at reaction times of (a) 6hr, (b) 12hr, (c) 18hr and (d) 24hr with 1.0g of gelatin combining with 0.5mol of nickel acetate as the starting materials

4.2.3. X-ray Diffractogram

Figure 4.5 shows the XRD patterns for the best sample of NiO from the FESEM images. According to FESEM images, sample synthesized with 0.5 mol of nickel acetate with 1 g of gelatin and 1.0 mol, 2 g of gelatin showed the best result in terms of agglomeration and particle size. The NiO diffraction peaks show five distinct peaks that are located at Bragg angles of 37.01º, 43.04º, 62.63º, 75.24º, 79.22º, which correspond to the (1 1 1), (2 0 0), (2 2 0), (3 1 1) and (2 2 2) crystal planes. These Miller's indices indicate the synthesized nickel oxide crystal belongs to the busenite structure with face-centered cubic geometry (Maia et al., 2006). No other impurity peaks were observed in the diffractogram, which proves that pure NiO was synthesized successfully after calcination.

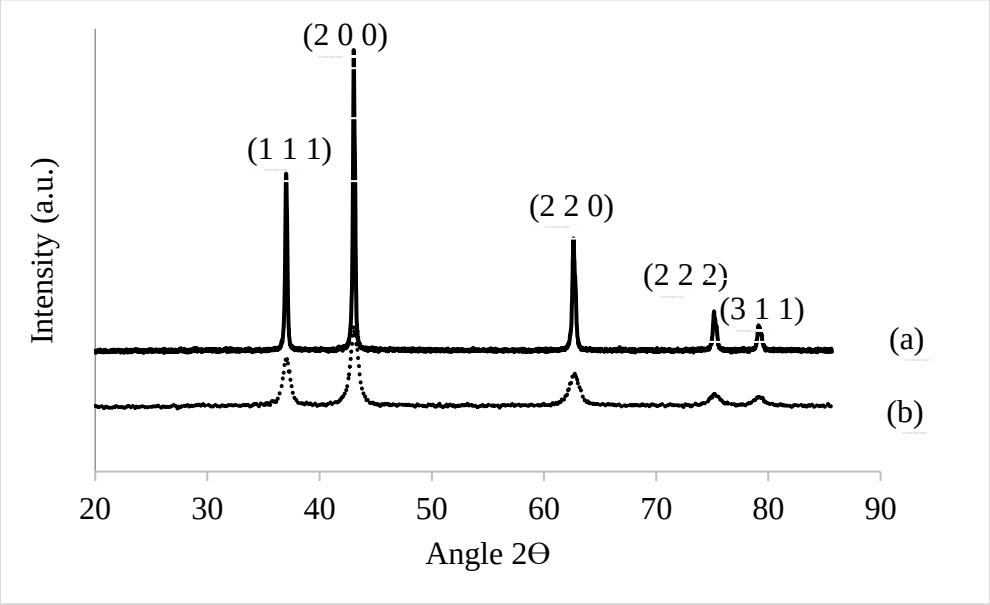

Figure 4.5: Comparison of XRD results for nickel oxide with (a) 1 mol of nickel acetate with 2 g of gel, (b) 0.5 mol of nickel acetate with 1 g of gel

Crystallite size of the synthesized nickel oxide was calculated from the diffraction peak of (2 0 0) using the Scherer equation:

$$L = \frac{k\lambda}{\beta \cos\theta} \quad 4.1$$

where, k (0.9) (Davar et al., 2009) is the Scherer constant, λ is the wavelength of X-ray radiation, β is the full width half minimum of diffraction peak at 2θ and L is the crystallite size.

The estimated sizes were calculated from the line broadening of the second diffraction peak and the results are tabulated in Table 4.1. It can be observe that the average crystallite size reduces as the concentration of both nickel acetate and gelatin decreases. A higher mixing concentration resulted in increased particles size because of the broadening of diffraction peaks at (1 1 1). The increasing crystallite growth is attributed to the quick nucleation process at higher mixing ratio (Al-Sehemi et al., 2014). The results from XRD crystallite size calculation shows consistent results with the FESEM results in Figure 4.2 and Figure 4.3 showing particle size of 45.4 nm, 46.2 nm and particle size of 15.0 nm, 11.7 nm were measured from the images respectively.

Table 4.1 Summary of average crystallite size calculated using Scherrer's Equation

Compound mixing ratio	**Angle (rad)**	**Full width half maximum (rad)**	**Average crystalline size (nm)**
1 mol nickel acetate + 2g of gel	0.6463	0.0039	43.74
0.5 mol nickel acetate + 1g of gel	0.6477	0.0161	10.67

4.2.4. Fourier Transform Infrared Spectra (FTIR)

FTIR spectroscopy was conducted to understand and examine the functional groups of any organic molecule that are present in a set of samples. FTIR spectra for the precursor and nickel oxide samples for various parameters are presented in Figure 4.6. The presence of Ni particles in the precursor is shown at the peaks of 500–600 cm^{-1} (Silva et al., 2018). A vibration bending peak could be observed at 700-1000 cm^{-1}, which suggest the presence of C-N bonds in amine groups from gelatin (Roy et al., 2017). Another two distinct peaks could be observed at 1394 cm^{-1} and 1584 cm^{-1} which are associated with the C–H bending mode of carbon chains in the precursor and 2340 cm^{-1} corresponds to the bending vibration of water molecules (Deng et al., 2018). The weak vibration from 2896-3669 cm^{-1} relates to the O – H stretching bands from physically absorbed water (El-Kemary et al., 2013). The presence of O – H, N – H, C – H and Ni functional groups shows that gelatin and nickel acetate were successfully polymerize during the reaction. From Figure 4.6 (b) to Figure 4.6 (c), it could be observed that only one main peak is detected within the range of 500 – 650 cm^{-1}. This peak is considerably weaker as compared to the precursor spectra from Figure 4.6 (a). This occurrence is due to the reduction of Ni bonds into Ni – O. No other peaks were observed from 650 cm^{-1} onwards indicating the absence of O – H, N – H, C – H functional groups. In other words, these functional groups were successfully removed during calcination and nickel oxide was remained as the end product. The findings from FTIR are in great agreement with the results of XRD, showing pure NiO formation.

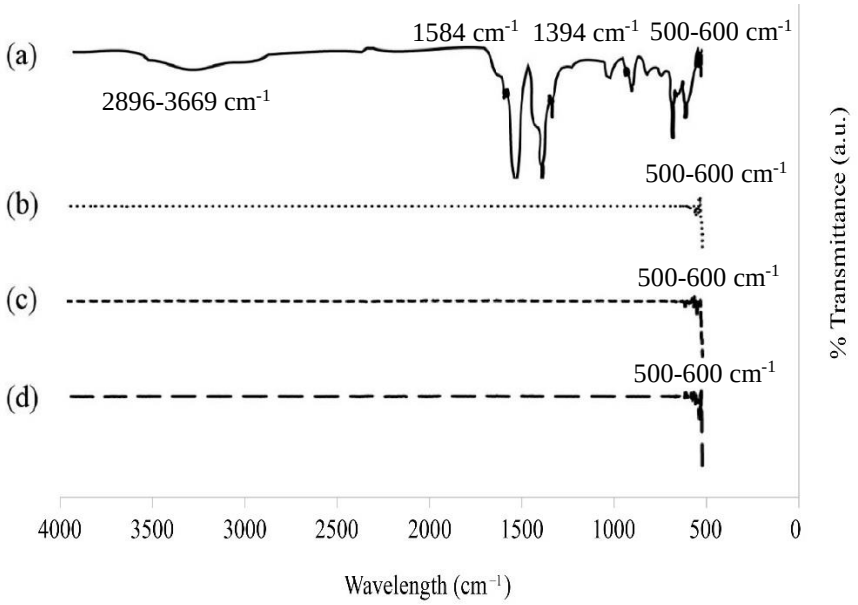

Figure 4.6: FTIR spectra of precursor and nickel oxide nanoparticles synthesize at (a) precursor, (b) 1.0 mol of nickel acetate and 2.0 g of gelatin (c) 0.5 mol of nickel acetate and 1.0 g of gelatin, (d) reaction time of 6 h

4.2.5. Raman Spectroscopy

Raman spectroscopy (RS) was conducted to study the surface properties of NiO and structural transition. RS was conducted for each parameter of sol reaction in order to determine the optimize condition to synthesize nano-sized nickel oxide. The room temperature Raman spectra of NiO consists of two main bands within the range of 200 cm^{-1} – 1800 cm^{-1}. Two vibrational bands: longitudinal optical (LO) at ~510 cm^{-1} and 2LO at 1100 cm^{-1} can be observed from all the reaction parameters as seen in Figure 4.7 (Thamri et al., 2017). The first order LO band at 510 cm^{-1} correspond to the Ni-O stretching mode due to the photon excitement of nano-sized NiO. It is also observed from Figure 4.7 (c) that irregular bumps are present between the LO and 2LO band. This could indicate the presence of O-H bonds that are still present in the sample. This

indicates that 0.5 mol of nickel acetate is inadequate to completely hydrolyse with 2.0 g of gelatin, which suggest nickel oxide precursor didn't react completely in the initial stages. Furthermore, looking at Figure 4.7 (d), a band at 1600 cm^{-1} can be observed in the NiO sample. This is attributed to the two magnon band (2M) that suggest a larger particle size as compared to the other samples (Kumar et al., 2015). This is in accordance with the FESEM results, wher e images of 1.0 mol of Nickel Acetate and 2.0 g of gelatin show higher agglomeration and particle size.

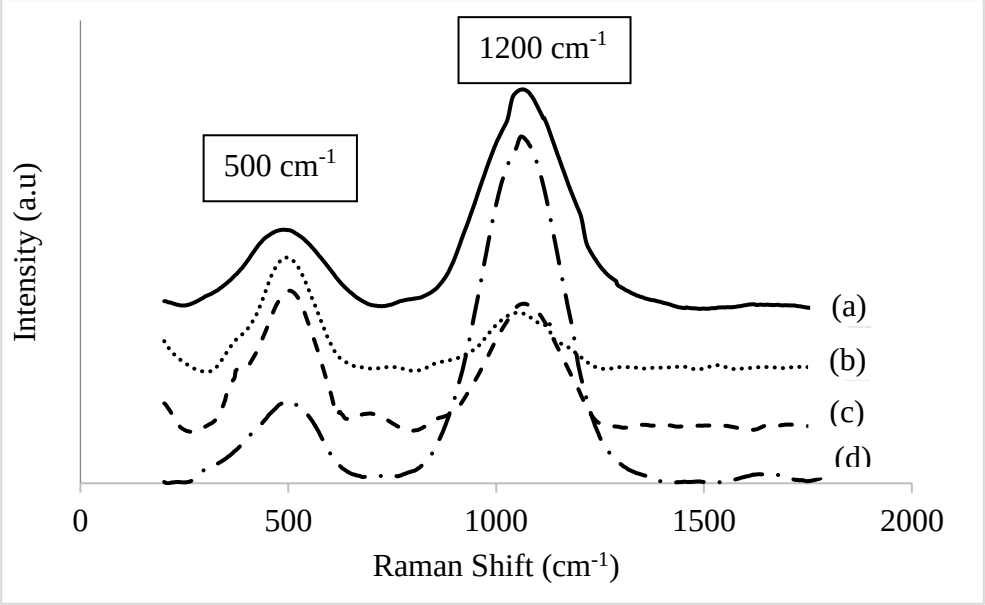

Figure 4.7: Raman Spectra for Nickel Oxide synthesized with (a) Reaction time of 6 hours, (b) 0.5 mol of Nickel Acetate with 1.0 g of Gel, (c) 0.5 mol of Nickel Acetate with 2.0 g of gel and (d) 1.0 mol of Nickel Acetate with 2.0 g of gel

4.3. Calcination of Precursor

A study on calcination parameters for the precursor was conducted because calcination conditions directly affect the chemical and physical properties of the NiO nanoparticles. The Nickel-gelatin xerogel requires calcination to burn off the excess

water and organic components in the compound to form NiO. Different calcination time and temperature will result in different properties due to sintering effect (Varunkumar et al., 2017b). A high temperature and long duration of calcination time usually results in larger particles because of the heighten kinetic energy in the particles that forms agglomeration. Hence, this section discusses on the parameters of calcination time and temperature on the resulting NiO nanoparticles.

4.3.1. Microstructural Analysis

FESEM images of calcination time and temperature were attained to evaluate and conclude the optimum calcination parameter for NiO nanoparticles.

4.3.1.1 Calcination Time

The effect of calcination time on surface morphology of NiO nanoparticles was also studied. Calcination times of ranging between 2 h to 8 h at constant calcination temperature of 500 ºC with ramping rate of 2 ºC/min were investigated. All of the FESEM images presented in Figure 4.8 (a) to Figure 4.8 (d), show that nanosphere particles were successfully obtained. However, irregular shaped particles and large agglomeration were observed at Figure 4.8 (a). This could be attributed to the insufficient time allowed for high homogeneity calcination reaction. Comparing calcination time at Figure 4.8 (b) to Figure 4.8 (d), also show that calcination times of 4 h demonstrates a better particles sizes as compared to 6 h and 8 h. Hence, calcination time of 4 h was found to be the most favourable with particle size ranging between 13.4 nm to 22.4 nm.

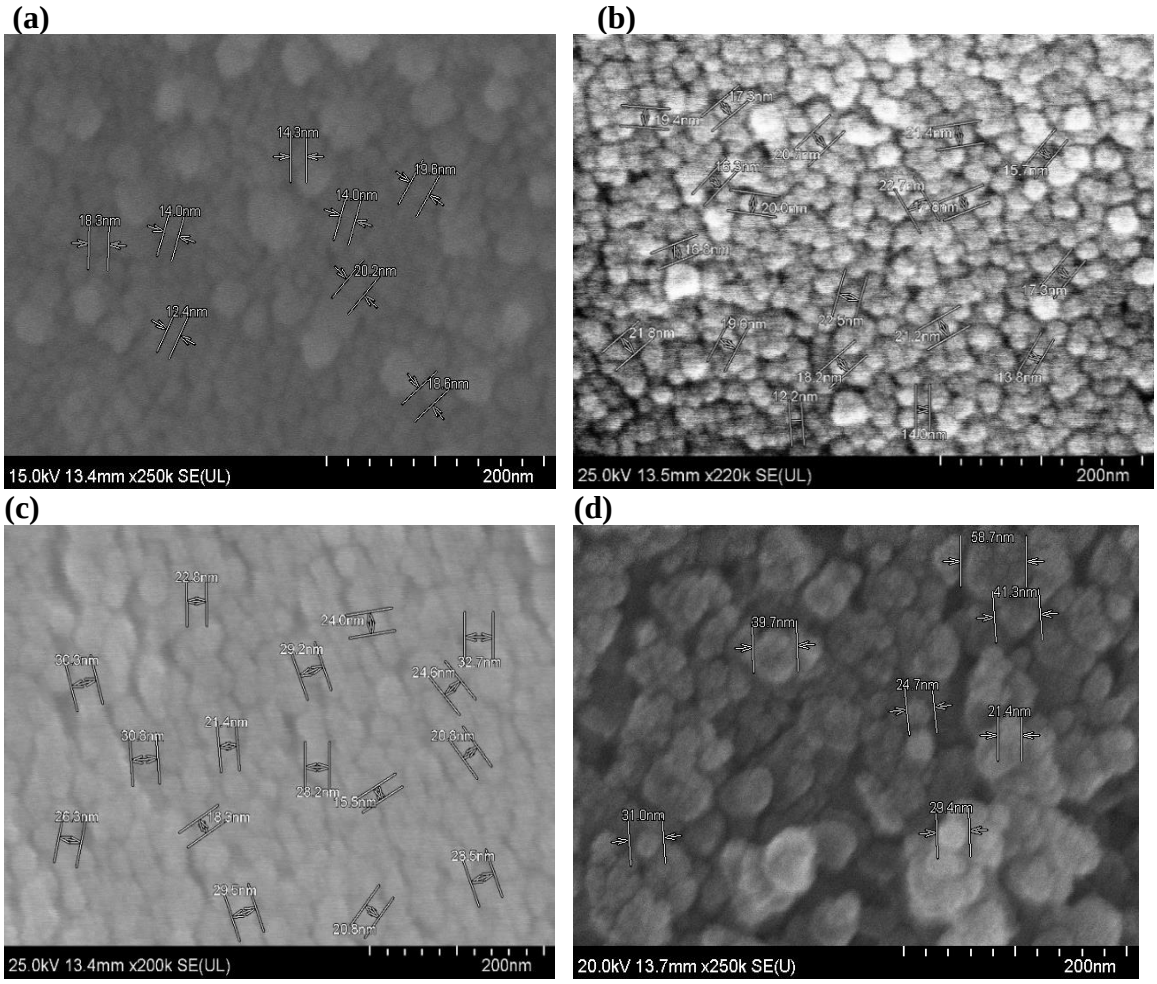

Figure 4.8: Comparison of surface morphology for NiO at calcination times of (a) 2 h, (b) 4 h, (c) 6 h and (d) 8 h with a constant calcination temperature at 500 ^{o}C

4.3.1.2 Calcination Temperature

Figure 4.9 shows the effect of calcination temperature on the surface morphology of NiO synthesized at a calcination time of 6 h with a ramping rate of 2 ^{o}C/min. Figure 4.9 (a) shows irregular shaped particles with high agglomeration indicating that 400 ^{o}C is not sufficient enough for high homogeneity calcination and degradation of the precursor. This is because inadequate calcination temperature leads to incomplete combustion and decomposition of NiO precursor (Prabhakaran et al., 2017). The result

tallies with TGA results in Figure 4.1 whereby the precursor required a temperature of at least 420 ^{o}C for complete degradation to form NiO. Comparing images in Figure 4.9 (b) to Figure 4.9 (d), reveal that higher temperatures will result in larger particle size. This is attributed to higher calcination time resulting in larger particles due to grain growth and agglomeration (Abdel Hameed and Medany, 2017). This occurrence can be attributed to the higher loss of oxygen at higher calcination temperatures that results in an increase repulsion force between neighboring cations (Lay et al., 2012). Results observed from Figure 4.9 (b) shows that calcination temperature of 500 ^{o}C is the optimum calcination temperature to totally combust and degrade the precursor to form nano-sized NiO particles. A previous study on FENi alloy composite synthesized through sol-gel technique studies the effect of calcination temperature. The study shows similar results where the sample synthesized at temperature of greater than 600 ^{o}C shows samples with size ranging from 50 – 300 nm (dos Santos et al., 2016b).

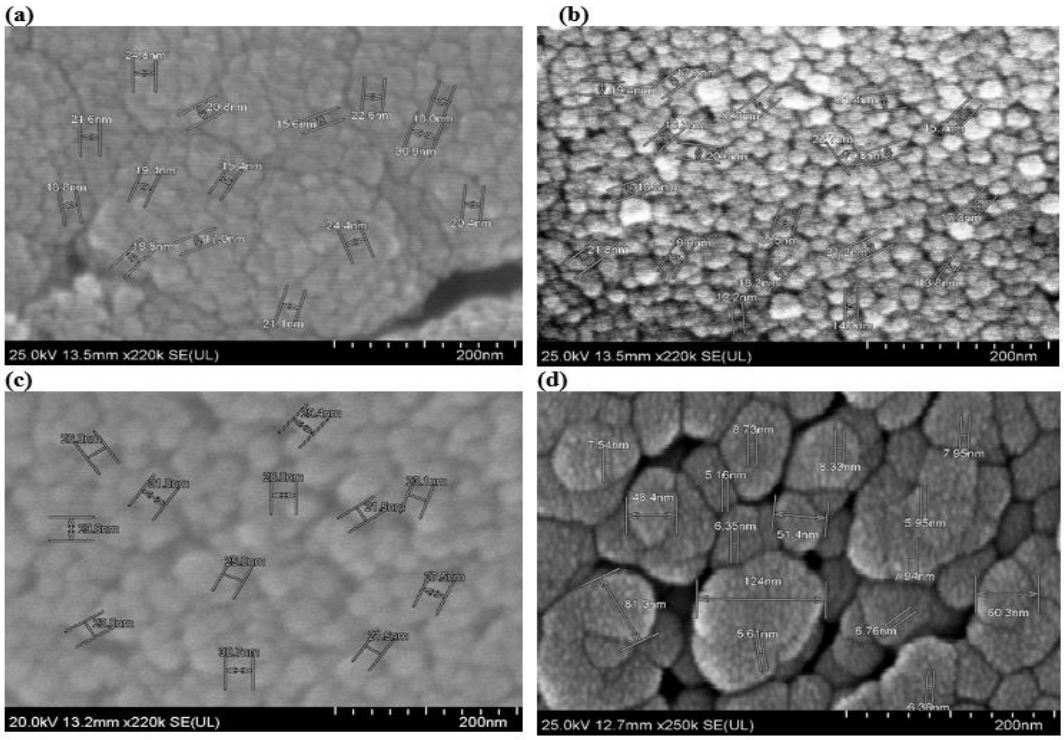

Figure 4.9: Comparison of surface morphology for NiO at calcination temperature of (a) 400 ^{o}C, (b) 500 ^{o}C, (c) 600 ^{o}C and (d) 700 ^{o}C with calcination time at 4 h.

4.3.2. X-ray Diffractogram (XRD)

The phase purity of the synthesized NiO nanoparticles for calcination time and temperature were confirmed by the XRD result shown in Figure 4.10 and Figure 4.11 respectively. The diffraction peaks observed in all the NiO samples produced five diffraction peaks at Bragg angles of 37.01^{o}, 43.04^{o}, 62.63^{o}, 75.24^{o}, 79.22^{o} correspond to (1 1 1), (2 0 0), (2 2 0), (3 1 1) and (2 2 2) crystal planes. The planes is well matched with the busenite cubic structural NiO in the space group Fm3m (Zhang, 2017). All the materials calcined at different time and temperatures shows no additional peaks indicating high purity of NiO nanoparticles without presence of impurities.

4.3.2.1 Calcination Time

Crystalline sizes were calculated using Scherer's equation from Equation 4.1 and the results are tabulated in Table 4.2. A trend can be noted where crystalline size increases with an increase of calcination time. This result is concurrent with the FE-SEM images obtained in Figure 4.8 (a) to Figure 4.8 (d) an increase in particle size is observed with increasing calcination time. Although the smallest crystallite size was calculated at 10.676 nm at calcination time of 2 h, FESEM images from Figure 4.8 (a) shows high amounts of agglomeration and inconsistent size distribution of particles. This indicates that calcination time of 2 h is not sufficient for highly homogenous reaction. Calcination time of 4 h is determined to be the ideal time to proceed because complete nucleation of nanoparticles was already achieved at calcination time of 4 h. Having a longer calcination time will prolong the Ostwald ripening process that merges the smaller particles into a larger nanoparticles (Pinjari et al., 2015). This is in accordance with a previous study where prolonging the calcination time of ZnO shows higher average particles size because of the crystallization growth of ZnO nanoparticles (Lu et al., 2017).

Table 4.2 Summary of average crystallite size for calcination time calculated using Scherrer's Equation

Calcination Time (hr)	Angle (rad)	Full width half maximum (rad)	Average crystalline size (nm)
2	0.6477	0.0161	10.67
4	0.6459	0.0096	17.76
6	0.6492	0.0089	19.24
8	0.6459	0.0078	21.86

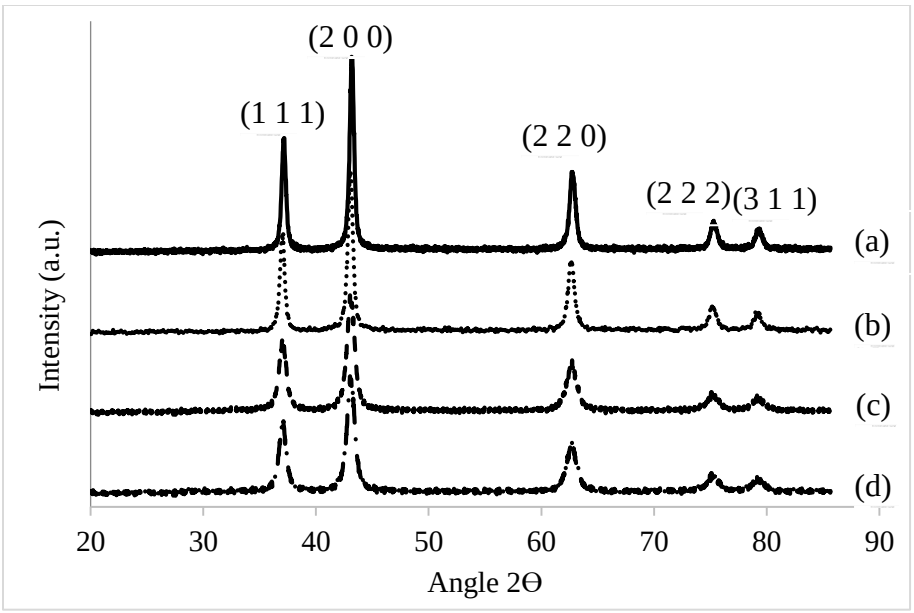

Figure 4.10: Comparison of XRD results for nickel oxide with calcination time of (a) 2 h, (b) 4 h, (c) 6 h and (d) 8 h

4.3.2.2 Calcination Temperature

The estimated crystallite sizes were calculated and presented in Table 4.3. The increase in calcination temperature resulted in a larger average crystallite size. However, calcination temperature at 400 ^{o}C is noted to have a larger particle size compared to 500 ^{o}C and 600 ^{o}C. This could be attributed to the insufficient temperature to decompose off all the organic compounds to form Nickel oxide. Furthermore, the low calcination temperature does not provide enough energy to the crystallite to form a high crystalline structure. The highest crystallite size was found to be 39.99 nm at calcination temperature of 700 ^{o}C as seen in Table 4.3. This occurrence is due to the molecular expansions from grain growth caused by high calcination temperature that results an increased diffusion rate of oxygen to the molecule. A previous research highlighted that

XRD pattern from calcination temperature of 350 ^{o}C to 650 ^{o}C shows that calcination temperature at 550 ^{o}C has the highest degree of crystallinity. At a higher temperature of 550 ^{o}C, the sample expands with higher strain values that reduces the crystallinity of the sample (Turgut et al., 2015). Calcination temperature of 500 ^{o}C for 4 h was found to be more feasible to synthesize the nickel oxide nanoparticles as all the functional groups in the precursor were decomposed with crystallite size of 18.78 nm. Similar results can be noted from a reported study, where crystallite size of NiO progressively increases at higher calcination temperature (600 ^{o}C) because of the crystal growth of the samples (Danial et al., 2015).

Table 4.3 Summary of average crystallite size for calcination temperature calculated using Scherrer's Equation

Calcination Temperature (^{o}C)	**Angle (rad)**	**Full width half maximum (rad)**	**Average crystalline size (nm)**
400	0.6471	0.0078	21.82
500	0.6459	0.0091	18.78
600	0.6467	0.0078	21.82
700	0.6463	0.0042	39.99

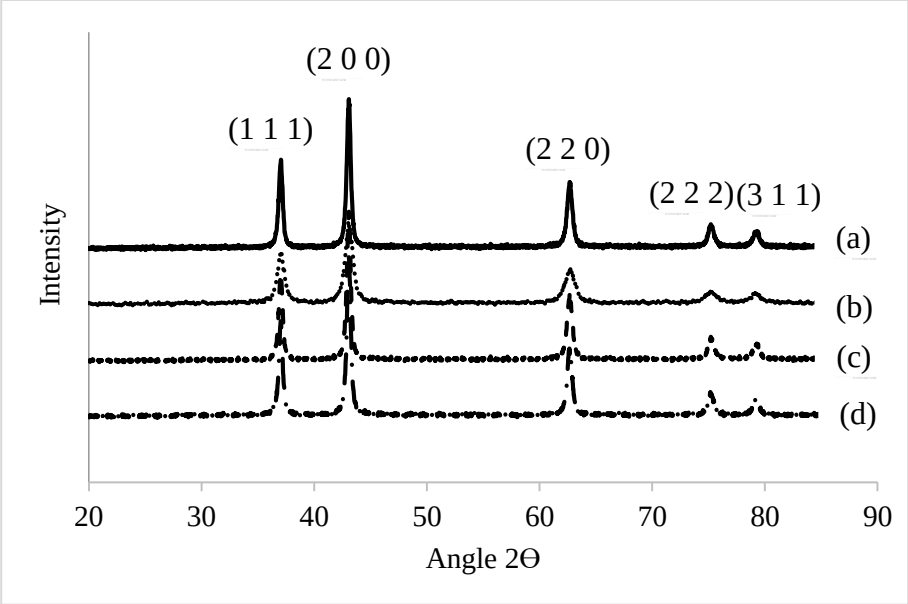

Figure 4.11: Comparison of XRD results for nickel oxide with calcination temperature of (a) 400 ºC, (b) 500 ºC, (c) 600 ºC and (d) 700 ºC

4.3.3. Fourier Transform Infrared Spectra (FTIR)

Figure 4.12 and Figure 4.13 show the FTIR spectra for calcination time and calcination temperature, respectively. It is observed that only one main peak were observed within the range of 500 – 650 cm^{-1}. The peak can be attributed to the dominant functional group of the nickel oxide products, which correspond to the vibration of Ni-O bond. Comparing these results to the precursor FTIR [illegible]5 (a), no other peaks were observed from 650cm^{-1} onwards indicating the absence of O – H, N – H, C – H functional groups. In other words, these functional groups were successfully removed during calcination and nickel oxide was remained as the side end product. This results are in agreement with the data obtained from XRD and RAMAN where no other impurities peak were observed after calcination.

NiO peaks at 500 cm^{-1} to 650 cm^{-1}

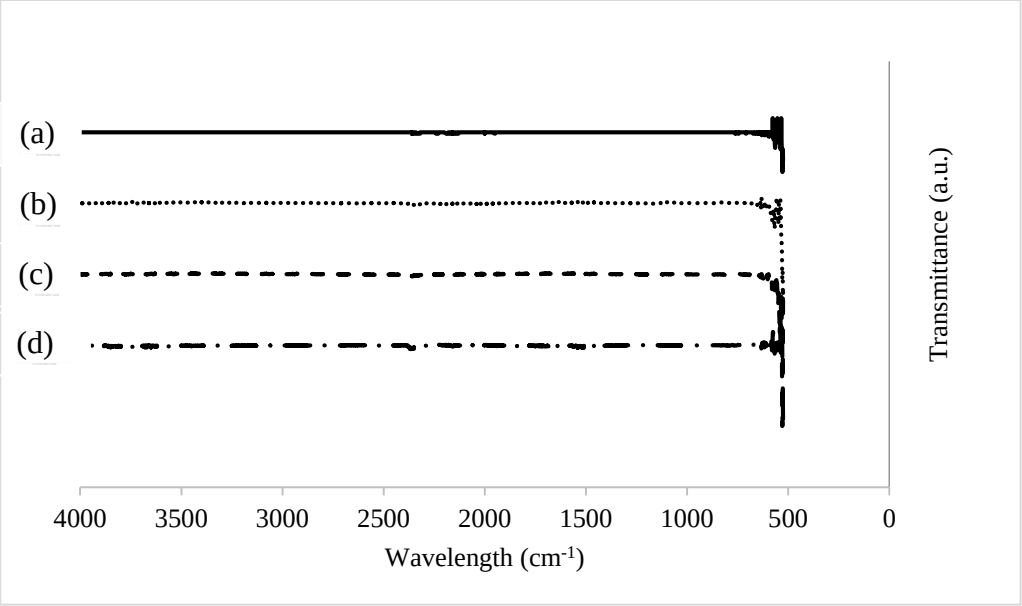

Figure 4.12: Comparison of FTIR spectra for NiO samples with calcination time of (a) 2 h, (b) 4 h, (c) 6 h and (d) 8 h

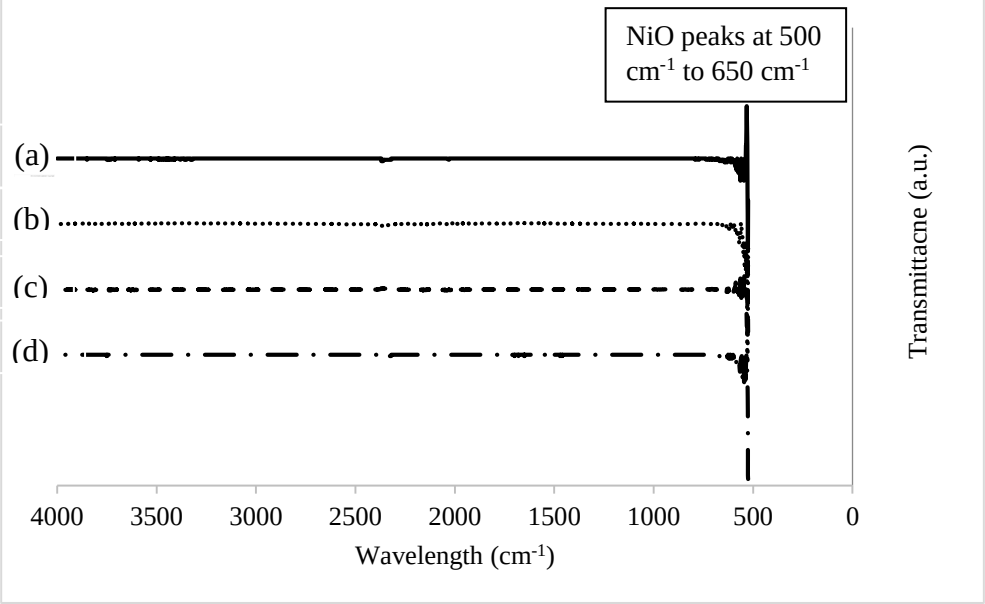

Figure 4.13: Comparison of FTIR spectra for NiO samples with calcination temperature of (a) 400 °C, (b) 500 °C, (c) 600 °C and (d) 700 °C

4.3.4. RAMAN Spectroscopy

Raman spectroscopy was used to study the structural surface properties of NiO at different calcination time and temperature and the results are shown in Figure 4.14 (a)

and Figure 4.14 (b). There are two characteristics peaks that can be observed at 500 cm^{-1} and 1200 cm^{-1}. As explained earlier, the two peaks could attribute to the first order and second order longitudinal (LO) phonon modes of NiO, respectively. The photon excitement of the Ni-O bond results in these two distinct peaks. No irregular stretches were observed in both Figures suggesting that all the O-H bonds are being disintegrated after calcination. Furthermore, 2M band at 1600 cm^{-1} is noticeably absent in Figure 4.14 (a), which shows that small NiO crystallite size was obtained after calcination. However, from Figure 4.14 (b), 2M band can still be observed at calcination temperatures of 400 ^{o}C and 600 ^{o}C. This can be attributed to the large agglomeration of the sample particle, which was also observed in the FESEM images in Figure 4.9. No gelatin peaks were detected in the NiO samples, showing that the entire gelatin was completely removed during calcination, which confirms the results obtained from XRD and FTIR results.

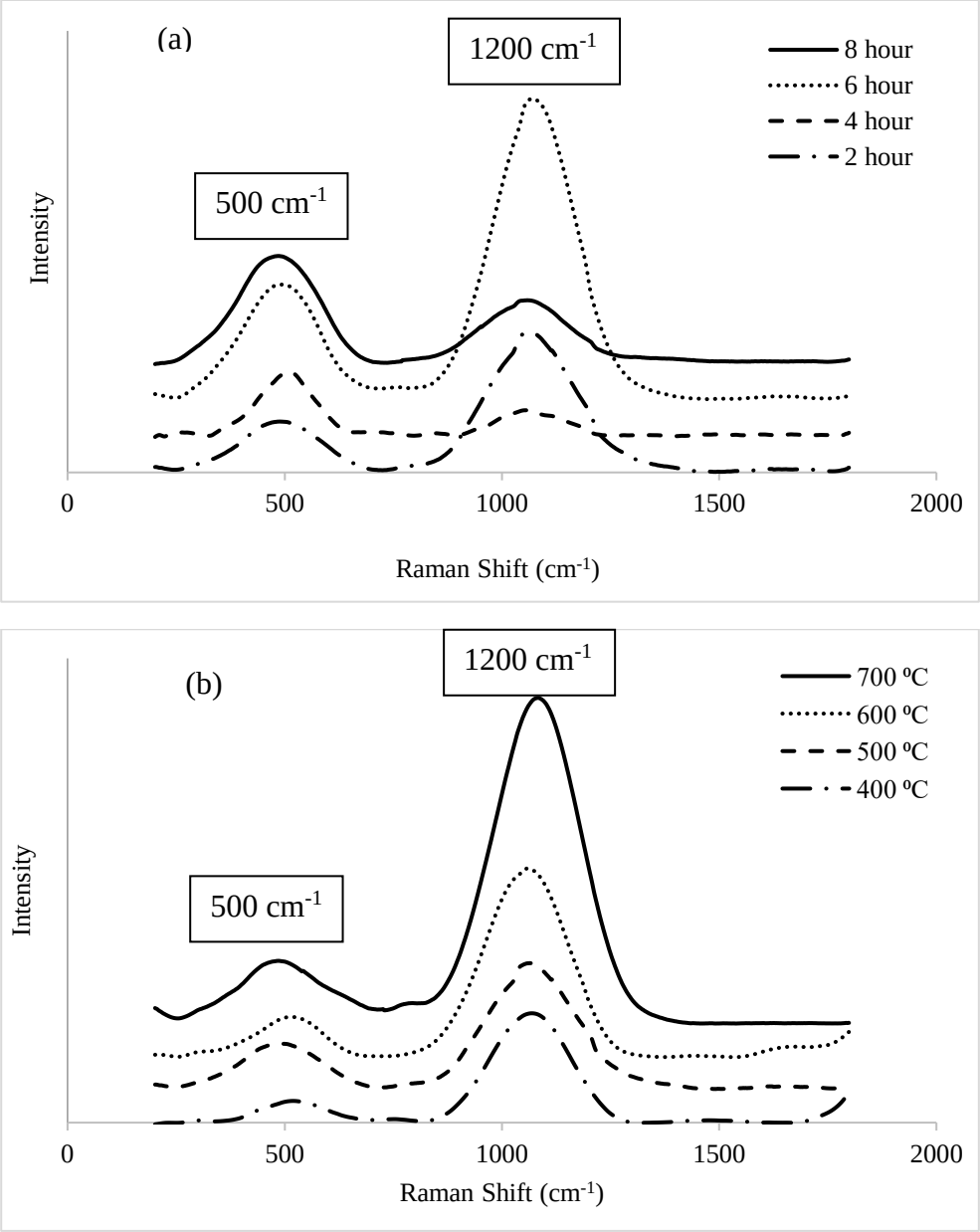

Figure 4.14: (a) RAMAN results for nickel oxide with various calcination times and (b) RAMAN results for nickel oxide with various calcination temperatures

4.3.5. Summary

Manipulation of parameters like, concentration of Nickel Acetate, mass of gelatin, reaction time, calcination time and calcination temperature, has shown significant changes in the morphology, particle size and crystallite size of the NiO. Selection of a

condition was based on the best results in terms of purity, low agglomeration of the sample, good particle size distribution and optimal crystallite size. It was observed that 0.5 mol of concentration of nickel acetate with 1.0 g mass of gelatin at a reaction time and temperature of 6 h and 80 ^{o}C, respectively yielded the optimum result for the sol parameter. Optimum calcination time and temperature were determined at 4 h and 500 ^{o}C, respectively. Photocatalysis on degradation of Reactive Black 5 dye and Acid Yellow 25 dye were conducted using the optimum sample conditions for the catalyst loading parameter in order to further evaluate the catalytic performance of NiO nanopowder.

4.4. Photocatalytic treatment of dye water

Photo-degradation performance does not depend solely on the properties of catalyst and light source. Chemical structure, molecular weight, substitute groups of a dye are crucial factors that determine the photo-degradation efficiency (Khataee et al., 2009). Therefore, the optimized parameters of NiO nanoparticles were employed as the photocatalyst for two different dyes, i.e. Reactive Black 5 dye (RB5) and Acid Yellow 25 (AY25) dye. RB5 and AY25 were chosen for comparison because they contain the same fucntional group (C, N, H, O and S) in the compound but with different molecular structure.

Three parameters were investigated for the photo-degradation of azo dyes. Catalyst load of NiO nanoparticles was investigated first to determine the optimum mass of catalyst. Subsequently, effect of calcination time and calcination temperature of NiO nanoparticles on degradation of dyes were conducted with the best result from catalyst

loading experiment. Effects of calcination time and calcination temperature were examined to further support the conclusion on the synthesis paramters for NiO nanocatalyst. The degradation rate and kinetics of RB5 and AY25 dyes were examined for each of the parameter mentioned. All the photo-degradation experiments were conducted under UV-light at room temperature.

4.4.1. Effects Catalyst Loading on Degradation Rate

Catalyst loading is the most important parameter for photocatalytic degradation because it directly affect the economical areas for an industry. Optimum amounts of catalyst for catalytic efficiency is necessary in order to avoid excess usage of catalyst, which might distress the photocatalytic system (Kavitha and Palanisamy, 2011).

The effect of catalyst loading on the removal of RB5 dye and AY 25 are shown in Figure 4.15 (a) and Figure 4.15 (b) respectively. It was observed that the degradation rate and percentage removal of dye increases with the presence of catalyst until a certain threshold. A photocatalytic system without any catalyst has zero active sites to affect the rate of reaction. This occurrence proves the presence of catalyst increases the oxidation reaction for both the adsorption of reactive black dye and acid yellow dye.

An increase of catalyst loading from 0.1 g to 0.75 g of NiO catalyst shows an increase of photo-degradation rate in RB5 dye as observed from the steeper gradient from Figure 4.15a.

Consequently, it was also observed that RB5 dye removal significantly reduce with an increase of catalyst loading from 0.75 g to 1.0 g in Figure 4.15 (a). Observing Figure 4.15 (b), the degradation efficiency are also noticeably higher with an increase of catalyst loading from 0.1 g to 0.5 g for AY25 dye. Generally, an increase amount of catalyst increases the number of active sites present on the catalyst, which result in a higher number of hydroxyl, OH- and superoxide radicals, $O_2^{-}\cdot$ (Ajmal et al., 2016). Rate of reaction of the dye on the NiO catalyst is limited with a low catalyst load. The reaction rate increases with a higher loading of catalyst due to the increase of active sites on the surface of the catalyst (Mahmoud et al., 2015). Furthermore, a decrease in rate of reaction with an increase of catalyst loading from 0.5 g to 1.0 g can be observed in AY 25 dye from Figure 4.15 (b). Although a higher loading of catalyst provides a higher number of active sites, the rate of reaction decreases due to shielding effect (Linda et al., 2016).

(a)

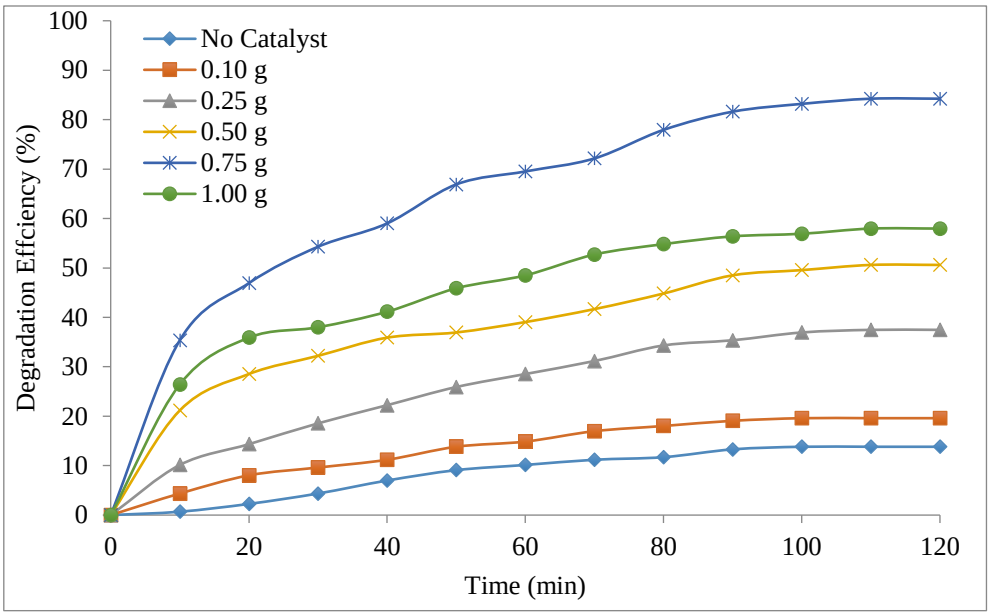

(b)

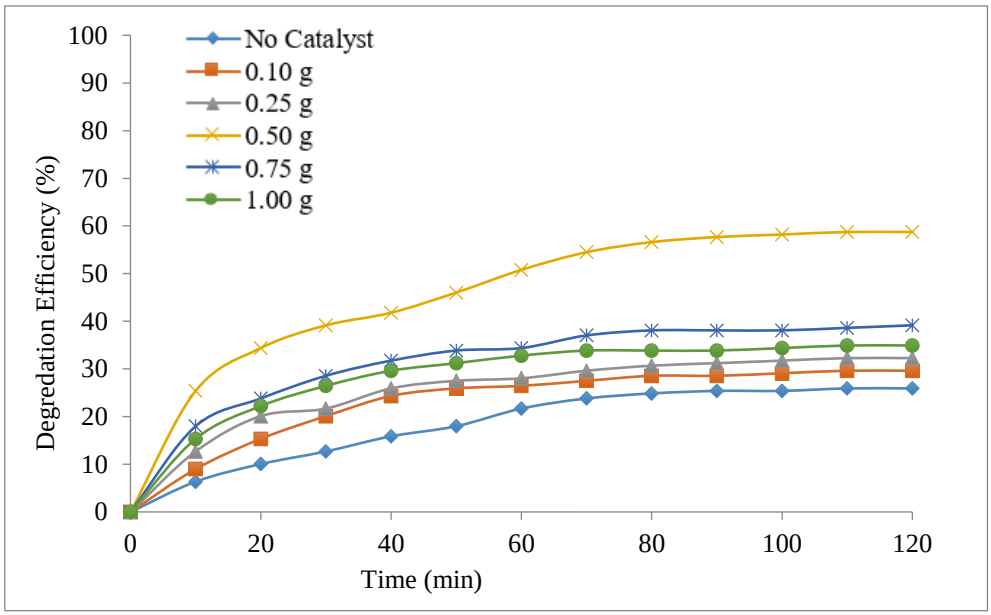

Figure 4.15: Photo-degradation of (a) Reactive Black 5 dye (b) Acid Yellow 25 dye using NiO synthesized through Proteic sol-gel technique at varying catalyst loading from 0.0 g to 1.0 g

Catalyst load of 1.0 g presents a higher number of active sites but the penetration of radiation from the UV-light decreases. High amounts of catalyst commonly forms

agglomerated particles that have small active sites for catalytic activity to occur (Akpan and Hameed, 2009). Agglomerated particles will prevents certain parts of the catalyst surface to be available for photon absorption. The higher loading also will increase the opacity of the dye which disrupts the passage of irradiation throughout the dye. The reduced illumination results in a decrease amount of hydroxyl radical in the photocatalytic system, which will reduce the degradation rate accordingly. The results obtained are in accordance with a study on photo-degradation of Methylene Blue dye with ZnO. It was reported that an increase of catalyst loading does not increase the rate of degradation because of the interference of the passing UV light to the suspension (Chakrabarti and Dutta, 2004). Similarly, a research on the photo-degradation of methyl orange solution with concentration of 0.5 g/l to 6.0 g/l of platinum catalyst shows that the rate of reaction significantly reduce with an increased in catalyst concentration from 3.0 g/l (Huang et al., 2008).

4.4.2. Effect of Calcination Time and Temperature on Degradation Rate

Size, shape and morphology of a catalyst plays an important role in the performance of photo-degradation (Yu et al., 2007). Calcination time and temperature plays a direct role in the formation of different morphology and particle size distribution of the catalyst. The rate of reaction for both reactive black and acid yellow 25 dye was found to be decreasing with an increase of calcination temperature from 500 ^{o}C to 700 ^{o}C observed in Figure 4.16 (a) and Figure 4.16 (b), respectively. This could be attributed to the high crystallinity and smaller surface particle size of the NiO catalyst synthesized at 500 ^{o}C, which results in a decrease in surface defects. FESEM images and XRD analysis from Figure 4.9 and Figure 4.11, correspondingly, support this statement where

the low agglomeration with good particle size distribution was observed at a calcination temperature of 500 ^{o}C. Generally, a highly agglomerated particle will result in lower amounts of active sites. FESEM images from Figure 4.9 shows that although particle size of ± 5.14 nm was obtained with a calcination temperature of 700 ^{o}C, highest amount of agglomeration was observed where the small nano-sized particles are agglomerated to a large particle of ± 124 nm.

The highly agglomerated particles present results with a lowest photo-degradation rate of reaction as compared to NiO calcinated at 500 ^{o}C and 600 ^{o}C. This is in accordance with a study conducted on the photo-degradation of Rhodamine-B using SnO_2/TiO_2 composite film with varying calcination temperature of 100 ^{o}C to 600 ^{o}C where optimum calcination temperature for the degradation of Rhodamine-B dye was obtained at 400 ^{o}C due to the least amount of observed agglomeration from FESEM images taken (Zhou et al., 2008). Another study was conducted for Fe_2O_3/TiO_2 nanocomposite catalyst at different calcination temperature ranging from 300 ^{o}C to 900 ^{o}C. BET analysis of the sample showed that highest specific surface area was obtained at the lowest possible calcination temperature at 300 ^{o}C, hence, the best photo-degradation efficiency was observed with a calcination temperature at 300 ^{o}C showing that a high specific area is ideal to increase the rate of photo-degradation (Nasirian et al., 2017).

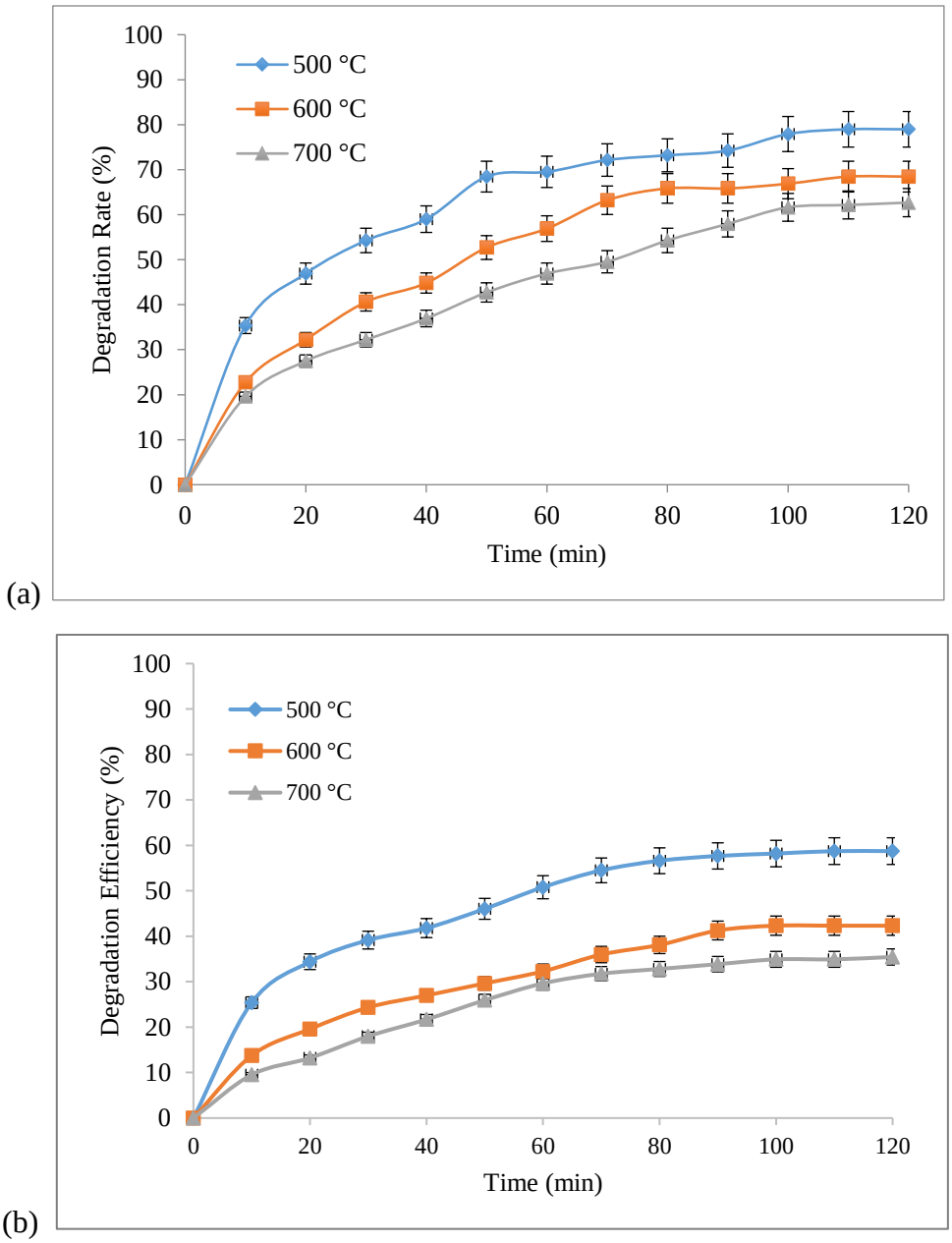

Figure 4.16: Photo-degradation of (a) Reactive Black 5 dye and (b) Acid Yellow 25 dye using NiO synthesized through proteic sol-gel technique at varying calcination temperature at 500 ºC, 600 ºC and 700 ºC with a constant calcination time of 4 h

For the parameter of calcination time, the efficiency of NiO in the photodegradation of RB5 and AY25 dyes increased as the calcination time increased

from 2 h to 4 h but dropped when the calcination time was increased from 4 h to 6 h as seen in Figure 4.17. Calcination time of 4 h was observed to be the optimum parameter due to the stronger Ni-O bonds as observed from FTIR results in Figure 4.13, which resulted in more cavities available for the conversion of hydroxyl ions to form hydroxyl radicals (Sun et al., 2006). A study was conducted to investigate the effects of calcination time of Zn-TiO_2 on the discoloration of Orange II under light radiation, where the results shows that a short calcination time of 3 h was not sufficient enough to optimize the photocatalytic activity of the catalyst.

Similar to the effects of calcination temperature, the increasing duration of calcination caused the efficiency of NiO in the photodegradation to increase. This further confirmed that higher amounts of agglomeration caused by elevated calcination temperature will reduce the efficiency by hindering the active sites available for degradation to occur (Wan et al., 2014). Similarly, RB5 shows better degradation rates in all the calcination temperature and time parameters as compared to AY25. This is because the degradation rate of the dyes also depend upon the adsorption capability on the catalyst surface (Wiszniowski et al., 2002). This can be supported from the results as seen from Table 4.4. The dyes were subjected in presence of NiO catalyst without any irradiation from light source. The results shows that RB5 has a higher degradation efficiency as compared to AY25, which proves that RB5 has a better adsorption on the NiO catalyst.

(a)

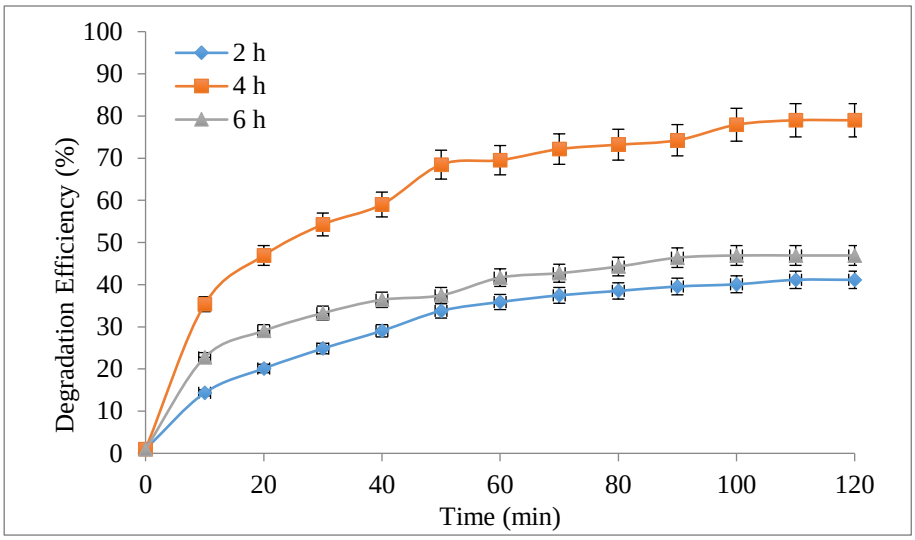

(b)

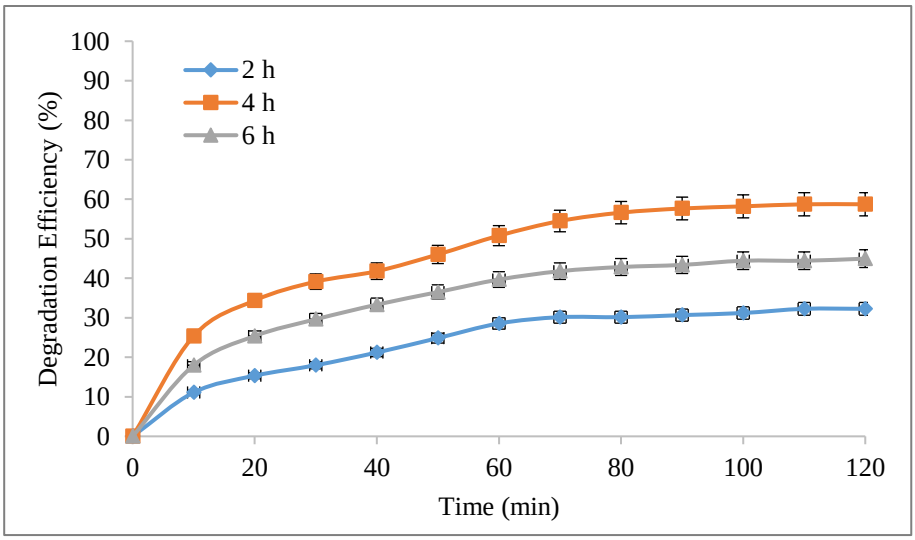

Figure 4.17: Photo-degradation of (a) Reactive Black 5 dye and (b) Acid Yellow 25 dye using NiO synthesized through proteic sol-gel technique at varying calcination time at 2 h, 4 h and 6 h with a constant calcination temperature of 500 ^{o}C

Table 4.4 Adsorption of dyes without presence of light

Type of Dye	**Time (min)**	**Adsorption of dyes (%)**
Reactive Black 5	120	18.42
Acid Yellow 25	120	11.25

This is in accordance with a previous study conducted on the photo-degradation of methylene blue with tin dioxide nanocrystals acting as the catalyst. It was determined that TiO_2 sample with low calcination temperature of $T \leq 200\ ^oC$ exhibited the highest degradation activities whereby high calcination temperature of $400\ ^oC \leq T \leq 1000\ ^oC$ shows a decreasing degradation efficiency, which was attributed to the increasing crystallite size (Wan et al., 2014). Furthermore, the rough surface and crystallinity of the catalyst could be another possible explanation that reduces the efficiency of the dyes with higher calcination temperature and time (Wang et al., 2013).

4.4.3. Kinetics Study

The comparisons of the pseudo first order and second order model between RB5 and AY25 dyes are shown in Figure 4.18 and Figure 4.19, respectively. The best degradation rate for RB5 and AY25 are presented, with 0.75 g and 0.5 g catalyst load, respectively. The kinetic model with a higher correlation R^2 value was selected as the most compatible model for the degradation of RB5 and AY25 dyes with nano-NiO photocatalyst. Looking at Figure 4.198 it can be observed that the pseudo second order model has a higher R^2 value of 0.9689 compared to the pseudo first order model at 0.737 for RB5 dye. Similar results can be seen from Figure 4.19, where pseudo second order has a R^2 value of 0.8514 compared to pseudo first order at 0.6424. This signifies that the pseudo second order is a better fitting model for the photocatalytic degradation of RB5 and AY25. The lower R^2 values from pseudo first order model for both RB5 dye and AY25 dye could be attributed to the proposed model being suitable for modeling

systems with lower dye concentration (Lanfredi et al., 2014). Furthermore, the pseudo first order kinetics is generally found to be suitable for the initial stages of adsorption (Repo et al., 2012). This result is in accordance with a previous study, where the pseudo second order model shows a better fitting compared to the pseudo first order model for degradation of anionic dye with ZnO catalyst. It was suggested that the linearity of the pseudo second order could be attributed to the occurrence of intra-particle diffusion during adsorption process (Hassanzadeh Siahpoosh and Soleimani, 2017).

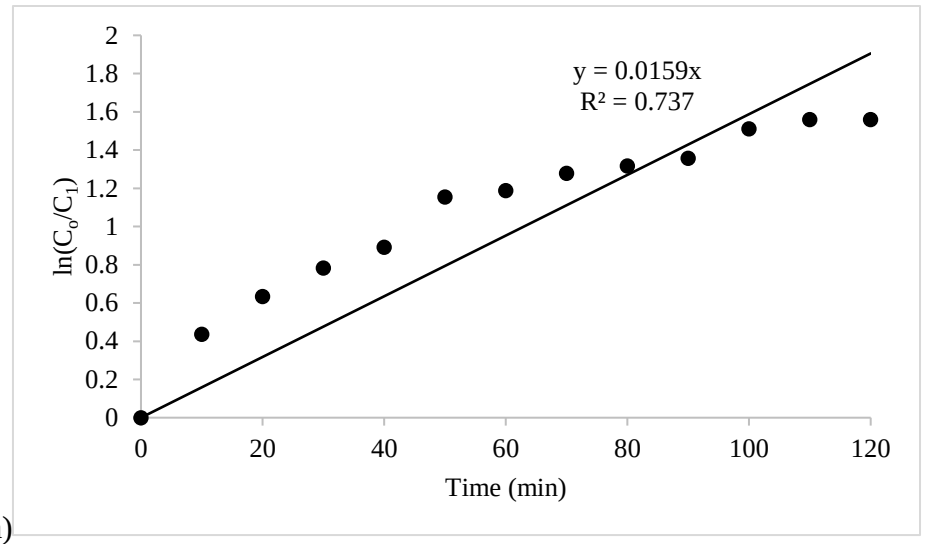

(a)

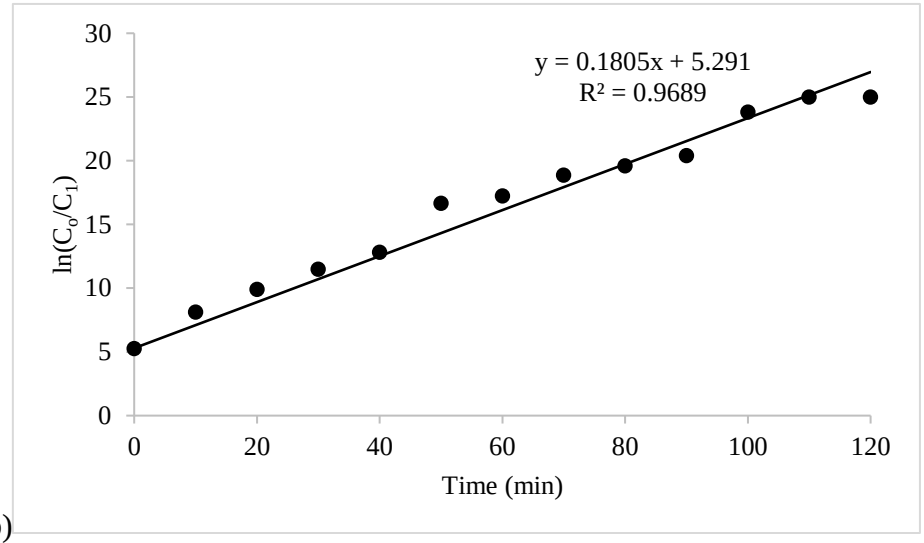

(b)

Figure 4.18: Kinetics analysis of photo-degradation of Reactive Black 5 dye for (a) Pseudo first order and (b) Pseudo second order model using the best photo-degradation results at 0.75 g

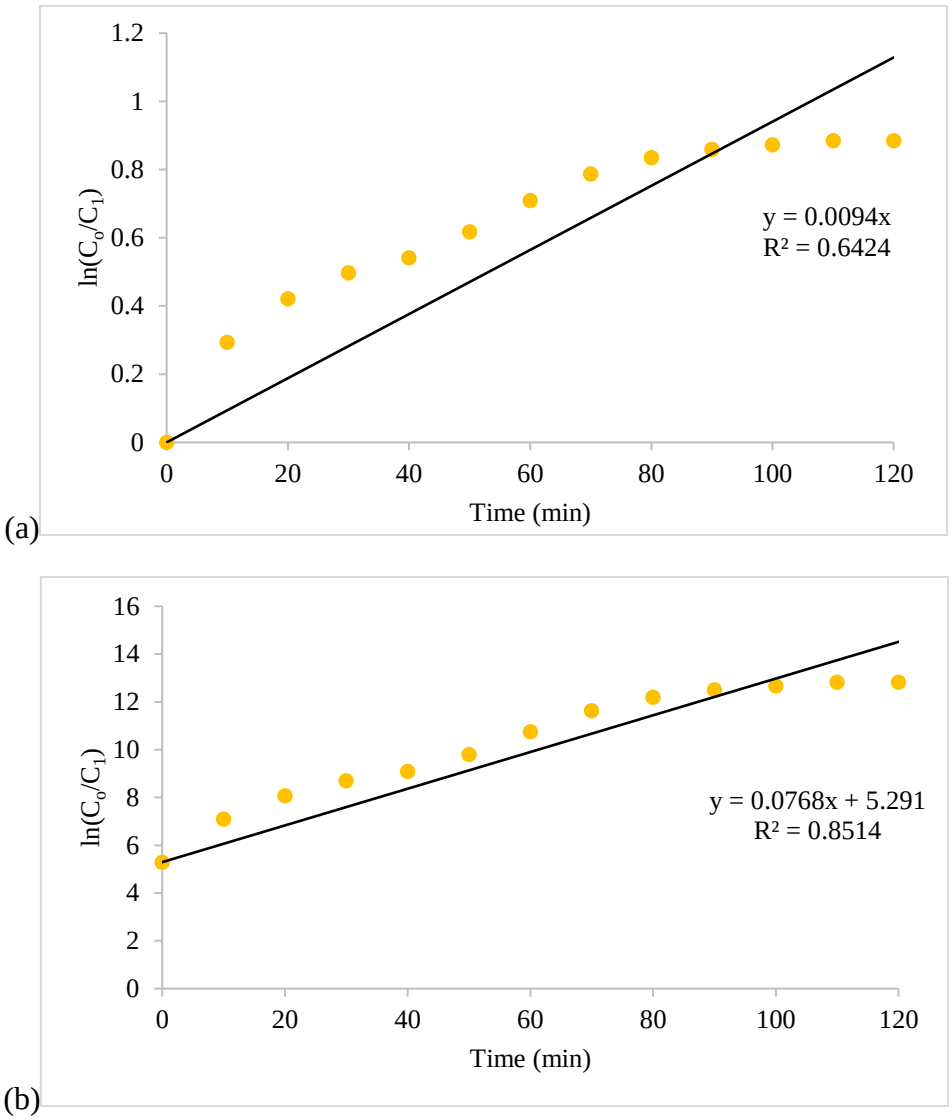

Figure 4.19: Kinetics analysis of photo-degradation of Acid Yellow 25 dye for (a) Pseudo first order and (b) Pseudo second order model using NiO synthesized through proteic sol-gel method at varying catalyst loading.

4.5. Comparison of Photo-degradation Performance

The data obtained from this research shows that nickel oxide nanoparticles synthesize through sol-gel method shows that dye removal of Reactive Black 5 dye has a higher efficiency and degradation rate of 84.23 % and 0.1805 min^{-1} respectively,

whereas the dye removal of Acid Yellow dye only shows an efficiency of 58.73 % and a degradation rate of 0.0768 min^{-1}. This is attributed to the difference in molecular formula and molecular structure of RB5 and AY25 as seen from Table 4.5. During photocatalytic degradation of dyes, the anions group of the dyes will be discharged from the dye molecule. Anions group like sulphate (SO_4^{2-}) and nitrates (NO_3^-) can have a significant effect on the degradation rate because they act as strong oxidizing agents to form hydroxyl radicals (Borthakur et al., 2017). Degradation rate is directly proportional to the number of OH· and O_2^-·(Soo et al., 2016). As mentioned before, the increase amount of superoxides and hydroxyl radicals will enhance the photocatalytic system by increasing the redox reaction to degrade the dye into organic compounds (Ajmal et al., 2016).

Table 4.5 Chemical data for Reactive Black 5 dye and Acid Yellow 25 dye

Name	Molecular formula	Molecular weight	Molecular Structure
Reactive Black 5	$C_{26}H_{21}N_5Na_4O_{19}S_6$	991.82	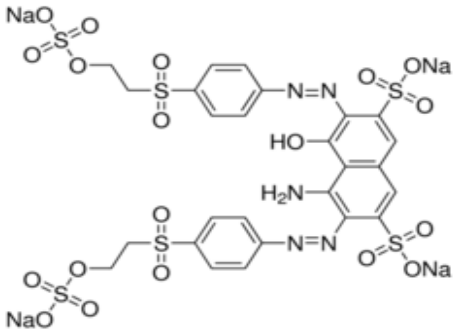
Acid Yellow 25	$C_{23}H_{20}N_5NaO_6S_2$	549.55	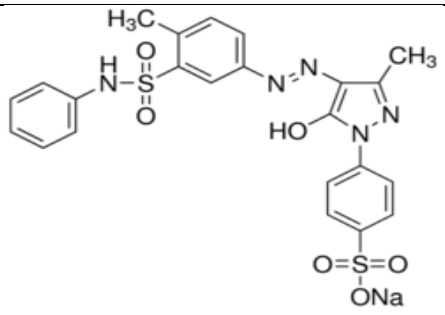

The mechanism of sulphate ions can be presented in the following equation:

$$SO_4^{2-} + h^+ \rightarrow SO_4^- \cdot \quad (4.2)$$

$$SO_4^- \cdot + H_2O \rightarrow SO_4^{2-} + OH \cdot + H^+ \quad (4.3)$$

SO_4^{2-} acts as driving force from the dye molecule bulk interface, increasing the aqueous ionic strength and enhancing the degradation efficiency. At Equation 4.2, the sulphate ion reacts with the positive holes at the valence band to form a sulphate radical anion ($SO_4^{-}\cdot$). The sulphate radical is a strong oxidant anion with redox potential of 2.6 eV further oxidize the water molecule to form hydroxyl radicals (Ajmal et al., 2014). Similarly, nitrate also shows similar mechanism where hydroxyl radicals can be produced through irradiation of nitrates anion. The hydroxyl radical formation is shown in the following equation:

$$NO_3^- + hv\ (light) \rightarrow NO_2^- + O \quad (4.4)$$

$$NO_3^- + H_2O + hv\ (light) \rightarrow NO_2^- + 2OH \cdot \quad (4.5)$$

$$O + H_2O \rightarrow 2OH \cdot \quad (4.6)$$

Looking at the molecular structure of RB5 and AY25 in Table 4.5, RB5 contains more sulphur and oxygen molecules as compared to AY25. The higher amount of sulphate ions discharged during photocatalytic degradation of dyes could result in a higher degradation efficiency. This statement can be supported by a previous study

conducted on investigating the influence of SO_4^{2-} and NO_3^- on photo-degradation of Congo red and Remazol blue dye. Results from the study showed that the addition of SO_4^{2-} and NO_3^- enhances the degradation efficiency as compared to the samples without any added anions (Borthakur et al., 2017). Additionally, a previous study investigated the addition of potassium persulphate into the photocatalytic degradation of acridine orange dye and the results revelaed an increased rate constant value with elevated amount of potassium persulphate (Pare et al., 2008).

4.6. Summary

In summary, NiO nanoparticles were successfully synthesized through sol-gel method with gelatin as the templating agent. The optimum parameters from the synthesis of NiO nanoparticles were utilized to examine the catalytic performance of the nanoparticles on photo-degradation of RB5 and AY 25 dye. A detailed conclusion is presented in Chapter 5.

CHAPTER 5

CONCLUSIONS AND FUTURE RECOMMENDATIONS

5.1 Conclusions

Pure nickel oxide nanoparticles were obtained by proteic sol-gel method with nickel acetate tetrahydrate and gelatin from bovine skin as the initial raw material. The parameters studied in this work included concentration of nickel acetate, mass of gelatin, reaction time, calcination temperature and calcination time. Reaction temperature and ramping rate were set at a constant of 80 ^{o}C and 2 ^{o}C/min, respectively for all the experiments conducted. TGA results on the precursor have showed that a minimum calcination temperature of 420 ^{o}C was required to decompose all the nitrates, carbon, and hydroxides compound into nickel oxide. Morphology from FESEM images further concludes that a high homogeneity of particle size was achieved by calcination temperature of 500 ^{o}C. The mixing ratio of nickel acetate and gelatin has showed great influence onto the surface morphology and crystallite size of the nickel oxide nanoparticles. The crystallite size of nickel oxide was found to increase from 10.67 nm to 43.75 nm through the usage of Scherer's equation. Based on the FE-SEM images, FTIR and RAMAN spectrometry results, it was found that the "sol" reaction of the system only required 6 h to reach reaction equilibrium. FE-SEM images proved that the NiO particles obtained are generally spherical and almost uniform shape, which indicates homogeneity in the samples. FE-SEM images also show a higher degree of agglomeration with the increasing calcination temperature. FTIR analysis results revealed that there were no impurities observed in the nickel oxide nanoparticles at

calcination temperatures above 500 ^{o}C. The decrease in concentration of nickel acetate also showed a better purity of the final product. Only a strong adsorption band existed at 500 cm^{-1} to 600 cm^{-1}, which corresponds to the strong vibration of Ni-O bond in the sample. This result, coupled with the peaks shown in XRD proves that a highly pure NiO were synthesized in this research. Raman spectrometry was also conducted on the nickel oxides nanoparticles and results showed that only nickel oxide peaks were observed, further justifying that only pure metal oxides were obtained.

The best condition for synthesis of nickel oxide nanoparticles through sol-gel method was obtained at 0.5 mol of nickel acetate with 1.0 g of gelatin diluted with 30 ml and 170 ml of distilled water as its starting material with a reaction time of 6 h at temperature of 80 ^{o}C followed by calcination time of 4 h at 500 ^{o}C with a ramping rate of 2 ^{o}C/min. No reaction was observed with concentration of nickel acetate less than 0.5 mol and 6 h was found to be the shortest time required for polymerization and hydrolysis of nickel acetate and gelatin that forms the xerogel for further calcination to obtain nano sized nickel oxide powder. This was confirm by photocatalytic degradation experiment through the degradation of Reactive Black 5 dye and Acid Yellow dye. It was determined that the optimum conditions showed the highest degradation efficiency for Reactive Black 5 dye and Acid Yellow 25 dye at 84.23 % and 58.73 % respectively.

5.2 Future Recommendations

Based on the results and conclusion of the current studies, it is recommended that the following is investigated for future studies:

1) The effects of adding a surfactant in the sol-gel precursor could be investigated to see the effects of different surfactants.
2) The effect of drying conditions could be evaluated on the effects of freeze drying over conventional oven drying.
3) Nano-sized dye effluents from industries could be used to investigate the photocatalytic activities of the synthesized nanoparticles for a more accurate valuation of the NiO.

REFERENCES

ABDEL HAMEED, R. M. & MEDANY, S. S. 2017. NiO nanoparticles on graphene nanosheets at different calcination temperatures as effective electrocatalysts for urea electro-oxidation in alkaline medium. *Journal of Colloid and Interface Science,* 508**,** 291-302.

ABU-ZIED, B. M., BAWAKED, S. M., KOSA, S. A., ALI, T. T., SCHWIEGER, W. & AQLAN, F. M. 2017. Effects of Nd-, Pr-, Tb- and Y-doping on the structural, textural, electrical and N2O decomposition activity of mesoporous NiO nanoparticles. *Applied Surface Science,* 419**,** 399-408.

AGUIAR, J. E., CECILIA, J. A., TAVARES, P. A. S., AZEVEDO, D. C. S., CASTELLÓN, E. R., LUCENA, S. M. P. & SILVA, I. J. 2017. Adsorption study of reactive dyes onto porous clay heterostructures. *Applied Clay Science,* 135**,** 35-44.

AJMAL, A., MAJEED, I., MALIK, R. N., IDRISS, H. & NADEEM, M. A. 2014. Principles and mechanisms of photocatalytic dye degradation on TiO2 based photocatalysts: a comparative overview. *RSC Advances,* 4**,** 37003-37026.

AJMAL, A., MAJEED, I., MALIK, R. N., IQBAL, M., NADEEM, M. A., HUSSAIN, I., YOUSAF, S., ZESHAN, MUSTAFA, G., ZAFAR, M. I. & NADEEM, M. A. 2016. Photocatalytic degradation of textile dyes on Cu2O-CuO/TiO2 anatase powders. *Journal of Environmental Chemical Engineering,* 4**,** 2138-2146.

AKPAN, U. G. & HAMEED, B. H. 2009. Parameters affecting the photocatalytic degradation of dyes using TiO2-based photocatalysts: A review. *Journal of Hazardous Materials,* 170**,** 520-529.

AL-SEHEMI, A. G., AL-SHIHRI, A. S., KALAM, A., DU, G. & AHMAD, T. 2014. Microwave synthesis, optical properties and surface area studies of NiO nanoparticles. *Journal of Molecular Structure,* 1058**,** 56-61.

AMONPATTARATKIT, P., KHUNMANEE, S., KIM, D. H. & PARK, H. 2017. Synthesis and Characterization of Gelatin-Based Crosslinkers for the Fabrication of Superabsorbent Hydrogels. *Materials,* 10**,** 826.

AN, H.-R., PARK, S. Y., HUH, J. Y., KIM, H., LEE, Y.-C., LEE, Y. B., HONG, Y. C. & LEE, H. U. 2017. Nanoporous hydrogenated TiO2 photocatalysts generated by underwater discharge plasma treatment for solar photocatalytic applications. *Applied Catalysis B: Environmental,* 211**,** 126-136.

ARSLAN, O. & ABALı, Y. 2017. Controlled modulation of 1D ZnO nano/micro structures: Evaluation of the various effects on the photocatalytic activity. *Journal of Physics and Chemistry of Solids,* 108**,** 88-97.

ATCHUDAN, R., EDISON, T. N. J. I., PERUMAL, S., SHANMUGAM, M. & LEE, Y. R. 2017. Direct solvothermal synthesis of zinc oxide nanoparticle decorated graphene oxide nanocomposite for efficient photodegradation of azo-dyes. *Journal of Photochemistry and Photobiology A: Chemistry,* 337**,** 100-111.

AYATI, A., SHAHRAK, M. N., TANHAEI, B. & SILLANPÄÄ, M. 2016. Emerging adsorptive removal of azo dye by metal–organic frameworks. *Chemosphere,* 160**,** 30-44.

AZHAGU RAJ, R., ALSALHI, M. S. & DEVANESAN, S. 2017. Microwave-Assisted Synthesis of Nickel Oxide Nanoparticles Using Coriandrum sativum Leaf Extract and Their Structural-Magnetic Catalytic Properties. *Materials,* 10**,** 460.

BABAEI, A. A., KAKAVANDI, B., RAFIEE, M., KALANTARHORMIZI, F., PURKARAM, I., AHMADI, E. & ESMAEILI, S. 2017. Comparative treatment of textile wastewater by adsorption, Fenton, UV-Fenton and US-Fenton using magnetic nanoparticles-functionalized carbon (MNPs@C). *Journal of Industrial and Engineering Chemistry*.

BABU, J. & MURTHY, Z. V. P. 2017. Treatment of textile dyes containing wastewaters with PES/PVA thin film composite nanofiltration membranes. *Separation and Purification Technology,* 183**,** 66-72.

BANKOVIĆ–ILIĆ, I. B., MILADINOVIĆ, M. R., STAMENKOVIĆ, O. S. & VELJKOVIĆ, V. B. 2017. Application of nano CaO–based catalysts in biodiesel synthesis. *Renewable and Sustainable Energy Reviews,* 72**,** 746-760.

BARBUSINSKI, K. & MAJEWSKI, J. 2003. *Discoloration of Azo Dye Acid Red 18 by Fenton Reagent in the Presence of Iron Powder*.

BHASKAR, A., LAI, R.-T., CHANG, K.-C. & LIU, C.-J. 2017. High thermoelectric performance of BiCuSeO prepared by solid state reaction and sol-gel process. *Scripta Materialia,* 134**,** 100-104.

BHATE, P. M., DEVI, R. V., DUGANE, R., HANDE, P. R., SHAIKH, L., VAIDYA, S. & MASAND, S. 2017. A novel reactive dye system based on diazonium salts. *Dyes and Pigments,* 145**,** 208-215.

BIAO, L., TAN, S., WANG, Y., GUO, X., FU, Y., XU, F., ZU, Y. & LIU, Z. 2017. Synthesis, characterization and antibacterial study on the chitosan-functionalized Ag nanoparticles. *Materials Science and Engineering: C,* 76**,** 73-80.

BORTHAKUR, P., BORUAH, P. K., HUSSAIN, N., SILLA, Y. & DAS, M. R. 2017. Specific ion effect on the surface properties of Ag/reduced graphene oxide nanocomposite and its influence on photocatalytic efficiency towards azo dye degradation. *Applied Surface Science,* 423**,** 752-761.

BOYJOO, Y., SUN, H., LIU, J., PAREEK, V. K. & WANG, S. 2017. A review on photocatalysis for air treatment: From catalyst development to reactor design. *Chemical Engineering Journal,* 310, Part 2**,** 537-559.

BRAGA, T. P., DIAS, D. F., DE SOUSA, M. F., SOARES, J. M. & SASAKI, J. M. 2015. Synthesis of air stable FeCo alloy nanocrystallite by proteic sol–gel method using a rotary oven. *Journal of Alloys and Compounds,* 622**,** 408-417.

BRICEÑO, S., SUAREZ, J. & GONZALEZ, G. 2017. Solvothermal synthesis of cobalt ferrite hollow spheres with chitosan. *Materials Science and Engineering: C,* 78**,** 842-846.

BRÜSCHWEILER, B. J. & MERLOT, C. 2017. Azo dyes in clothing textiles can be cleaved into a series of mutagenic aromatic amines which are not regulated yet. *Regulatory Toxicology and Pharmacology,* 88**,** 214-226.

CALVACHE-MUÑOZ, J., PRADO, F. A. & RODRÍGUEZ-PÁEZ, J. E. 2017. Cerium oxide nanoparticles: Synthesis, characterization and tentative mechanism of particle formation. *Colloids and Surfaces A: Physicochemical and Engineering Aspects,* 529**,** 146-159.

CHAKRABARTI, S. & DUTTA, B. K. 2004. Photocatalytic degradation of model textile dyes in wastewater using ZnO as semiconductor catalyst. *Journal of Hazardous Materials,* 112**,** 269-278.

CHAKRABORTY, J. N. 2014. 6 - Dyeing with reactive dye. *Fundamentals and Practices in Colouration of Textiles.* Woodhead Publishing India.

CHANNEI, D., NAKARUK, A. & PHANICHPHANT, S. 2017. Photocatalytic degradation of dye using CeO2/SCB composite catalysts. *Spectrochimica Acta Part A: Molecular and Biomolecular Spectroscopy,* 183**,** 218-224.

CHENG, Y., LI, Y., JI, G., QUAN, B., LIANG, X., ZHAO, Z., CAO, J. & DU, Y. 2017. Magnetic and electromagnetic properties of Fe3O4/Fe composites prepared by a simple one-step ball-milling. *Journal of Alloys and Compounds,* 708**,** 587-593.

CHEQUER, F. M. D., DE OLIVEIRA, G. A. R., FERRAZ, E. R. A., CARDOSO, J. C., ZANONI, M. V. B. & DE OLIVEIRA, D. P. 2013. Textile Dyes: Dyeing Process and Environmental Impact, Eco-Friendly Textile Dyeing and Finishing. *Textle Technology*.

CRETESCU, I., LUPASCU, T., BUCISCANU, I., BALAU-MINDRU, T. & SOREANU, G. 2017. Low-cost sorbents for the removal of acid dyes from aqueous solutions. *Process Safety and Environmental Protection,* 108**,** 57-66.

DANIAL, A. S., SALEH, M. M., SALIH, S. A. & AWAD, M. I. 2015. On the synthesis of nickel oxide nanoparticles by sol–gel technique and its electrocatalytic oxidation of glucose. *Journal of Power Sources,* 293**,** 101-108.

DASGUPTA, J., CHAKRABORTY, S., SIKDER, J., KUMAR, R., PAL, D., CURCIO, S. & DRIOLI, E. 2014. The effects of thermally stable titanium silicon oxide nanoparticles on structure and performance of cellulose acetate ultrafiltration membranes. *Separation and Purification Technology,* 133**,** 55-68.

DAVAR, F., FERESHTEH, Z. & SALAVATI-NIASARI, M. 2009. Nanoparticles Ni and NiO: Synthesis, characterization and magnetic properties. *Journal of Alloys and Compounds,* 476**,** 797-801.

DE PAIVA, J. A. C., GRAÇA, M. P. F., MONTEIRO, J., MACEDO, M. A. & VALENTE, M. A. 2009. Spectroscopy studies of NiFe2O4 nanosized powders obtained using coconut water. *Journal of Alloys and Compounds,* 485**,** 637-641.

DELLAMATRICE, P. M., SILVA-STENICO, M. E., MORAES, L. A. B. D., FIORE, M. F. & MONTEIRO, R. T. R. 2017. Degradation of textile dyes by cyanobacteria. *Brazilian Journal of Microbiology,* 48**,** 25-31.

DENG, L., ZHANG, X., LI, Y., QUE, F., KANG, X., LIU, Y., FENG, F. & ZHANG, H. 2018. Characterization of gelatin/zein nanofibers by hybrid electrospinning. *Food Hydrocolloids,* 75**,** 72-80.

DEY, S., SHERLY, M. C. D., REKHA, M. R. & SREENIVASAN, K. 2016. Alginate stabilized gold nanoparticle as multidrug carrier: Evaluation of cellular interactions and hemolytic potential. *Carbohydrate Polymers,* 136**,** 71-80.

DONG, H., ZENG, G., TANG, L., FAN, C., ZHANG, C., HE, X. & HE, Y. 2015. An overview on limitations of TiO2-based particles for photocatalytic degradation of organic pollutants and the corresponding countermeasures. *Water Research,* 79**,** 128-146.

DOS SANTOS, C., #XE1, MORILLA, S., MARTINS, A. F. N., COSTA, B. C., RIBEIRO, T. S., BRAGA, T. P., SOARES, J., #XE3, MARIA, O., SASAKI, J., #XE9 & MARCOS 2016a. Synthesis of FeNi Alloy Nanomaterials by Proteic Sol-Gel Method: Crystallographic, Morphological, and Magnetic Properties. *Journal of Nanomaterials,* 2016**,** 9.

DOS SANTOS, C., MARTINS, A. F. N., COSTA, B. C., RIBEIRO, T. S., BRAGA, T. P., SASAKI, J. & MARCOS 2016b. Synthesis of FeNi Alloy Nanomaterials by Proteic Sol-Gel Method: Crystallographic, Morphological, and Magnetic Properties. *Journal of Nanomaterials,* 2016**,** 9.

DUHAN, J. S., KUMAR, R., KUMAR, N., KAUR, P., NEHRA, K. & DUHAN, S. 2017. Nanotechnology: The new perspective in precision agriculture. *Biotechnology Reports,* 15**,** 11-23.

EDRALIN, E. J. M., GARCIA, J. L., DELA ROSA, F. M. & PUNZALAN, E. R. 2017. Sonochemical synthesis, characterization and photocatalytic properties of hydroxyapatite nano-rods derived from mussel shells. *Materials Letters,* 196**,** 33-36.

EL-KEMARY, M., NAGY, N. & EL-MEHASSEB, I. 2013. Nickel oxide nanoparticles: Synthesis and spectral studies of interactions with glucose. *Materials Science in Semiconductor Processing,* 16**,** 1747-1752.

EL HASSANI, K., BEAKOU, B. H., KALNINA, D., OUKANI, E. & ANOUAR, A. 2017. Effect of morphological properties of layered double hydroxides on adsorption of azo dye Methyl Orange: A comparative study. *Applied Clay Science,* 140**,** 124-131.

ELSAYED, K. A., IMAM, H., AHMED, M. A. & RAMADAN, R. 2013. Effect of focusing conditions and laser parameters on the fabrication of gold nanoparticles via laser ablation in liquid. *Optics & Laser Technology,* 45**,** 495-502.

ERTUGAY, N. & ACAR, F. N. 2017. Removal of COD and color from Direct Blue 71 azo dye wastewater by Fenton's oxidation: Kinetic study. *Arabian Journal of Chemistry,* 10**,** S1158-S1163.

FAN, C. & WANG, D.-A. 2016. Novel Gelatin-based Nano-gels with Coordination-induced Drug Loading for Intracellular Delivery. *Journal of Materials Science & Technology,* 32**,** 840-844.

FAZLALI, F., MAHJOUB, A. R. & ABAZARI, R. 2015. A new route for synthesis of spherical NiO nanoparticles via emulsion nano-reactors with enhanced photocatalytic activity. *Solid State Sciences,* 48**,** 263-269.

FERREIRA, L. C., LUCAS, M. S., FERNANDES, J. R. & TAVARES, P. B. 2016. Photocatalytic oxidation of Reactive Black 5 with UV-A LEDs. *Journal of Environmental Chemical Engineering,* 4**,** 109-114.

FORGACS, E., CSERHÁTI, T. & OROS, G. 2004. Removal of synthetic dyes from wastewaters: a review. *Environment International,* 30**,** 953-971.

GHAZALI, N. A. B., EBERT, M., DITSHEGO, N. M. J., DE PLANQUE, M. R. R. & CHONG, H. M. H. 2016. Top-down fabrication optimisation of ZnO nanowire-FET by sidewall smoothing. *Microelectronic Engineering,* 159**,** 121-126.

GOSWAMI, M. & PHUKAN, P. 2017. Enhanced adsorption of cationic dyes using sulfonic acid modified activated carbon. *Journal of Environmental Chemical Engineering,* 5**,** 3508-3517.

GUPTA, V. K., KUMAR, R., NAYAK, A., SALEH, T. A. & BARAKAT, M. A. 2013. Adsorptive removal of dyes from aqueous solution onto carbon nanotubes: A review. *Advances in Colloid and Interface Science,* 193**,** 24-34.

HAIKAL, R. R., SOLIMAN, A. B., AMIN, M., KARAKALOS, S. G., HASSAN, Y. S., ELMANSI, A. M., HAFEZ, I. H., BERBER, M. R., HASSANIEN, A. & ALKORDI, M. H. 2017. Synergism of carbon nanotubes and porous-organic polymers (POPs) in CO2 fixation: One-pot approach for bottom-up assembly of tunable heterogeneous catalyst. *Applied Catalysis B: Environmental,* 207**,** 347-357.

HARISHA, S., KESHAVAYYA, J., KUMARA SWAMY, B. E. & VISWANATH, C. C. 2017. Synthesis, characterization and electrochemical studies of azo dyes derived from barbituric acid. *Dyes and Pigments,* 136**,** 742-753.

HASHEM, M., SAION, E., AL-HADA, N. M., KAMARI, H. M., SHAARI, A. H., TALIB, Z. A., PAIMAN, S. B. & KAMARUDEEN, M. A. 2016. Fabrication and characterization of semiconductor nickel oxide (NiO) nanoparticles manufactured using a facile thermal treatment. *Results in Physics,* 6**,** 1024-1030.

HASSANZADEH SIAHPOOSH, Z. & SOLEIMANI, M. 2017. Photocatalytic degradation of azo anionic dye (RR120) in ZnO-Ghezeljeh nanoclay composite catalyst/UV-C system: Equilibrium, kinetic and thermodynamic studies. *Process Safety and Environmental Protection,* 111**,** 180-193.

HE, K., RUAN, Z., TENG, X. & ZHU, Y. 2017. Facile synthesis and electrochemical properties of spherical LiNi0.85−xCo0.15AlxO2 with sodium aluminate via co-precipitation. *Materials Research Bulletin,* 90**,** 131-137.

HOLKAR, C. R., JADHAV, A. J., PINJARI, D. V., MAHAMUNI, N. M. & PANDIT, A. B. 2016. A critical review on textile wastewater treatments: Possible approaches. *Journal of Environmental Management,* 182**,** 351-366.

HU, J., GUO, Z., CHU, W., LI, L. & LIN, T. 2015. Carbon dioxide catalytic conversion to nano carbon material on the iron–nickel catalysts using CVD-IP method. *Journal of Energy Chemistry,* 24**,** 620-625.

HU, L., CAO, X., SHI, L., QI, F., GUO, Z., LU, J. & GU, H. 2011. A Highly Active Nano-Palladium Catalyst for the Preparation of Aromatic Azos under Mild Conditions. *Organic Letters,* 13**,** 5640-5643.

HUANG, M., XU, C., WU, Z., HUANG, Y., LIN, J. & WU, J. 2008. Photocatalytic discolorization of methyl orange solution by Pt modified TiO2 loaded on natural zeolite. *Dyes and Pigments,* 77**,** 327-334.

HUNG, C.-H., YUAN, C. & LI, H.-W. 2017. Photodegradation of diethyl phthalate with PANi/CNT/TiO2 immobilized on glass plate irradiated with visible light and simulated sunlight—effect of synthesized method and pH. *Journal of Hazardous Materials,* 322, Part A**,** 243-253.

IMRAN DIN, M. & RANI, A. 2016a. Recent Advances in the Synthesis and Stabilization of Nickel and Nickel Oxide Nanoparticles: A Green Adeptness. *International Journal of Analytical Chemistry,* 2016**,** 14.

IMRAN DIN, M. & RANI, A. 2016b. Recent Advances in the Synthesis and Stabilization of Nickel and Nickel Oxide Nanoparticles: A Green Adeptness. *International Journal of Analytical Chemistry,* 2016**,** 3512145.

JUNAID, M., KHAN, M. A., IQBAL, F., MURTAZA, G., AKHTAR, M. N., AHMAD, M., SHAKIR, I. & WARSI, M. F. 2016. Structural, spectral, dielectric and magnetic properties of Tb–Dy doped Li-Ni nano-ferrites synthesized via micro-emulsion route. *Journal of Magnetism and Magnetic Materials,* 419**,** 338-344.

KAUR, P., KUMAR, S., CHEN, C.-L., YANG, K.-S., WEI, D.-H., DONG, C.-L., SRIVASTAVA, C. & RAO, S. M. 2017. Gd doping induced weak ferromagnetic ordering in ZnS nanoparticles synthesized by low temperature co-precipitation technique. *Materials Chemistry and Physics,* 186**,** 124-130.

KAVITHA, S. K. & PALANISAMY, P. N. 2011. Photocatalytic and Sonophotocatalytic Degradation of Reactive Red 120 using Dye Sensitized TiO_2 under Visible Ligh. *World Academy of Science, Engineering & Technology***,** 1.

KHATAEE, A. R., PONS, M. N. & ZAHRAA, O. 2009. Photocatalytic degradation of three azo dyes using immobilized TiO2 nanoparticles on glass plates activated by UV light irradiation: Influence of dye molecular structure. *Journal of Hazardous Materials,* 168**,** 451-457.

KHATRI, M., AHMED, F., SHAIKH, I., PHAN, D.-N., KHAN, Q., KHATRI, Z., LEE, H. & KIM, I. S. 2017. Dyeing and characterization of regenerated cellulose nanofibers with vat dyes. *Carbohydrate Polymers,* 174**,** 443-449.

KHAZAEI, A., KHAZAEI, M. & RAHMATI, S. 2015. A green method for the synthesis of gelatin/pectin stabilized palladium nano-particles as efficient heterogeneous catalyst for solvent-free Mizoroki–Heck reaction. *Journal of Molecular Catalysis A: Chemical,* 398**,** 241-247.

KHEZRIANJOO, S. & REVANASIDDAPPA, H. D. 2013. Photocatalytic Degradation of Acid Yellow 36 Using Zinc Oxide Photocatalyst in Aqueous Media. *Journal of Catalysts,* 2013**,** 6.

KRISTINAITYTĖ, K., DAGYS, L., KAUSTEKLIS, J., KLIMAVICIUS, V., DOROSHENKO, I., POGORELOV, V., VALEVIČIENĖ, N. R. & BALEVICIUS, V. 2017. NMR and FTIR studies of clustering of water molecules: From low-temperature matrices to nano-structured materials used in innovative medicine. *Journal of Molecular Liquids,* 235**,** 1-6.

KRÓL, A., POMASTOWSKI, P., RAFIŃSKA, K., RAILEAN-PLUGARU, V. & BUSZEWSKI, B. 2017. Zinc oxide nanoparticles: Synthesis, antiseptic activity and toxicity mechanism. *Advances in Colloid and Interface Science*.

KUMAR, A., AGARWALA, V. & SINGH, D. 2014. Effect of milling on dielectric and microwave absorption properties of SiC based composites. *Ceramics International,* 40**,** 1797-1806.

KUMAR, R., BARATTO, C., FAGLIA, G., SBERVEGLIERI, G., BONTEMPI, E. & BORGESE, L. 2015. Tailoring the textured surface of porous nanostructured NiO thin films for the detection of pollutant gases. *Thin Solid Films,* 583**,** 233-238.

KURIAN, M. & NAIR, D. S. 2016. Effect of preparation conditions on Nickel Zinc Ferrite nanoparticles: A comparison between sol–gel auto combustion and co-precipitation methods. *Journal of Saudi Chemical Society,* 20, Supplement 1**,** S517-S522.

KWAN, S. E., BAR-ZEEV, E. & ELIMELECH, M. 2015. Biofouling in forward osmosis and reverse osmosis: Measurements and mechanisms. *Journal of Membrane Science,* 493**,** 703-708.

LANFREDI, S., NOBRE, M. A. L., MORAES, P. G. P. & MATOS, J. 2014. Photodegradation of phenol red on a Ni-doped niobate/carbon composite. *Ceramics International,* 40**,** 9525-9534.

LAY, E., BENAMIRA, M., PIROVANO, C., GAUTHIER, G. & DESSEMOND, L. 2012. Effect of Ce-Doping on the Electrical and Electrocatalytical Behavior of La/Sr Chromo-Manganite Perovskite as New SOFC Anode. *Fuel Cells,* 12**,** 265-274.

LEE, J.-A., SEO, B. B., CHOI, I.-C., SEOK, M.-Y., ZHAO, Y., JAHED, Z., RAMAMURTY, U., TSUI, T. Y. & JANG, J.-I. 2016. Time-dependent nanoscale plasticity in nanocrystalline nickel rods and tubes. *Scripta Materialia,* 112**,** 79-82.

LEE, J.-H., KIM, C.-K., KATOH, S. & MURAKAMI, R. 2001. Microwave-hydrothermal versus conventional hydrothermal preparation of Ni- and Zn-ferrite powders. *Journal of Alloys and Compounds,* 325**,** 276-280.

LERMYTE, F., VERSCHUEREN, T., BROWN, J. M., WILLIAMS, J. P., VALKENBORG, D. & SOBOTT, F. 2015. Characterization of top-down ETD in a travelling-wave ion guide. *Methods,* 89**,** 22-29.

LI, J., WANG, X., ZHAO, J., CHEN, J., JIA, T. & CAO, C. 2016. Porous lithium nickel cobalt manganese oxide hierarchical nanosheets as high rate capability cathodes for lithium ion batteries. *Journal of Power Sources,* 307**,** 731-737.

LI, Q., WANG, L.-S., HU, B.-Y., YANG, C., ZHOU, L. & ZHANG, L. 2007. Preparation and characterization of NiO nanoparticles through calcination of malate gel. *Materials Letters,* 61**,** 1615-1618.

LI, Y. H., WANG, Y., ZHENG, L. R., ZHAO, H. J., YANG, H. G. & LI, C. 2017. Water-soluble inorganic photocatalyst for overall water splitting. *Applied Catalysis B: Environmental,* 209**,** 247-252.

LIANG, G., HUOT, J., BOILY, S., VAN NESTE, A. & SCHULZ, R. 1999. Hydrogen storage properties of the mechanically milled MgH2–V nanocomposite. *Journal of Alloys and Compounds,* 291**,** 295-299.

LIANG, H., WANG, Z., LIAO, L., CHEN, L., LI, Z. & FENG, J. 2017. High performance photocatalysts: Montmorillonite supported-nano TiO2 composites. *Optik - International Journal for Light and Electron Optics,* 136**,** 44-51.

LINDA, T., MUTHUPOONGODI, S., SHAJAN, X. S. & BALAKUMAR, S. 2016. Fabrication and characterization of chitosan templated CdO/NiO nano composite for dye degradation. *Optik - International Journal for Light and Electron Optics,* 127**,** 8287-8293.

LIU, J.-L., LUO, H.-J. & WEI, C.-H. 2007. Degradation of anthraquinone dyes by ozone. *Transactions of Nonferrous Metals Society of China,* 17**,** 880-886.

LIU, X., QIU, M. & HUANG, C. 2011. Degradation of the Reactive Black 5 by Fenton and Fenton-like system. *Procedia Engineering,* 15**,** 4835-4840.

LONTIO FOMEKONG, R., LAHEM, D., DEBLIQUY, M., DUPONT, V., NGOLUI, J. L. & DELCORTE, A. 2016. Co-precipitation Synthesis by Malonate Route, Structural Characterization and Gas Sensing Properties of Zn-doped NiO. *Materials Today: Proceedings,* 3**,** 586-591.

LOW, Z. H., CHEN, S. K., ISMAIL, I., TAN, K. S. & LIEW, J. Y. C. 2017. Structural transformations of mechanically induced top-down approach BaFe12O19 nanoparticles synthesized from high crystallinity bulk materials. *Journal of Magnetism and Magnetic Materials,* 429**,** 192-202.

LTAÏEF, A. H., D'ANGELO, A., AMMAR, S., GADRI, A., GALIA, A. & SCIALDONE, O. 2017. Electrochemical treatment of aqueous solutions of catechol by various electrochemical advanced oxidation processes: Effect of the process and of operating parameters. *Journal of Electroanalytical Chemistry,* 796**,** 1-8.

LU, Y.-J., LIU, C.-F., HU, C.-C., KUO, J.-H. & BODDULA, R. 2017. Fabrication and characterization of ZnO nanowires array electrodes with high photocurrent densities: Effects of the seed layer calcination time. *Materials Chemistry and Physics,* 189**,** 56-63.

MAHATO, T. H., PRASAD, G. K., SINGH, B., ACHARYA, J., SRIVASTAVA, A. R. & VIJAYARAGHAVAN, R. 2009. Nanocrystalline zinc oxide for the decontamination of sarin. *Journal of Hazardous Materials,* 165**,** 928-932.

MAHMOODI, N. M. 2013. Photocatalytic ozonation of dyes using multiwalled carbon nanotube. *Journal of Molecular Catalysis A: Chemical,* 366**,** 254-260.

MAHMOUD, A. M., IBRAHIM, F. A., SHABAN, S. A. & YOUSSEF, N. A. 2015. Adsorption of heavy metal ion from aqueous solution by nickel oxide nano catalyst prepared by different methods. *Egyptian Journal of Petroleum,* 24**,** 27-35.

MAIA, A. O. G., MENESES, C. T., MENEZES, A. S., FLORES, W. H., MELO, D. M. A. & SASAKI, J. M. 2006. Synthesis and X-ray structural characterization of NiO nanoparticles obtained through gelatin. *Journal of Non-Crystalline Solids,* 352**,** 3729-3733.

MAO, W., BAI, Y., WANG, B., WANG, W., MA, H., QIN, Y., LI, C., LU, J. & LIU, Z. 2017. A facile sol-gel synthesis of highly active nano α-aluminum fluoride catalyst for dehydrofluorination of hydrofluorocarbons. *Applied Catalysis B: Environmental,* 206**,** 65-73.

MBUYISA, P. N., NDWANDWE, O. M. & CEPEK, C. 2015. Controlled growth of zinc oxide nanorods synthesised by the hydrothermal method. *Thin Solid Films,* 578**,** 7-10.

MEDEIROS, A. M. L., MIRANDA, M. A. R., DE MENEZES, A. S., JARDIM, P. M., DA SILVA, L. R. D., GOUVEIA, S. T. & SASAKI, J. M. 2004. Synthesis and characterization of Cr2O3 nanoparticles obtained by gelatin. *Journal of Metastable and Nanocrystalline Materials,* 20-21**,** 399-404.

MIURA, K. R. P. N. 2004. Electrochemically deposited nanowhiskers of nickel oxide as a high-power pseudocapacitive electrode. *Applied Physics Letter,* 85**,** 4199-4201.

MOLINARI, R., MARINO, T. & ARGURIO, P. 2014. Photocatalytic membrane reactors for hydrogen production from water. *International Journal of Hydrogen Energy,* 39**,** 7247-7261.

MUÑOZ, A. & COSTA, M. 2012. Elucidating the mechanisms of nickel compound uptake: A review of particulate and nano-nickel endocytosis and toxicity. *Toxicology and Applied Pharmacology,* 260**,** 1-16.

MUTTA, G. R., POPURI, S. R., RUTERANA, P. & BUCKMAN, J. 2017. Single step hydrothermal synthesis of mixed valent V6O13 nano-architectures: A case study of the possible applications in electrochemical energy conversion. *Journal of Alloys and Compounds,* 706**,** 562-567.

NARAYANAN, K. B. & HAN, S. S. 2017. Dual-crosslinked poly(vinyl alcohol)/sodium alginate/silver nanocomposite beads – A promising antimicrobial material. *Food Chemistry,* 234**,** 103-110.

NASIRIAN, M., BUSTILLO-LECOMPTE, C. F. & MEHRVAR, M. 2017. Photocatalytic efficiency of Fe2O3/TiO2 for the degradation of typical dyes in textile industries: Effects of calcination temperature and UV-assisted thermal synthesis. *Journal of Environmental Management,* 196**,** 487-498.

NAVAS, M. P., SONI, R. K., TARASENKA, N. & TARASENKO, N. 2017. Temperature and solution assisted synthesis of anisotropic ZnO nanostructures by pulsed laser ablation. *Applied Surface Science,* 414**,** 413-423.

NGULUBE, T., GUMBO, J. R., MASINDI, V. & MAITY, A. 2017. An update on synthetic dyes adsorption onto clay based minerals: A state-of-art review. *Journal of Environmental Management,* 191**,** 35-57.

NGUYEN, T. A. & JUANG, R.-S. 2013. Treatment of waters and wastewaters containing sulfur dyes: A review. *Chemical Engineering Journal,* 219**,** 109-117.

OZCAN, O., YUKRUK, F., AKKAYA, E. U. & UNER, D. 2007. Dye sensitized artificial photosynthesis in the gas phase over thin and thick TiO2 films under UV and visible light irradiation. *Applied Catalysis B: Environmental,* 71**,** 291-297.

PALANISAMY, P. 2008. Biosurfactant mediated synthesis of NiO nanorods. *Materials Letters,* 62**,** 743-746.

PAN, Y., WANG, Y., ZHOU, A., WANG, A., WU, Z., LV, L., LI, X., ZHANG, K. & ZHU, T. 2017. Removal of azo dye in an up-flow membrane-less bioelectrochemical system integrated with bio-contact oxidation reactor. *Chemical Engineering Journal,* 326**,** 454-461.

PAPYNOV, E. K., PALAMARCHUK, M. S., MAYOROV, V. Y., MODIN, E. B., PORTNYAGIN, A. S., SOKOL'NITSKAYA, T. A., BELOV, A. A., TANANAEV, I. G. & AVRAMENKO, V. A. 2017. Sol-gel (template) synthesis of macroporous Mo-based catalysts for hydrothermal oxidation of radionuclide-organic complexes. *Solid State Sciences,* 69**,** 31-37.

PARE, B., JONNALAGADDA, S. B., TOMAR, H., SINGH, P. & BHAGWAT, V. W. 2008. ZnO assisted photocatalytic degradation of acridine orange in aqueous solution using visible irradiation. *Desalination,* 232**,** 80-90.

PARK, J. 2017. Visible and near infrared light active photocatalysis based on conjugated polymers. *Journal of Industrial and Engineering Chemistry,* 51**,** 27-43.

PATRA, S., BASAK, P. & TIBAREWALA, D. N. 2016. Synthesis of gelatin nano/submicron particles by binary nonsolvent aided coacervation (BNAC) method. *Materials Science and Engineering: C,* 59**,** 310-318.

PAWAR, S. N. & EDGAR, K. J. 2012. Alginate derivatization: A review of chemistry, properties and applications. *Biomaterials,* 33**,** 3279-3305.

PENG, X., PENG, K. & HUANG, J. 2017. Synthesis and magnetic properties of core-shell structured Finemet/NiZn ferrite soft nanocomposites by co-precipitation. *Journal of Alloys and Compounds,* 691**,** 165-170.

PINJARI, D. V., PRASAD, K., GOGATE, P. R., MHASKE, S. T. & PANDIT, A. B. 2015. Synthesis of titanium dioxide by ultrasound assisted sol–gel technique: Effect of calcination and sonication time. *Ultrasonics Sonochemistry,* 23**,** 185-191.

PRABHAKARAN, T., MANGALARAJA, R. V., DENARDIN, J. C. & JIMÉNEZ, J. A. 2017. The effect of calcination temperature on the structural and magnetic properties of co-precipitated CoFe2O4 nanoparticles. *Journal of Alloys and Compounds,* 716**,** 171-183.

QI, X., SU, G., BO, G., CAO, L. & LIU, W. 2015. Synthesis of NiO and NiO/TiO2 films with electrochromic and photocatalytic activities. *Surface and Coatings Technology,* 272**,** 79-85.

QING, Z., HAIXIA, L., HUALI, L., YU, L., HUAYONG, Z. & TIANDUO, L. 2015. Solvothermal synthesis and photocatalytic properties of NiO ultrathin nanosheets with porous structure. *Applied Surface Science,* 328**,** 525-530.

RAGHAVENDRA, G. M., JUNG, J., KIM, D. & SEO, J. 2017. Chitosan-mediated synthesis of flowery-CuO, and its antibacterial and catalytic properties. *Carbohydrate Polymers,* 172**,** 78-84.

RAHMANI, A. R., ZARRABI, M. & GHAFARI, L. R. 2010. Degradation of Azo Dye Reactive Black 5 and Acid Orange 7 by Fenton - like Mechanism. *Iranian Journal of Chemical Engineering,* 7**,** 87-94.

RAMESH, S. 2013. Sol-Gel Synthesis and Characterization of Nanoparticles. *Journal of Nanoscience,* 2013**,** 8.

RASHEED, T., BILAL, M., IQBAL, H. M. N. & LI, C. 2017. Green biosynthesis of silver nanoparticles using leaves extract of Artemisia vulgaris and their potential biomedical applications. *Colloids and Surfaces B: Biointerfaces,* 158**,** 408-415.

REDDY, C. V., SHIM, J. & CHO, M. 2017. Synthesis, structural, optical and photocatalytic properties of CdS/ZnS core/shell nanoparticles. *Journal of Physics and Chemistry of Solids,* 103**,** 209-217.

REPO, E., MÄKINEN, M., RENGARAJ, S., NATARAJAN, G., BHATNAGAR, A. & SILLANPÄÄ, M. 2012. Lepidocrocite and its heat-treated forms as effective arsenic adsorbents in aqueous medium. *Chemical Engineering Journal,* 180**,** 159-169.

RODRIGUEZ-NARVAEZ, O. M., PERALTA-HERNANDEZ, J. M., GOONETILLEKE, A. & BANDALA, E. R. 2017. Treatment technologies for emerging contaminants in water: A review. *Chemical Engineering Journal,* 323**,** 361-380.

ROY, B. C., DAS, C., HONG, H., BETTI, M. & BRUCE, H. L. 2017. Extraction and characterization of gelatin from bovine heart. *Food Bioscience,* 20**,** 116-124.

SAFEERA, T. A. & ANILA, E. I. 2017. Wet chemical synthesis of chitosan capped ZnO:Na nanoparticles for luminescence applications. *International Journal of Biological Macromolecules,* 104**,** 1833-1836.

SAGHATFOROUSH, L. A., HASANZADEH, M., SANATI, S. & MEHDIZADEH, T. 2012. $Ni(OH)_2$ and NiO Nanostructures: Synthesis, Characterization and Electrochemical Performance. *Korean Chem. Soc.,* 33.

SANTHOSH, C., VELMURUGAN, V., JACOB, G., JEONG, S. K., GRACE, A. N. & BHATNAGAR, A. 2016. Role of nanomaterials in water treatment applications: A review. *Chemical Engineering Journal,* 306**,** 1116-1137.

SARAVANAN, C., RAJESH, R., KAVIARASAN, T., MUTHUKUMAR, K., KAVITAKE, D. & SHETTY, P. H. 2017a. Synthesis of silver nanoparticles using bacterial exopolysaccharide and its application for degradation of azo-dyes. *Biotechnology Reports,* 15**,** 33-40.

SARAVANAN, K., SURIAKARTHICK, R., ANANTHAKUMAR, S., BABU, S. M. & SELLADURAI, S. 2017b. Colloidal synthesis of copper cadmium sulphide (CuCdS2) nanoparticles and its structural, optical and morphological properties. *Materials Science in Semiconductor Processing,* 66**,** 123-130.

SHANKAR, S., TENG, X., LI, G. & RHIM, J.-W. 2015. Preparation, characterization, and antimicrobial activity of gelatin/ZnO nanocomposite films. *Food Hydrocolloids,* 45**,** 264-271.

SHARMA, R., THAKUR, P., KUMAR, M., THAKUR, N., NEGI, N. S., SHARMA, P. & SHARMA, V. 2016. Improvement in magnetic behaviour of cobalt doped magnesium zinc nano-ferrites via co-precipitation route. *Journal of Alloys and Compounds,* 684**,** 569-581.

SHEN, W., LI, P., FENG, H., GE, Y., LIU, Z. & FENG, L. 2017. The bactericidal mechanism of action against Staphylococcus aureus for AgO nanoparticles. *Materials Science and Engineering: C,* 75**,** 610-619.

SHI, Y., HUANG, J., ZENG, G., GU, Y., CHEN, Y., HU, Y., TANG, B., ZHOU, J., YANG, Y. & SHI, L. 2017. Exploiting extracellular polymeric substances (EPS) controlling strategies for performance enhancement of biological wastewater treatments: An overview. *Chemosphere,* 180**,** 396-411.

SILVA, R. M., RAIMUNDO, R. A., FERNANDES, W. V., TORRES, S. M., SILVA, V. D., GRILO, J. P. F., MORALES, M. A. & MACEDO, D. A. 2018. Proteic sol-gel synthesis, structure and magnetic properties of Ni/NiO core-shell powders. *Ceramics International*.

SINGH, S., BHARTI, A. & MEENA, V. K. 2015. Green synthesis of multi-shaped silver nanoparticles: optical, morphological and antibacterial properties. *Journal of Materials Science: Materials in Electronics,* 26**,** 3638-3648.

SMALENSKAITE, A., VIEIRA, D. E. L., SALAK, A. N., FERREIRA, M. G. S., KATELNIKOVAS, A. & KAREIVA, A. 2017. A comparative study of co-precipitation and sol-gel synthetic approaches to fabricate cerium-substituted MgAl layered double hydroxides with luminescence properties. *Applied Clay Science,* 143**,** 175-183.

SODIPO, B. K. & AZIZ, A. A. 2016. Recent advances in synthesis and surface modification of superparamagnetic iron oxide nanoparticles with silica. *Journal of Magnetism and Magnetic Materials,* 416**,** 275-291.

SOLÍS, M., SOLÍS, A., PÉREZ, H. I., MANJARREZ, N. & FLORES, M. 2012. Microbial decolouration of azo dyes: A review. *Process Biochemistry,* 47**,** 1723-1748.

SOO, C. W., JUAN, J. C., LAI, C. W., HAMID, S. B. A. & YUSOP, R. M. 2016. Fe-doped mesoporous anatase-brookite titania in the solar-light-induced photodegradation of Reactive Black 5 dye. *Journal of the Taiwan Institute of Chemical Engineers,* 68**,** 153-161.

SOOD, A., ARORA, V., SHAH, J., KOTNALA, R. K. & JAIN, T. K. 2017. Multifunctional gold coated iron oxide core-shell nanoparticles stabilized using thiolated sodium alginate for biomedical applications. *Materials Science and Engineering: C,* 80**,** 274-281.

SOOFIVAND, F. & SALAVATI-NIASARI, M. 2017. Step synthesis and photocatalytic activity of NiO/graphene nanocomposite under UV and visible light as an effective photocatalyst. *Journal of Photochemistry and Photobiology A: Chemistry,* 337**,** 44-53.

SREEJA, V. & JOY, P. A. 2007. Microwave–hydrothermal synthesis of γ-Fe2O3 nanoparticles and their magnetic properties. *Materials Research Bulletin,* 42**,** 1570-1576.

STANKIC, S., SUMAN, S., HAQUE, F. & VIDIC, J. 2016. Pure and multi metal oxide nanoparticles: synthesis, antibacterial and cytotoxic properties. *Journal of Nanobiotechnology,* 14**,** 73.

SUN, J., WANG, X., SUN, J., SUN, R., SUN, S. & QIAO, L. 2006. Photocatalytic degradation and kinetics of Orange G using nano-sized Sn(IV)/TiO2/AC photocatalyst. *Journal of Molecular Catalysis A: Chemical,* 260**,** 241-246.

SWETHA, J. N. & GEETHA, A. 2015. Synthesis and characterization of nickel oxide and manganese oxide nanoparticles and NiO/MnO nanocomposite: hydrothermal approach. *Inthernational Journal of ChemTech Research,* 7**,** 2138-2143.

TADIC, M., NIKOLIC, D., PANJAN, M. & BLAKE, G. R. 2015. Magnetic properties of NiO (nickel oxide) nanoparticles: Blocking temperature and Neel temperature. *Journal of Alloys and Compounds,* 647**,** 1061-1068.

TANZIL, A. H., SULTANA, S. T., SAUNDERS, S. R., SHI, L., MARSILI, E. & BEYENAL, H. 2016. Biological synthesis of nanoparticles in biofilms. *Enzyme and Microbial Technology,* 95**,** 4-12.

TAO, L., YING, L. & GUOHUA, M. 2016. Preparation of Submicro-porous Nickel Wafers by Molding-Decomposition-Sintering Method Using Nickel Oxalate Nano-Rods as Precursors. *Rare Metal Materials and Engineering,* 45**,** 1396-1400.

THAMRI, S., STA, I., JLASSI, M., HAJJI, M. & EZZAOUIA, H. 2017. Fabrication of ZnO-NiO nanocomposite thin films and experimental study of the effect of the NiO, ZnO concentration on its physical properties. *Materials Science in Semiconductor Processing,* 71**,** 310-320.

TURGUT, G., SONMEZ, E. & DUMAN, S. 2015. Determination of certain sol-gel growth parameters of nickel oxide films. *Ceramics International,* 41**,** 2976-2989.

UDAY, U. S. P., BANDYOPADHYAY, T. K. & BHUNIA, B. 2016. Bioremediation and Detoxification Technology for Treatment of Dye(s) from Textile Effluent. *Textile Water Treatment*

VAN DER BRUGGEN, B., MÄNTTÄRI, M. & NYSTRÖM, M. 2008. Drawbacks of applying nanofiltration and how to avoid them: A review. *Separation and Purification Technology,* 63**,** 251-263.

VAN DER ZEE, F. P. & VILLAVERDE, S. 2005. Combined anaerobic–aerobic treatment of azo dyes—A short review of bioreactor studies. *Water Research,* 39**,** 1425-1440.

VARMA, A. J., DESHPANDE, S. V. & KENNEDY, J. F. 2004. Metal complexation by chitosan and its derivatives: a review. *Carbohydrate Polymers,* 55**,** 77-93.

VARUNKUMAR, K., HUSSAIN, R., HEGDE, G. & ETHIRAJ, A. S. 2017a. Effect of calcination temperature on Cu doped NiO nanoparticles prepared via wet-chemical method: Structural, optical and morphological studies. *Materials Science in Semiconductor Processing,* 66**,** 149-156.

VARUNKUMAR, K., HUSSAIN, R., HEGDE, G. & ETHIRAJ, A. S. 2017b. Effect of calcination temperature on Cu doped NiO nanoparticles prepared via wet-chemical method: Structural, optical and morphological studies. *Materials Science in Semiconductor Processing,* 66**,** 149-156.

VERMA, A. K., DASH, R. R. & BHUNIA, P. 2012. A review on chemical coagulation/flocculation technologies for removal of colour from textile wastewaters. *Journal of Environmental Management,* 93**,** 154-168.

VINOD, M. & GOPCHANDRAN, K. G. 2015. Ag@Au core–shell nanoparticles synthesized by pulsed laser ablation in water: Effect of plasmon coupling and their SERS performance. *Spectrochimica Acta Part A: Molecular and Biomolecular Spectroscopy,* 149**,** 913-919.

VINOTH, R., KARTHIK, P., DEVAN, K., NEPPOLIAN, B. & ASHOKKUMAR, M. 2017. TiO2–NiO p–n nanocomposite with enhanced sonophotocatalytic activity under diffused sunlight. *Ultrasonics Sonochemistry,* 35, Part B**,** 655-663.

WAN, X., MA, R., TIE, S. & LAN, S. 2014. Effects of calcination temperatures and additives on the photodegradation of methylene blue by tin dioxide nanocrystals. *Materials Science in Semiconductor Processing,* 27**,** 748-757.

WANG, C., TAN, X., YAN, J., CHAI, B., LI, J. & CHEN, S. 2017a. Electrospinning direct synthesis of magnetic ZnFe2O4/ZnO multi-porous nanotubes with enhanced photocatalytic activity. *Applied Surface Science,* 396**,** 780-790.

WANG, G., LU, G., YIN, P., ZHAO, L. & JIMMY YU, Q. 2016a. Genotoxicity assessment of membrane concentrates of landfill leachate treated with Fenton reagent and UV-Fenton reagent using human hepatoma cell line. *Journal of Hazardous Materials,* 307**,** 154-162.

WANG, H., CHEN, W., ZHANG, J., HUANG, C. & MAO, L. 2015. Nickel nanoparticles modified CdS – A potential photocatalyst for hydrogen production through water splitting under visible light irradiation. *International Journal of Hydrogen Energy,* 40**,** 340-345.

WANG, J., MI, W., TIAN, J., DAI, J., WANG, X. & LIU, X. 2013. Effect of calcinations of TiO2/ZnO composite powder at high temperature on photodegradation of methyl orange. *Composites Part B: Engineering,* 45**,** 758-767.

WANG, J., WEI, L., ZHANG, L., JIANG, C., SIU-WAI KONG, E. & ZHANG, Y. 2012. Preparation of high aspect ratio nickel oxide nanowires and their gas sensing devices with fast response and high sensitivity. *Journal of Materials Chemistry,* 22**,** 8327-8335.

WANG, Q., CUI, M., HOU, Y., ZHONG, Q., YUE, M. & HUANG, X. 2017b. The effect of precipitation pH on thermal stability and structure of Ce0.35Zr0.55(LaPr)0.1O2 oxides prepared by co-precipitation method. *Journal of Alloys and Compounds,* 712**,** 431-436.

WANG, R., LIANG, H., HONG, J. & WANG, Z. 2016b. Hydrothermal synthesis of cobalt-doped ZnS for efficient photodegradation of methylene blue. *Journal of Photochemistry and Photobiology A: Chemistry,* 325**,** 62-67.

WISZNIOWSKI, J., ROBERT, D., SURMACZ-GORSKA, J., MIKSCH, K. & WEBER, J.-V. 2002. Photocatalytic decomposition of humic acids on TiO2: Part I: Discussion of adsorption and mechanism. *Journal of Photochemistry and Photobiology A: Chemistry,* 152**,** 267-273.

WITOON, T., PERMSIRIVANICH, T., DONPHAI, W., JAREE, A. & CHAREONPANICH, M. 2013. CO2 hydrogenation to methanol over Cu/ZnO nanocatalysts prepared via a chitosan-assisted co-precipitation method. *Fuel Processing Technology,* 116**,** 72-78.

XU, L., SRINIVASAKANNAN, C., PENG, J., ZHANG, L. & ZHANG, D. 2017. Synthesis of Cu-CuO nanocomposite in microreactor and its application to photocatalytic degradation. *Journal of Alloys and Compounds,* 695**,** 263-269.

XU, Y. & XU, R. 2015. Nickel-based cocatalysts for photocatalytic hydrogen production. *Applied Surface Science,* 351**,** 779-793.

YAGUB, M. T., SEN, T. K., AFROZE, S. & ANG, H. M. 2014. Dye and its removal from aqueous solution by adsorption: A review. *Advances in Colloid and Interface Science,* 209**,** 172-184.

YAMINI, K., RENGANATHAN, B., GANESAN, A. R. & PRAKASH, T. 2017. Clad modified optical fiber gas sensors based on nanocrystalline nickel oxide embedded coatings. *Optical Fiber Technology,* 36**,** 139-143.

YANG, Q., LU, Z., LIU, J., LEI, X., CHANG, Z., LUO, L. & SUN, X. 2013. Metal oxide and hydroxide nanoarrays: Hydrothermal synthesis and applications as supercapacitors and nanocatalysts. *Progress in Natural Science: Materials International,* 23**,** 351-366.

YANG, W., ZHU, Z., SHI, J., ZHAO, B., CHEN, Z. & WU, Y. 2017. Characterizations of the thermal decomposition of nano-magnesium hydroxide by positron annihilation lifetime spectroscopy. *Powder Technology,* 311**,** 206-212.

YANG, Y. & DING, J. 2012. Microwave property of micron and sub-micron Fe90Al10 flakes fabricated via ball milling and jet milling routes. *Journal of Alloys and Compounds,* 528**,** 58-62.

YU, F., XU, X., PENG, H., YU, H., DAI, Y., LIU, W., YING, J., SUN, Q. & WANG, X. 2015. Porous NiO nano-sheet as an active and stable catalyst for CH4 deep oxidation. *Applied Catalysis A: General,* 507**,** 109-118.

YU, H., YU, J., CHENG, B. & LIN, J. 2007. Synthesis, characterization and photocatalytic activity of mesoporous titania nanorod/titanate nanotube composites. *Journal of Hazardous Materials,* 147**,** 581-587.

ZENG, G., YE, Z., HE, Y., YANG, X., MA, J., SHI, H. & FENG, Z. 2017. Application of dopamine-modified halloysite nanotubes/PVDF blend membranes for direct dyes removal from wastewater. *Chemical Engineering Journal,* 323**,** 572-583.

ZHANG, D. E., NI, X. M., ZHENG, H. G., LI, Y., ZHANG, X. J. & YANG, Z. P. 2005. Synthesis of needle-like nickel nanoparticles in water-in-oil microemulsion. *Materials Letters,* 59**,** 2011-2014.

ZHANG, M.-M., CHEN, W.-M., CHEN, B.-Y., CHANG, C.-T., HSUEH, C.-C., DING, Y., LIN, K.-L. & XU, H. 2010. Comparative study on characteristics of azo dye decolorization by indigenous decolorizers. *Bioresource Technology,* 101**,** 2651-2656.

ZHANG, Y. 2017. Glycine-assisted fabrication of NiO-based quantum dots light-emitting diodes. *Journal of Luminescence*.

ZHAO, X., LI, Z., DENG, Y., ZHAO, Z., LI, X. & XIA, Y. 2017. Facile Synthesis of Gold Nanoparticles with Alginate and Its Catalytic Activity for Reduction of 4-Nitrophenol and H(2)O(2) Detection. *Materials,* 10**,** 557.

ZHAO, X., XIA, Y., LI, Q., MA, X., QUAN, F., GENG, C. & HAN, Z. 2014. Microwave-assisted synthesis of silver nanoparticles using sodium alginate and their antibacterial activity. *Colloids and Surfaces A: Physicochemical and Engineering Aspects,* 444**,** 180-188.

ZHOU, M., YU, J., LIU, S., ZHAI, P. & JIANG, L. 2008. Effects of calcination temperatures on photocatalytic activity of SnO2/TiO2 composite films prepared by an EPD method. *Journal of Hazardous Materials,* 154**,** 1141-1148.

ZOU, H. & WANG, Y. 2017. Azo dyes wastewater treatment and simultaneous electricity generation in a novel process of electrolysis cell combined with microbial fuel cell. *Bioresource Technology*, 235**,** 167-175.